SEARCH FOR NEW SUPERFLUID STATES OF ^{3}HE CONFINED IN COHERENCE LENGTH SIZED NANOFABRICATED STRUCTURES

A Dissertation

Presented to the Faculty of the Graduate School

of Cornell University

in Partial Fulfillment of the Requirements for the Degree of

Doctor of Philosophy

by

Nikolay Zhelev Zhelev

May 2016

SEARCH FOR NEW SUPERFLUID STATES OF ^{3}HE CONFINED IN COHERENCE LENGTH SIZED NANOFABRICATED STRUCTURES

Nikolay Zhelev Zhelev, Ph.D.

Cornell University 2016

Properties of superfluid ^{3}He are greatly affected by proximity of surfaces and disorder. In this work, we describe three different experiments for which we use torsion pendulums to study the properties of the ^{3}He fluid confined within the torsion pendulum heads.

In the first two experiments, the fluid was embedded within anisotropic aerogel samples. In one case, we compressed an otherwise isotropic 98% open silica aerogel. In the other, we used a highly oriented, "nematically ordered" aerogel sample, which represented the limit of extremely stretched aerogel. In the third experiment, ^{3}He was confined within a nanofabricated high aspect ration 1080 nm deep cavity formed between patterned silicon disc bonded to a matching glass piece.

We obtained data for the superfluid fraction versus temperature for a number of pressures. We observe great modifications of the superfluid phase diagram for the confined fluid in all three experiments. The order parameters for the A and B phases are distorted and the regions of stability for these phases is drastically different compared to the bulk or previous experiments with isotropic aerogels.

In particular, the highly anisotropic disorder provided by the "nematically ordered" aerogel sample gives rise to a phase transition not seen in the bulk. We argue that at low pressures in the temperature region near the superfluid

transition we observe a superfluid state that is closely related to Polar phase.

In the experiment in which we confined the fluid within the 1080 nm deep cavity, we see an A to B phase transition at all experimental pressures. We, however, do not observe any signature of a new superfluid state (Stripe phase), which has been predicted to occur at the onset of the A to B transition.

BIOGRAPHICAL SKETCH

Nikolay was born in in Burgas, a sunny city on the coast of Black Sea in the southeastern part of Bulgaria. Nikolay spent nineteen years of his life in Bulgaria, before he traveled to the other side of the globe, where he attended Colgate University in the tiny Upstate New York town of Hamilton. There, Nikolay earned his bachelor's degree in physics and mathematics. After his college graduation in 2009, Nikolay moved an hour and a half southwest to Ithaca, where he began his graduate school career at Cornell. There he joined the group of Jeevak Parpia, and learned a lot of valuable lessons on how to be a scientist and how to persevere when faced with difficult problems. But most importantly, it was there where he met his fiancée, Kayla, which provided meaning to all the sacrifices he had to endure.

Nikolay recently accepted a job offer from Corning Inc., and will be starting his job there after he successfully defends his PhD.

To my fiancée, Kayla, who has always provided me with encouragement in the face of hardships. To my parents for giving me all their support.

ACKNOWLEDGEMENTS

I want to thank my advisor Jeevak Parpia, for his patience and mentorship. He was always available to me and my fellow lab mates. He taught us through example and dedication.

I want to also thank the other members of special committee, Erich Mueller and Séamus Davis. Erich and his student Matthew Reichl did the theoretical work behind the "nematic aerogel" part of this thesis.

Rob Bennett and Andrew Fefferman did a lot of the early work on the compressed aerogel sample experiment. Taking data and the subsequent analysis on this experiment was a joint effort between Rob and I. Rob also did a lot of the early work on the experiment in which the fluid was confined to a 1080 nm deep cavity. Large portion of the work described here would not have been possible without his efforts.

I also want to thank my current lab mates, Abhilash Sebastian, who was instrumental in the fabrication of the cells for the confined cavity experiments and helped immensely with the setup and running the experiments, and Robert DeAlba for being a great friend and colleague.

I am also extremely grateful to Eric Smith. His expertise and knowledge of low temperature techniques is rivaled by none. He has been a great resource that has been invaluable to everybody in the lab.

I also want to thank my collaborators: Johannes Pollanen, Joshua Wiman, William Halperin, and James Sauls from Northwestern University and Lev Levitin, Andrew Casey, Xavier Rojas, and John Saunders from Royal Holloway University in London.

TABLE OF CONTENTS

LIST OF TABLES

LIST OF FIGURES

CHAPTER 1

INTRODUCTION AND OUTLINE

Around Thanksgiving of 1971, in a lab in the basement of Clark Hall, superfluidity of ^{3}He was first discovered by David Lee, Robert Richardson and Douglas Osheroff [1]. Superfluid ^{3}He exhibits some remarkable properties that have made it such an interesting system to study. The rich physics of this extraordinary state of matter led it to being recognized by the Nobel committee which to date has awarded two Nobel prizes, in 1996 and in 2003 recognizing researchers who have devoted their career on studying superfluid ^{3}He.

Superfluid ^{3}He has a p-wave fermionic pairing, and has proved to be a model system for other p-wave fermionic systems such as $SrRu_2O_4$. Superfluid ^{3}He also comes in multiple superfluid phases; it has proved to be valuable for studying materials that have multiple superconducting phases, such as the heavy-fermion superconductor UPt_3. Properties of superfluid ^{3}He are also highly tunable one can use pressure to change the stability of the different superfluid phases and tune the superfluid transition temperature by approximately a factor of 2.5, from 0.9 mK at 0 bar to 2.44 mK at 34 bar.

Disorder and confinement are two other ways we can tune the properties of the superfluid. The goal for this work is to elucidate how the properties of the superfluid change when these two parameters are varied. Here I will describe two types of experiments. In the first, ^{3}He is confined within a highly porous aerogel. The aerogel provides a way for us to engineer disorder into the system. By either squeezing the aerogel, or by using an extremely anisotropic (*nematically ordered*) aerogel, we can introduce anisotropic disorder, which greatly modifies the superfluid phase diagram and the stability of the different superfluid

phases. The superfluid order parameter is modified compared to the order parameter in the bulk, and when the fluid is confined within the *nematically ordered* aerogel, at low pressures and at temperatures near the superfluid transition, a new superfluid state, which is not realized in the bulk fluid, is observed.

In the second set of experiments, ^{3}He is confined to a thin slab within a nanofabricated cavity. The particular experimental results described here are for a cavity with a depth of 1080 nm. The extreme confinement allows us to study the surface properties of the superfluid, and the superfluidity of thin films. A new superfluid state, which breaks translational symmetry, referred to as the *Stripe phase* is predicted in such a geometry [48]. We aim to map the phase diagram for the fluid within the 1080 nm slab and search for the *Stripe phase*.

The layout of this thesis is as follows:

In chapter 2, I will give a brief overview of the properties of bulk superfluid ^{3}He and its various superfluid phases.

In chapter 3, I will review the theoretical predictions and previous experimental results for the properties of the superfluid ^{3}He confined within a porous aerogel.

In chapter 4, I will review the theoretical predictions and previous experimental results for the properties of the superfluid ^{3}He confined within a thin slab.

In chapter 5, I will discuss the details of the experimental setup used for the experiments I have carried out, as well as the fabrication process for the type of cells used to study the fluid under confinement.

In chapter 6, I will present the experimental results and analysis for an experiment looking at superfluid ^{3}He embedded in a 10% uniaxially compressed silica aerogel sample.

In chapter 7, I will present the experimental results and analysis for an experiment studying the properties of superfluid ^{3}He embedded in a highly anisotropic *nematically ordered* alumina aerogel sample.

In chapter 8, I will present the results and the analysis for the most recent experiment I carried out, in which the properties for the superfluid confined within a 1080 nm nanofabricated cavity were investigated and will conclude with a fairly brief discussion of future projects that this work has laid the ground for.

CHAPTER 2

SUPERFLUID ^{3}HE

2.1 Fermionic Superfluidity. BCS theory

Helium comes in two distinct isotopes: ^{4}He and ^{3}He. Although the condensates of the two isotopes have similar properties at high temperatures, they behave radically different at temperatures close to the absolute zero. ^{4}He atoms have integer spin, i.e. they obey Bose-Einstein statistics, thus at low temperatures, we would expect to have large occupancy in the quantum ground state. The model of an interacting Bose liquid qualitatively describes the lambda transition for ^{4}He, which occurs at $T_\lambda \sim 2$ K. Below the lambda transition, a fraction of the fluid is in a superfluid state – a state which manifests itself by allowing the fluid to flow with no dissipation, i.e. the viscosity of the fluid drops sharply. In the superfluid state, we can describe the ^{4}He atoms by a single wavefunction, which defines the complex order parameter of the system.

Unlike ^{4}He, the ^{3}He particles have spin, which is equal to ½, are fermions, and due to the Pauli-exclusion principle no two particles can be in the same quantum state. At first glance, that would lead us to the conclusion that we cannot have a superfluid transition in ^{3}He. We know that this is not the case, thus the mechanism for ^{3}He superfluidity must be distinctively different from that in ^{4}He.

In normal ^{3}He, at low temperatures, the quantum states with energy less than the Fermi energy, ε_F, are occupied. The Fermi surface is simple. For ^{3}He it is a sphere. Since energy states deep into the Fermi sphere are surrounded by

filled energy states, they lack available states in which they can scatter. Thus, the properties of the fluid are determined largely by the particles with energy close to the Fermi surface. Properties of normal ^{3}He are described by the Fermi-liquid theory [3], which models the strongly interacting system as a weakly interacting system by replacing the ^{3}He particles by quasiparticles with somewhat larger mass.

To describe the superfluid state, we would make the analogy with another well-known Fermi fluid the electrons in metals. Bardeen, Cooper and Schrieffer proposed the BCS theory of superconductivity [4], by considering a small attractive interaction between the electrons in superconducting metals mediated by their interactions with the crystal lattice. Below a critical temperature T_c, these interactions become strong enough to precipitate the formation of Cooper pairs – pairs of fermions that have an integer spin and are hence bosons. The fermions that make up the Cooper pairs come from a narrow band near the Fermi level, and due to the attractive potential form a pair with a total energy less than $2\varepsilon_F$. It can be shown that Cooper pairs condense into a coherent quantum state, which defines the superconducting condensate. Having particles near the Fermi surface form Cooper pairs produces an energy gap for the density of states 2Δ centered at the Fermi level separating the filled from the unoccupied states. The energy gap Δ represents the minimum energy needed to break the pair. Excitations with energy less than Δ are not possible, so small enough currents will be conducted without any resistance.

The mechanism for superfluidity in ^{3}He is similar to the BCS mechanism for electrons in superconducting metals. One major difference, however, is that ^{3}He, being a fluid, does not possess a crystal lattice which would mediate the

attractive interactions between the fermions. Attractive potential for the ^{3}He Cooper pairs is mediated through spin wave excitations [5]. Unlike ordinary superconductors, where the Cooper pairs are in the spin singlet state ($S = 0$), the nature of interactions for ^{3}He force Cooper pairs to be in the spin triplet state ($S = 1$). A theorem from quantum mechanics tells us that two fermion particle states with an even spin quantum number, must also have an even orbital angular momentum quantum number, while states for which S is odd, have l also being odd [6]. This means that the Cooper pairs for ^{3}He are in the $\ell = 1$ state (p-wave), rather than the $\ell = 0$ (s-wave) state as for the ordinary BCS superconductors.

2.2 Superfluid Order Parameter

The spin triplet state consists of three possible spin states: $|\uparrow\uparrow\rangle$, $|\downarrow\downarrow\rangle$, or $\frac{1}{\sqrt{2}}(|\uparrow\downarrow\rangle + |\downarrow\uparrow\rangle)$. Therefore the wavefunction for the most general state of the Cooper pairs is given by:

$$\Psi = \psi_{\uparrow\uparrow}(\hat{\mathbf{k}})\,|\uparrow\uparrow\rangle + \psi_{\downarrow\downarrow}(\hat{\mathbf{k}})\,|\downarrow\downarrow\rangle + \psi_{\uparrow\downarrow}(\hat{\mathbf{k}})(|\uparrow\downarrow\rangle + |\downarrow\uparrow\rangle) \tag{2.1}$$

where the unit vector $\hat{\mathbf{k}}$ defines a particular position on the Fermi surface. This wavefunction can be represented in matrix form as:

$$\hat{\Psi} = \begin{pmatrix} \psi_{\uparrow\uparrow} & \psi_{\uparrow\downarrow} \\ \psi_{\uparrow\downarrow} & \psi_{\downarrow\downarrow} \end{pmatrix} \tag{2.2}$$

Alternatively, Balian and Werthamer in [7] introduced a vector notation that describes the wavefunction in even more convenient way. As described in Ref. [5], we define a vector $\mathbf{d}$, such that:

$$\mathbf{d}(\hat{\mathbf{k}}) = \frac{1}{2} i \sum_{\alpha\beta} (\hat{\sigma}_2 \boldsymbol{\sigma})_{\alpha\beta} \psi_{\alpha\beta}(\hat{\mathbf{k}}) \tag{2.3}$$

where $\boldsymbol{\sigma}$ is the Pauli vector and $\hat{\sigma}_2 = \left(\begin{smallmatrix} 0 & -i \\ i & 0 \end{smallmatrix}\right)$ is one of the Pauli matrices. Ref. [5] shows that $\mathbf{d}(\hat{\mathbf{k}})$ is related to the total amplitude of condensation of the Cooper pairs at direction $\hat{\mathbf{k}}$ along the Fermi sphere. We refer to $\mathbf{d}(\hat{\mathbf{k}})$ as the vector order parameter of the superfluid condensate. The superfluid gap at each point on the spherical Fermi surface has a magnitude proportional to $\left|\mathbf{d}(\hat{\mathbf{k}})\right|$.

Let us evaluate eq. 2.3 explicitly for the three components of $\mathbf{d}(\hat{\mathbf{k}})$. We obtain:

$$d_x = \frac{1}{2}\left(\psi_{\downarrow\downarrow} - \psi_{\uparrow\uparrow}\right) \tag{2.4}$$

$$d_y = \frac{1}{2i}\left(\psi_{\downarrow\downarrow} + \psi_{\uparrow\uparrow}\right) \tag{2.5}$$

$$d_z = \psi_{\uparrow\downarrow} \tag{2.6}$$

So, for $\hat{\Psi}$ in terms of the components of $\mathbf{d}(\hat{\mathbf{k}})$, we have:

$$\hat{\Psi} = \begin{pmatrix} -d_x + id_y & d_z \\ d_z & d_x + id_y \end{pmatrix} \tag{2.7}$$

Finally, it is also useful to define a 3×3 matrix $\hat{A}$ with components A_{ij} such that:

$$d_i(\hat{\mathbf{k}}) = \sum_{ij} A_{ij}\hat{\mathbf{k}}_j \tag{2.8}$$

The matrix $\hat{A}$ is another way to represent the order parameter.

2.3 Ginzburg-Landau theory

The reason why we defined 3×3 matrix $\hat{A}$ to describe the order parameter becomes apparent in the context of Ginzburg-Landau (GL) theory. Near T_c one can describe the equilibrium superfluid state by finding the matrix $\hat{A}$, which minimizes the appropriate expression for the Ginzburg-Landau free energy, which

at zero magnetic field is given as [8]:

$$F = \alpha \left(\frac{T - T_c}{T_c} \right) \mathrm{Tr}(\hat{A}\hat{A}^\dagger) + \beta_1 \left| \mathrm{Tr}(\hat{A}\hat{A}^T) \right|^2 + \beta_2 \left[\mathrm{Tr}(\hat{A}\hat{A}^\dagger) \right]^2 + \beta_3 \mathrm{Tr} \left[\hat{A}\hat{A}^T (\hat{A}\hat{A}^T)^\dagger \right] + \beta_4 \mathrm{Tr} \left[(\hat{A}\hat{A}^\dagger)^2 \right] + \beta_5 \mathrm{Tr} \left[\hat{A}\hat{A}^\dagger (\hat{A}\hat{A}^\dagger)^* \right] \tag{2.9}$$

where α is related to the density of states at the Fermi surface, and $\hat{A}^T$ refers to the transpose matrix, $\hat{A}^T$ – to the conjugate matrix, $\hat{A}^\dagger$ – to the conjugate transpose matrix. The exact values of the beta coefficients determine the structure of the order parameter. In the limit of weak coupling between the quasiparticles the beta coefficients can be calculated exactly and are given as [9]:

$$\{\beta_1, \beta_2, \beta_3, \beta_4, \beta_5\} = \{-1, 2, 2, 2, -2\} \times \frac{7\zeta(3)}{120\pi^2} \frac{N(\varepsilon_F)}{(k_B T_c)^2} \tag{2.10}$$

Weak coupling limit is a good approximation when the fluid is not pressurized (at saturated vapor pressure), but as we pressurize the fluid the strong coupling corrections become important. The full dependence on pressure of the beta parameters has been inferred by combining the data from a number of experimental sources in Ref. [10].

The general form of the matrix order parameter is:

$$\hat{A} = \begin{pmatrix} A_{xx} & A_{xy} & A_{xz} \\ A_{yx} & A_{yy} & A_{yz} \\ A_{zx} & A_{zy} & A_{zz} \end{pmatrix} \tag{2.11}$$

Depending on which among the values of A_{ij} are nonzero we can have several possible superfluid phases. In the following section we will describe four possible states, only two of which are realized in the bulk.

2.4 Superfluid states

2.4.1 A phase

Proposed first by Anderson and Morel in Ref. [11] and then refined by Anderson and Brinkman in Ref. [12], the A superfluid state (also referred to in the literature as ABM state after the last name initials of Anderson, Brinkman, and Morel) has the following matrix order parameter:

$$\hat{A}_{A-phase} = \sqrt{\frac{3}{2}}\Delta \begin{pmatrix} 1 & i & 0 \\ 0 & 0 & 0 \\ 0 & 0 & 0 \end{pmatrix} \tag{2.12}$$

Since only the x-row of the matrix $\hat{A}$ has nonzero entries, it follows from eq. 2.8 that only the x-component of $\mathbf{d}(\hat{\mathbf{k}})$ is nonzero, with its value given as:

$$d_x = \sqrt{\frac{3}{2}}\Delta \left(k_x + ik_y\right) \tag{2.13}$$

Then from equations 2.2 and 2.7, it follows that $\psi_{\uparrow\uparrow} = -d_x$, $\psi_{\downarrow\downarrow} = d_x$, and $\psi_{\uparrow\downarrow} = 0$. Then the wavefunction for this state is given as:

$$\Psi_{A-phase} = -\sqrt{\frac{3}{2}}\Delta \left(k_x + ik_y\right) |\uparrow\uparrow\rangle + \sqrt{\frac{3}{2}}\Delta \left(k_x + ik_y\right) |\downarrow\downarrow\rangle \tag{2.14}$$

We can see that the spins of the constituents of the Cooper pair are either both up or both down. Thus superfluid A phase is an example of an Equal Spin Pairing (ESP) state.

In terms of the magnitude for the gap at each point of the Fermi sphere, from eq. 2.13 we infer that:

$$\begin{aligned} \left|\mathbf{d}(\hat{\mathbf{k}})\right| &= \sqrt{\frac{3}{2}}\Delta\sqrt{k_x^2 + k_y^2} = \sqrt{\frac{3}{2}}\Delta\sqrt{1 - k_z^2} \\ &= \sqrt{\frac{3}{2}}\Delta\sqrt{1 - \cos^2\theta} = \sqrt{\frac{3}{2}}\Delta \sin\theta \end{aligned} \tag{2.15}$$

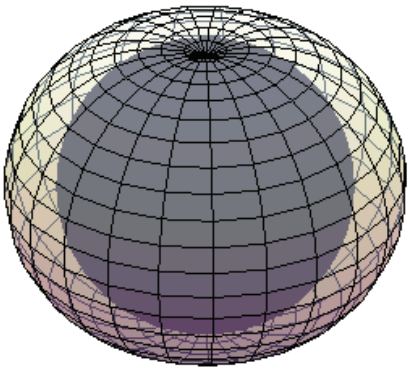

Figure 2.1: Visual representation of the Fermi surface (solid purple) and the superfluid gap (meshed surface) for the A phase.

We see that the value for the superfluid gap is anisotropic, and has nodes at the two poles of the Fermi sphere. Visual representation for the superfluid gap around the Fermi sphere is shown in Fig. 2.1. The anisotropy of the order parameter would lead to anisotropy in the measured superfluid fraction – we would measure larger superfluid fraction if we probe the properties of the superfluid in the equatorial plane, compared to measuring the properties of the superfluid along the polar axis. Furthermore, from 2.14 we see that the wavefunction is an eigenstate of the $\hat{L_+} = \hat{L_x} + i\hat{L_y}$ operator, so the pairs in the A phase will posses an orbital angular momentum of $\boldsymbol{\ell} = \hbar$ pointing in the nodal direction. For a superfluid sample, one can define its "texture" as the vector field of $\boldsymbol{\ell}$ along the sample.

2.4.2 B phase

The B phase (also referred to in the literature as the BW phase) was originally proposed by Balian and Werthamer in Ref. [7]. In the bulk fluid B phase, the matrix order parameter can be diagonalized and for the appropriate choice of

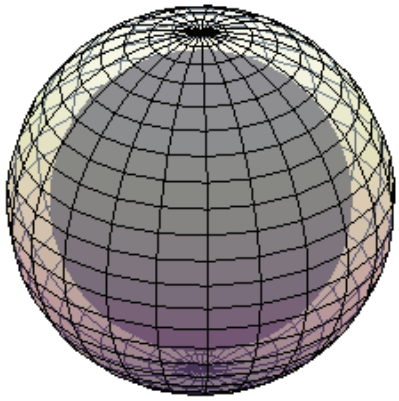

Figure 2.2: Visual representation of the Fermi surface (solid purple) and the superfluid gap (meshed surface) for the B phase.

the orthogonal x, y, and z axes has a form of:

$$\hat{A}_{B-phase} = \Delta \begin{pmatrix} 1 & 0 & 0 \\ 0 & 1 & 0 \\ 0 & 0 & 1 \end{pmatrix} \tag{2.16}$$

Then for the vector order parameter:

$$\mathbf{d}(\hat{\mathbf{k}}) = \Delta \hat{\mathbf{k}} \tag{2.17}$$

and for the $\hat{Psi}$ matrix, we have:

$$\hat{\Psi}_{B-phase} = \Delta \begin{pmatrix} -k_x + ik_y & k_z \\ k_z & k_x + ik_y \end{pmatrix} \tag{2.18}$$

Thus the wavefunction for the Cooper pairs in the B phase is given as:

$$\Psi_{B-phase} = \Delta \left(-k_x + ik_y\right) |\uparrow\uparrow\rangle + \Delta \left(k_x + ik_y\right) |\downarrow\downarrow\rangle + \Delta k_z \left(|\uparrow\downarrow\rangle + |\downarrow\uparrow\rangle\right) \tag{2.19}$$

As we can see all the possible spin state combinations are possible, unlike the A phase. In terms of the size of the gap at any point of the Fermi surface, it will be equal to $\left|\mathbf{d}(\hat{\mathbf{k}})\right| = \Delta$ for all points. Visual representation of the superfluid gap

around the Fermi sphere is shown in Fig. 2.2. The properties of the superfluid are uniform in all directions in the bulk B phase. Also, unlike the A phase, there is no angular momentum of the Cooper pairs in this state.

2.4.3 Polar phase

Let us go back to the form of the matrix order parameter of the A phase (Eq. 2.12). Now, let us allow the off-diagonal term A_{xy} diminish to zero (from i in the A phase). We have a smooth transition from A phase to what we refer to as the Polar phase. We define the matrix order parameter for the Polar state as:

$$\hat{A}_{Polar} = \Delta_{Polar} \begin{pmatrix} 1 & 0 & 0 \\ 0 & 0 & 0 \\ 0 & 0 & 0 \end{pmatrix} \tag{2.20}$$

This means that the vector $\mathbf{d\hat{k}}$ only has a component in the $\hat{\mathbf{x}}$ direction, $d_x = \Delta_{Polar} k_x$. Then the matrix $\hat{Psi}$ becomes:

$$\hat{\Psi}_{Polar} = \Delta_{Polar} \begin{pmatrix} -k_x & 0 \\ 0 & k_x \end{pmatrix} \tag{2.21}$$

And the wavefunction for the Cooper pairs:

$$\Psi_{Polar} = -\Delta_{Polar} k_x \left|\uparrow\uparrow\right\rangle + \Delta_{Polar} k_x \left|\downarrow\downarrow\right\rangle \tag{2.22}$$

Thus the Polar phase, similarly to the A phase, is also an Equal Spin Pairing (ESP) state. However, unlike the A phase, there is no angular momentum associated with the Polar phase Cooper pair.

The magnitude of the superfluid gap along the Fermi surface is given as:

$$\left|\mathbf{d\hat{k}}\right| = \Delta_{Polar} |k_x| = \Delta_{Polar} \cos\alpha \tag{2.23}$$

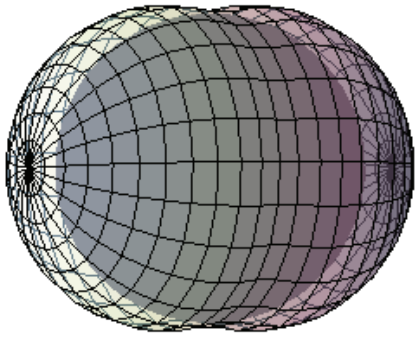

Figure 2.3: Visual representation of the order parameter of the Polar phase

where α is the angle between the vector $\hat{\mathbf{k}}$ and the x-axis. Visual representation for the superfluid gap for the Polar phase is shown in Fig. 2.3. We can see that the two nodal points of the A-phase transformed into a nodal line connecting them. If we call the two points of where the Fermi sphere intersects the x-axis poles, then the nodal line is along the equator. Superfluid fraction measured in the y-z plane will be strongly suppressed (but not entirely zero).

2.4.4 Planar phase

Finally, we consider a state that has two of the diagonal terms being nonzero, and all the other terms of the matrix order parameter being zero:

$$\hat{A}_{Planar} = \Delta_{Planar} \begin{pmatrix} 1 & 0 & 0 \\ 0 & 1 & 0 \\ 0 & 0 & 0 \end{pmatrix} \tag{2.24}$$

Then for the vector $\mathbf{d}(\hat{\mathbf{k}})$ we have:

$$\mathbf{d}(\hat{\mathbf{k}}) = \Delta_{Planar} k_x \hat{\mathbf{x}} + \Delta_{Planar} k_y \hat{\mathbf{y}} \tag{2.25}$$

Then the magnitude for the gap at each point of the Fermi sphere can be inferred as:

$$\left|\mathbf{d}(\hat{\mathbf{k}})\right| = \Delta_{Planar}\sqrt{k_x^2 + k_y^2} = \Delta_{Planar}\sin\theta \tag{2.26}$$

The expression in 2.26 is exactly the same as 2.15 for the A phase. So just like in the A phase, the superfluid gap distribution around the Fermi sphere is represented in Fig. 2.1.

For the Planar state the matrix $\hat{Psi}$ becomes:

$$\hat{\Psi}_{Planar} = \Delta_{Planar}\begin{pmatrix} -k_x + ik_y & 0 \\ 0 & k_x + ik_y \end{pmatrix} \tag{2.27}$$

which gives for the Cooper pair wavefunction:

$$\Psi_{Planar} = -\Delta_{Planar}(-k_x + ik_y)\left|\uparrow\uparrow\right\rangle + \Delta_{Polar}(k_x + ik_y)\left|\downarrow\downarrow\right\rangle \tag{2.28}$$

The Planar phase is also an Equal Spin Pairing (ESP) state like the A and Polar phases, and like the Polar state it differs from the A phase in the fact that it has no angular momentum associated with the Cooper pair state.

2.5 Calculating the superfluid fraction

Knowing the order parameter for the superfluid, and hence the superfluid gap distribution above the Fermi sphere, we can calculate the superfluid fraction in the plane of the torsion pendulum head starting from [8]:

$$\rho^0_{n\,ij} = 3\rho\left\langle \hat{\mathbf{k}}_i\hat{\mathbf{k}}_j Y_0(\hat{\mathbf{k}}, T)\right\rangle_{\hat{\mathbf{k}}} \tag{2.29}$$

$$\boldsymbol{\rho}_n = \frac{m^*}{m}\left(\mathbf{1} + \frac{1}{3}F_1^s\frac{\boldsymbol{\rho}_n^0}{\rho}\right)^{-1}\rho_n^0 \tag{2.30}$$

where $\boldsymbol{\rho}_n$ and $\boldsymbol{\rho}_n^0$ are 3 by 3 matrices with components $\rho_{n\,ij}$ and $\rho^0_{n\,ij}$ respectively, m^* is the renormalized mass of ^{3}He quasiparticles, and F_1^s is the Landau parameter. $Y_0(\hat{\mathbf{k}}, T)$ is the Yosida function, which is related to the energy density distribution along the Fermi sphere, f:

$$Y_0(\hat{\mathbf{k}}, T) = -\int_{-\infty}^{\infty} d\epsilon_{\hat{\mathbf{k}}} \left(\frac{\partial f}{\partial E_{\hat{\mathbf{k}}}} \right) \tag{2.31}$$

with the information for the gap structure contained in $^{\partial f}/_{\partial E_{\hat{\mathbf{k}}}}$. Torsion pendulum experiments probe the superfluid fraction in the $\hat{\mathbf{x}}$ - $\hat{\mathbf{y}}$ plane. Thus, the measured superfluid fraction is given by:

$$\rho_{s\,\text{in plane}} = \rho - \frac{\rho_{n\,xx} + \rho_{n\,yy}}{2} \tag{2.32}$$

2.6 Bulk superfluid phase diagram

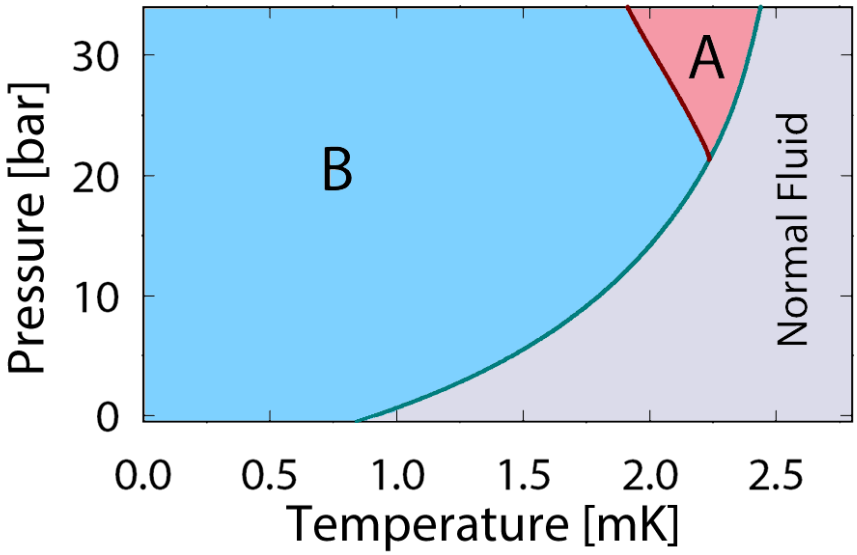

Figure 2.4: Superfluid phase diagram of bulk ^{3}He

Experimentally determined phase diagram for the bulk fluid is shown in Fig 2.4. Values for the transition temperatures are taken from Ref. [13]. Most of

it is occupied by the B superfluid phase, which is the equilibrium state at low pressures. The A phase is stable at high pressures and at temperatures near the superfluid transition temperature. Superfluid transition is a second order phase transition, while the transition between the A and B phase is a first order [14] and tends to supercool. There exists a polycritical point at which the superfluid transition and A-B transition lines intersect at $P_{pcp} = 21.22$ bar. Polar phase and Planar phase are not stable and have not been observed in the bulk.

The free energies of the bulk A and B phases are very close and the equilibrium state can be changed by applying moderate magnetic fields [15]. The field creates an axis of anisotropy and hence promotes the stability of the anisotropic A phase over the isotropic B phase. The field destroys the polycritical point and the A phase is observed in a sliver near T_c all the way to 0 bar pressure. Very close to T_c at high fields another state, referred to as A_1 is realized, however, discussion of this state is beyond the scope of this work.

2.6.1 Coherence length

Everything we have discussed so far is relevant for the bulk fluid far from any surfaces. However, surfaces and confinement will modify the properties of the superfluid as it will be shown in the following chapters.

The length scale at which the surface effects become important is related to the superfluid coherence length, $\xi(P, T)$. The coherence length is related up to a numerical factor to the average distance between two fermions in the Cooper pairs. The coherence length parametrizes the length scale over which the order parameter can exhibit significant changes.

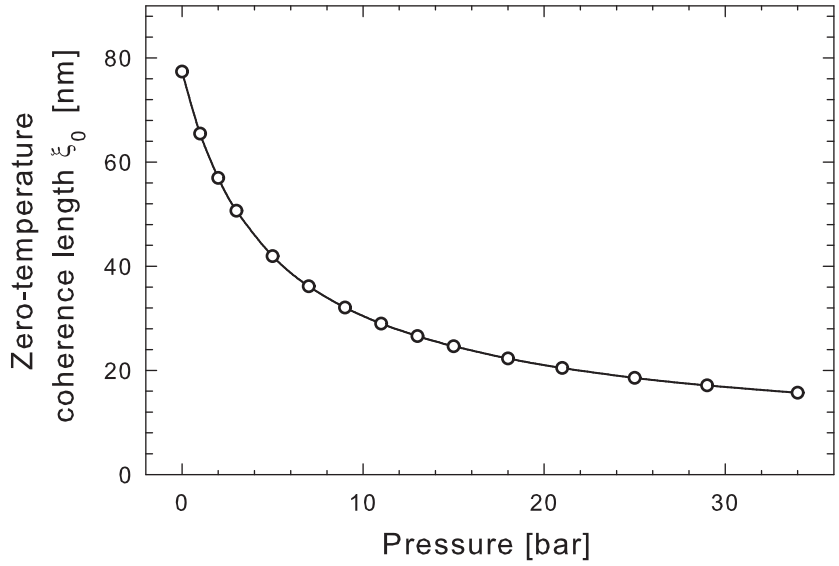

Figure 2.5: Plot of the zero temperature coherence length versus pressure.

At $T = 0$ the zero-temperature coherence length is defined as:

$$\xi_0(P) = \frac{\hbar\, v_F(P)}{2\pi k_B\, T_c(P)} \tag{2.33}$$

with v_F being the Fermi velocity and T_c the superfluid transition temperature. A plot for ξ_0 versus pressure is shown in Fig. 2.5. Ginzburg-Landau theory predicts that the coherence length should diverge near T_c as $(1 - T/T_c)^{-1/2}$, so in accordance with Ref. [16], we can define:

$$\xi_{tr}(T) = \left[\frac{7\zeta(3)}{20}\right]^{-1/2} \xi_0 \left(1 - \frac{T}{T_c}\right)^{-1/2} \tag{2.34}$$

where the Riemann zeta function $\zeta(3) \approx 1.2$. We can also define the temperature dependence of the coherence length by relating it to the size of the superfluid gap of the B phase, as was done in Ref. [17]. Using the definition used by Lev Levitin in Ref. [18], we can define:

$$\xi_\Delta(T) = \frac{\hbar v_F}{\sqrt{10}\Delta_B(T)} \tag{2.35}$$

The relationship between ξ_{tr} and ξ_Δ is shown in Fig. 2.6

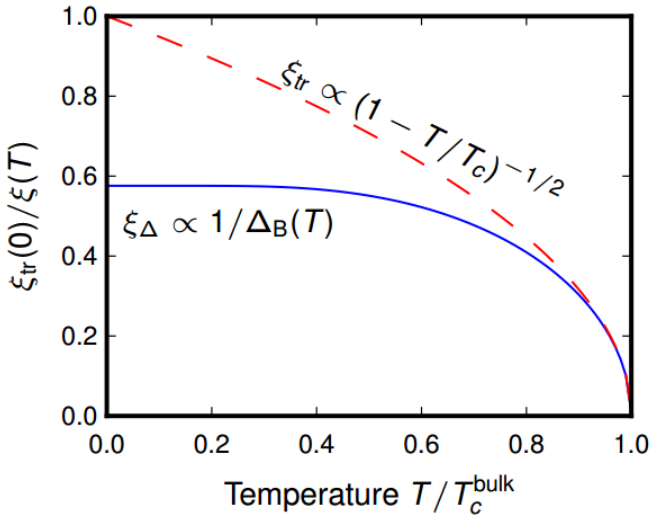

Figure 2.6: Plot of the zero temperature coherence length versus pressure. Courtesy of the supplementary information from Ref. [18].

CHAPTER 3

^{3}HE IN AEROGEL

3.1 Motivation: "Dirty" Superfluid

Bulk ^{3}He is exceptionally pure and free of disorder. Unlike solid crystalline samples, there is no crystal lattice, and hence there are no crystal lattice defects can scatter the quasiparticles. By the time we reach the temperatures the experiments with ^{3}He are performed (< 100 mK), any other impurity that we could have tried to mix in with the fluid would have long condensed at the walls of the experimental cell. Due to different quantum statistics between ^{4}He and ^{3}He, the solubility of ^{4}He in ^{3}He is vanishingly small at milli-Kelvin range temperatures – about one mole in a volume as large as the observable universe [8], and any appreciable amount of ^{4}He would phase separate, leaving an exceptional pure ^{3}He phase.

Normally, disorder is a nuisance. It leads to troubles when comparing and interpreting results from different experiments done on samples with varying amounts of purity or defects, since material properties can be very sensitive to disorder. For example, the onset of the superconducting transition and the nature of the superconducting state in unconventional superconductors, such as Sr_2RuO_4 and UPt_3, are greatly affected by the presence of disorder [19, 20]. In fact, the suppression of the superfluid transition temperature in these materials by nonmagnetic impurities is a tell-tale sign for "exotic" non s-wave pairing [21].

There are, however, compelling reasons to attempt introducing disorder in

the otherwise pristine ^{3}He. If we want to use ^{3}He as a model system for unconventional superconductors then we might want to attempt to make the parallel between the "dirty" superconducting samples and the superfluid ^{3}He closer by "dirtying" the superfluid. Moreover, the exceptional purity of the bulk fluid provides an unique baseline system that can be compared to a subsequently dirtied one to investigate exactly how the added disorder influences the superfluid properties.

At present, the only way to introduce disorder in ^{3}He is by embedding the fluid within a highly porous aerogel. First experiments investigating the properties of the aerogel embedded fluid – by Porto and Parpia at Cornell [22] and by the Halperin group at Northwestern [23] revealed remarkable differences compared to the properties of the bulk superfluid. Many more similar experiments followed that explored the properties of the "dirty" superfluid. Ref. [24] provides a comprehensive review of all recent experimental results.

3.2 Aerogel Structure

Aerogel samples tend to have a fractal-like micro structure composed of highly interconnected strands [25]. For the majority of these experiments, the aerogel samples are made out of silica and have densities $\approx 2\%$ of the density of solid silica. In other words, $\approx 98\%$ of the space within the sample is occupied by voids. An image of a silica aerogel sample is shown in Fig. 3.1 Typical size of the aerogel strands is estimated to be a few nanometers (~ 5 nm). Distance between strands is of the order of ~ 100 nm. The micro structure of the aerogels can

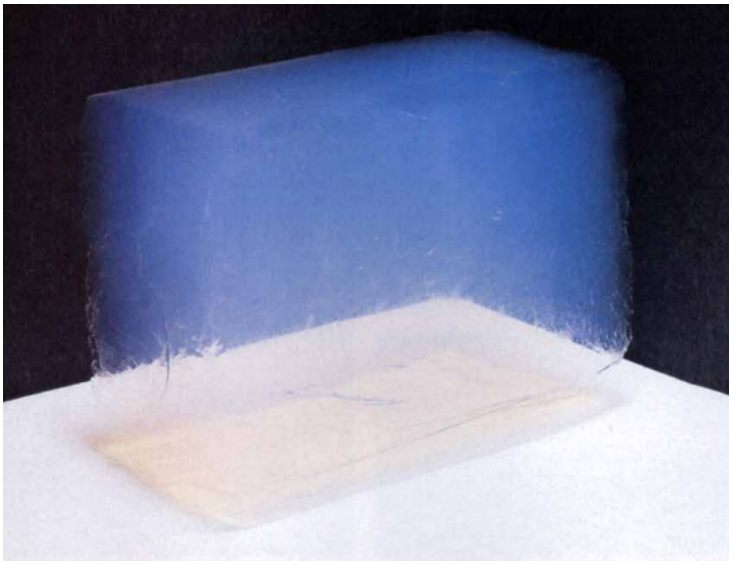

Figure 3.1: Image of a silica aerogel sample. Courtesy of Ref. [25]

be accurately modeled using diffusion-cluster-aggregation (DLCA) models [26] and experimentally verified through small angle X-ray scattering experiments [26, 41]. Fig. 3.2, panel (a) shows results from the DLCA simulations from [26] that accurately represent the correlated structure of the aerogel at small length scales. Solid matter accumulates into interconnected filament like structures, leaving large voids in between. This is contrasted in panel (b) with a randomly assembled solid matter with the same final density that would not form such correlated structure. An environmental ESEM image of a silica aerogel sample taken from Ref. [27] is shown in Fig. 3.3 in which we can see the real micro structure of the sample. Beyond the size of the aerogel strands and the typical size of the voids, we can also define the aerogel correlation length ξ_a. The parameter ξ_a defines the length scale at which the structure of the aerogel becomes inhomogeneous. For a typical silica aerogel sample $\xi_a \sim 50 - 100$ nm. .

Finally, the most important parameter that determines the behavior of the embedded fluid is the mean-free path for the quasiparticles they travel before

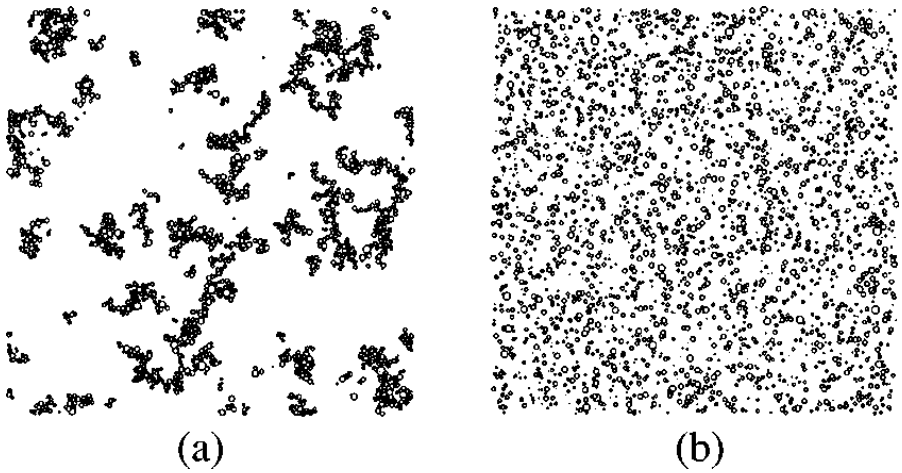

Figure 3.2: Panel (a) shows a 350 nm $\times$ 350 nm $\times$ 30 nm slice of a DLCA simulation for the aerogel structure. At such length scales, the inhomogeneity of the aerogel is revealed. Panel (b) shows a slice of the same size for a simulation that assumes random distribution of the solid matter. Courtesy of Ref. [26]

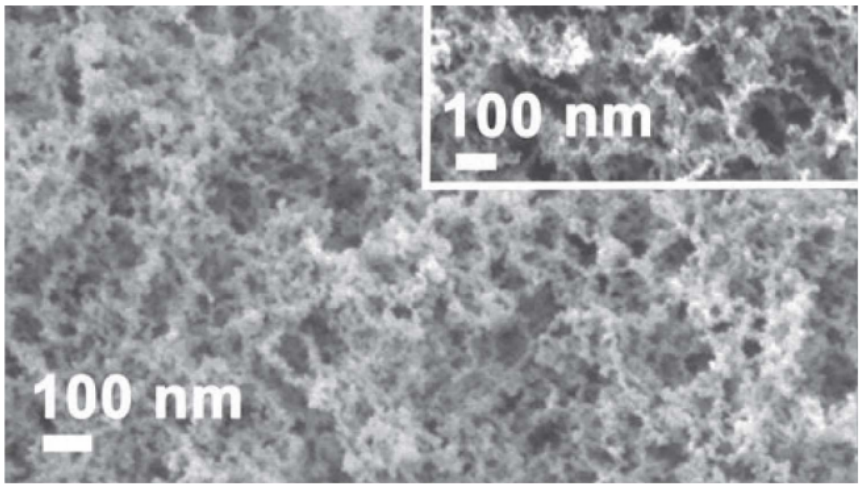

Figure 3.3: Environmental SEM image of a silica aerogel sample. Courtesy of Ref. [27]

they collide with an aerogel strand. A number of experimental properties, such as spin diffusion, thermal conductivity and viscosity of normal ^{3}He are directly related to the mean-free path of the quasiparticles in the fluid. Transport measurements in the normal Fermi liquid, such as spin diffusion [28, 29], thermal conductivity [30, 31], and viscosity [32] reveal a crossover from a regime in which the mean-free-path of the quasiparticles is determined by the elastic scattering rate off other quasiparticles to a regime where the mean-free-path is determined by the inelastic scattering rate off the aerogel strands. A relationship for the mean-free-path exists of the form:

$$\frac{1}{\lambda_{eff}} = \frac{1}{\lambda_{qp-qp}} + \frac{1}{\lambda_{aerogel}} \tag{3.1}$$

Typical values for $\lambda_{aerogel}$ for silica aerogels are of the order of $100 - 200$ nm.

3.3 Properties of the superfluid within the aerogel

In the ^{3}He-aerogel composite system, the ^{3}He quasiparticles are always within a distance of the order of the coherence length away from an aerogel strand. As will be shown in the next chapter, superfluid order parameter is suppressed near a surface. If the aerogel strands acted like conventional surfaces the superfluidity will be entirely suppressed. The reason why superfluidity persists is due to the strands being much smaller than the coherence length. While we can still observe superfluid order, the scattering from the aerogel strands will lead to suppression of the superfluid gap. Ref. [33] theoretically calculated the density of states versus energy for the embedded superfluid. Results from their calculations are shown in Fig. 3.4. Two limits were investigated: Unitary – in which the quasiparticles are strongly scattered off the aerogel strands, and Born

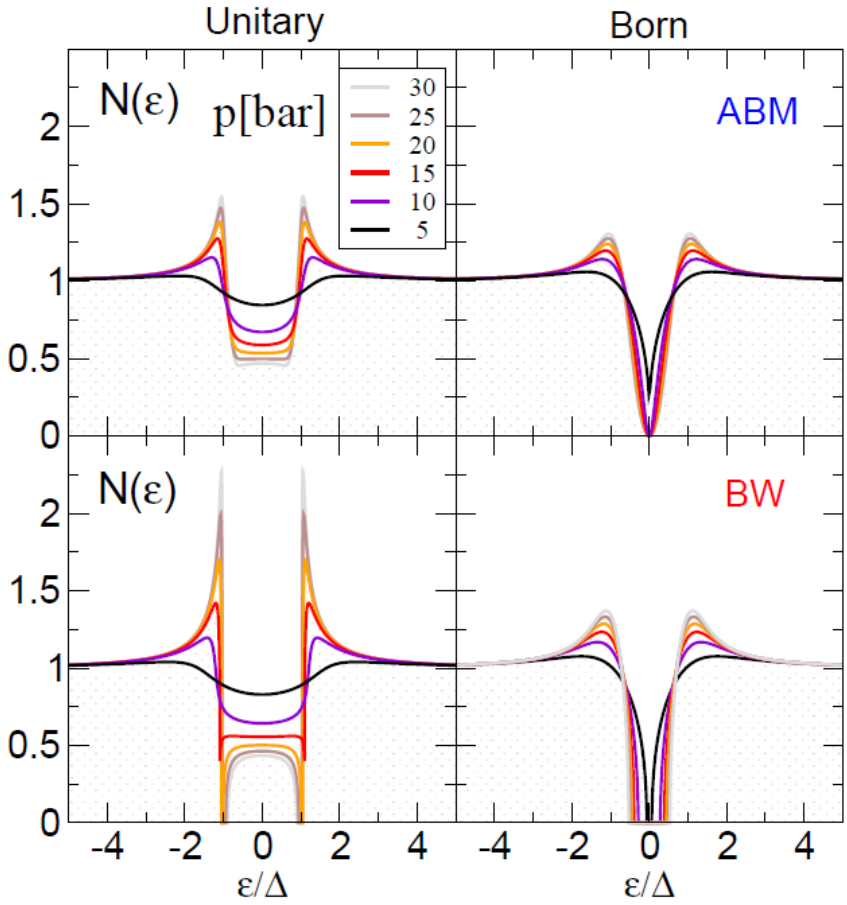

Figure 3.4: Theoretical calculations of the density of states for ABM- and BW order parameters with aerogel scattering. The mean-free path is $\ell = 180$ nm and the scattering is in both the unitary and Born limits. Courtesy of Ref. [33]

– in which the scattering is weak. The real system will have properties between these two limits. In all cases, the theoretical predictions reveal that a spectrum of low energy excitations inside the gap appear. The presence of these "mid-gap" states could lead to "gapless superfluidity," a situation in which the density of states does not go to zero in the superfluid gap above the Fermi surface, instead the density of states at those energy levels is merely suppressed compared to the density of states in the normal phase. Evidence for "gapless superfluidity" and the modification of the superfluid gap by disorder has been demonstrated

in thermal conductivity [34] and heat capacity measurements [35].

3.3.1 Superfluid phase diagram for ^{3}He in anisotropic aerogel

Despite the difference between the aerogel samples in the different experiments which mapped the "dirty" superfluid phase diagram, it is clear that the phase digram is radically different from that in the bulk.

Superfluid transition is suppressed for the fluid embedded in the aerogel. Theoretical models which have proved to well describe T_c-suppression observed in various experiments is proposed in Ref. [36]. Superfluid transition suppression is most sensitive to the ratio of the mean-free path of the quasiparticles within the aerogel ($\lambda_{aerogel}$ in eq. 3.1) and the zero temperature coherence length (ξ_0, see eq. 2.33 for definition). In fact, at low pressures where the zero temperature coherence length grows larger, and hence $\lambda_{aerogel}/\xi_0$ is smaller, superfluidity may be entirely extinguished. For dense enough aerogels, evidence for a quantum phase transition has been observed at $T = 0$ [37]. For pressures below the quantum critical point ^{3}He never becomes superfluid.

The regions of stability between the superfluid A and B phases are also severely modified by the disorder. Fig. 3.5 shows the phase diagram that was determined for a 98.2% open aerogel sample upon warming as reported by Ref. [38]. We see that unlike in bulk upon warming the entire phase diagram is occupied by the B phase.

On the other hand, upon cooling the A phase appears in wide sliver at high pressures which extends to pressures well below the pressure of the polycritical

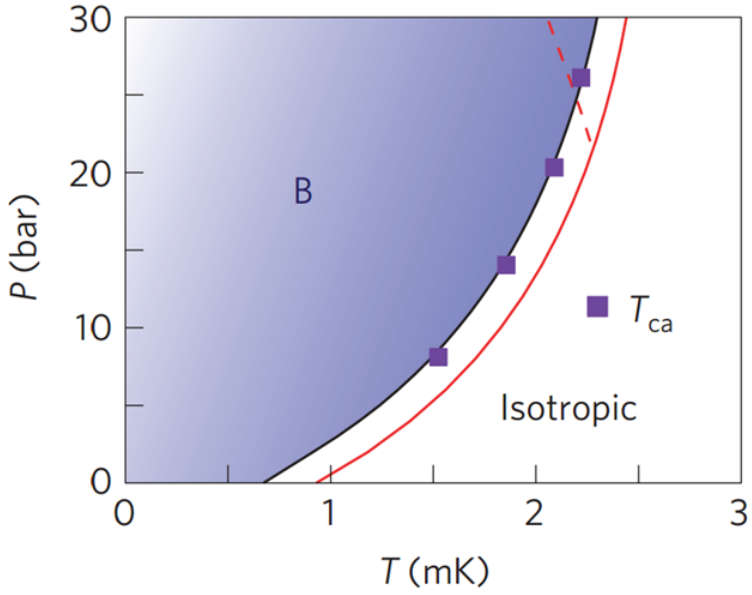

Figure 3.5: Phase diagram upon warming for a 98.2% open aerogel isotropic silica aerogel sample. Aerogel was grown in Northwestern University. Figure courtesy of Ref. [38]

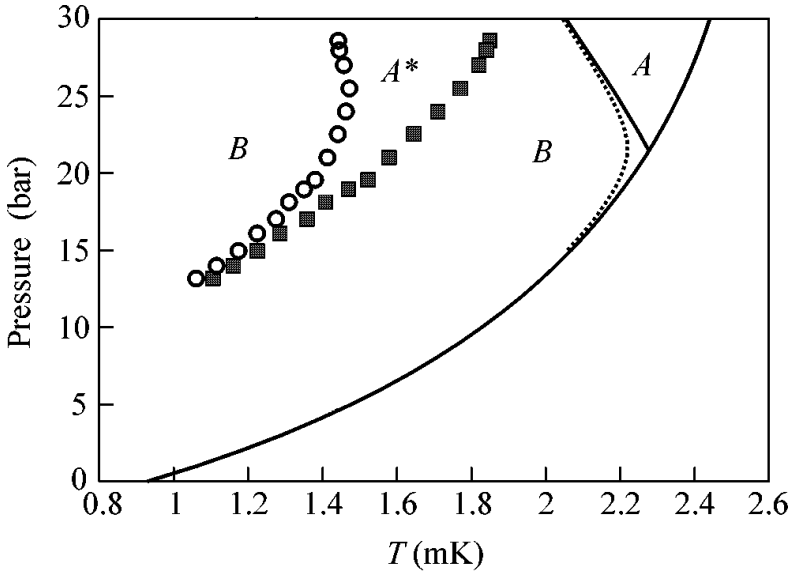

Figure 3.6: phase diagram upon cooling for a 98% open silica aerogel sample. Aerogel was grown in University of Delaware by the group of N. Mulders. Figure courtesy of Ref. [39]

point. The polycritical point is destroyed, there is a thin region of stability of A phase all the way down to the lowest pressures for which superfluidity can be observed. Fig. 3.6 summarizes the experimental phase diagram for a different 98% open silica aerogel sample upon cooling.

While metastability and supercooling of the A phase is observed in bulk, the degree of hysteresis between cooling and warming is strongly enhanced by the presence of disorder. In bulk, it is the B to A transition of warming that occurs at the thermodynamically predicted temperature. Since A phase is not observed on warming for isotropic aerogel samples, we can conclude that the thermodynamically stable phase for all pressures and temperatures is only the B phase. A phase is likely thermodynamically stable only in an extremely thin sliver right below the superfluid transition, and its metastability is due to large degree of supercooling.

3.4 Anisotropic disorder through aerogel compression

In the bulk, providing an axis of anisotropy via exposing the ^{3}He sample to magnetic field enhances the stability of the anisotropic A phase. We would like to investigate whether providing an axis of anisotropy via the aerogel could produce similar effect. Interest in such a system was spurred by Ref. [40]. It was predicted that anisotropic disorder will stabilize the anisotropic A phase, and this state will appear on both cooling and warming unlike the case of isotropic aerogels. What sparked even more interest was the prediction that very close to T_c, the Polar phase, a state not seen in the bulk, might be observed.

One way to produce anisotropy in the aerogel is to deforming it after its

growth. Stretching the fragile sample is experimentally non-trivial, but large degree of compression of the aerogel can be achieved post growth. Carefully squeezing the aerogel by 10 - 20 % has been demonstrated to reduce the spacing between the aerogel strands in the compression axis direction [41]. One can achieve an equivalent stretching by radial compression; radial compression is equivalent to an uniaxial stretching of a slightly denser sample. A number of experiments by our collaborators at Northwestern University were done with stretched samples. At Cornell, we concentrated our attention to studying a 10 % uniaxially compressed aerogel, for which we aimed to explore the phase diagram.

The texture (vector field of the angular momentum vectors ℓ of the Cooper pairs) of the supercooled superfluid A phase is predicted to be different for the fluid embedded within the aerogel compared to the bulk fluid. In particular, G. Volovik in Ref. [42] predicts that while the texture is oriented on short length scales, no long range order exists for the direction of ℓ within the aerogel. This is what is referred to as the Larkin - Imry - Ma (LIM) state, and represents a glassy state for the spin/angular momentum orientation of the superfluid. This prediction was experimentally verified in Ref. [43].

Volovik predicts that when axis of anisotropy is present by squeezing the aerogel, the LIM state would be destroyed and the long range order restored. Modeling the aerogel as a collection of rigid cylinders, he predicts that the the axis of compression will provide an "easy axis" parallel to which the ℓ vector will be oriented along. On the other hand, J. Sauls using symmetry arguments, argues that the ℓ vector will orient itself perpendicularly to the axis of compression in the "easy plane" [44]. We would like to investigate which of these two

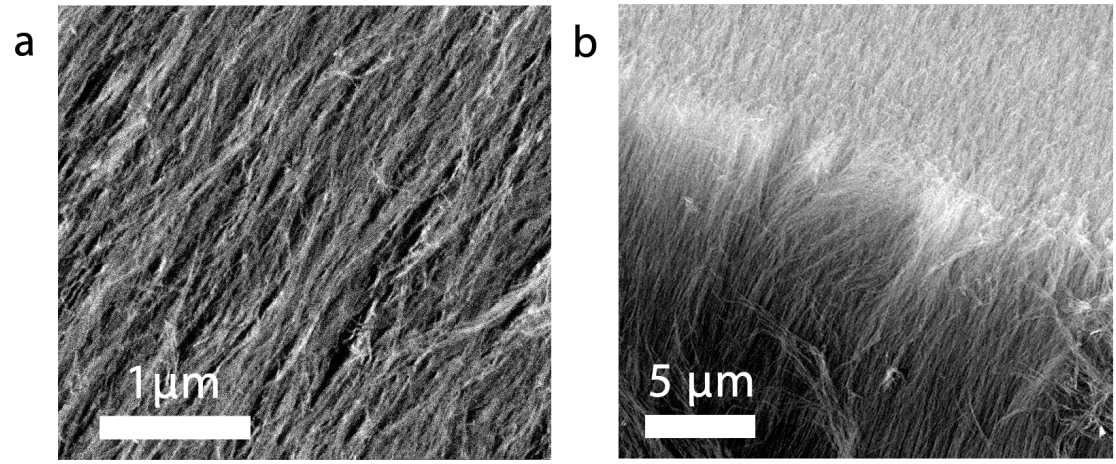

Figure 3.7: a) SEM image in a plane parallel to the aerogel strands.
b) SEM image of the edge of the aerogel sample at the intersection of planes parallel and perpendicular to the strands.

models is correct.

3.5 *Nematically ordered* aerogel

A new type of aerogel recently became available. Unlike the aerogels we have discussed so far, which were made from silica, this new type of aerogel is composed of alumina strands. What is remarkable about it is that the strands are all strongly oriented in a particular direction. Fig. 3.7 shows an SEM image of the oriented alumina aerogel. The image shows the extremely anisotropic structure of the aerogel. Because the aerogel is composed of long thin strands all mostly parallel to each other, we refer to this type of aerogel as *nematically ordered* aerogel.

The *nematically ordered* aerogel was grown by a group in Leypunsky Institute for Physics and Power Engineering in Obninsk, Russia. This type of aerogel is

also referred to by other references as the Obninsk aerogel. The aerogel is grown by dissolving aluminum in molten gallium. Then by flowing water vapor over the melt, the aluminum is oxidized and aluminum oxide strands are precipitated on the surface producing the *nematically ordered* aerogel structure. The density of the aerogel sample that experiments in the latter part of this work were carried on is ~ 30 mg/cm^3. The size of the alumina strands is ≈ 10 nm and average distance between the strands is ~ 100 nm. More information on the method of growth and the physical properties of the Obninsk aerogel can be found in Ref. [45].

We can consider this type of aerogel as the extreme case of the deformed (stretched or compressed) aerogels considered in the previous section. In particular, the *nematically ordered* aerogel would correspond to the limit of nearly infinite stretching.

CHAPTER 4

CONFINED SUPERFLUID ^{3}HE

We are interested in studying the effects of surfaces on the superfluid. To do that we confine the superfluid ^{3}He within nanofabricated geometries. In this chapter, I plan to do a brief review of the expected modifications of the order parameter imposed by being in the vicinity of a surface, the expected modification of the phase diagram by the confinement and conclude with a brief review of previous experimental results.

4.1 Superfluid order parameter near a surface

Shortly after the discovery of the superfluidity of ^{3}He, Ambegaokar, de-Gennes and Rainer considered the case of what happens to the superfluid order near a surface [16]. They argued that the component of the vector order parameter $\mathbf{d}(\hat{\mathbf{k}})$ perpendicular to the surface should be suppressed at the surface. What happens to the components of $\mathbf{d}(\hat{\mathbf{k}})$ parallel to the surface plane depends on the surface specularity. A perfectly specular surface acts like a mirror – a quasiparticle reflected off has its parallel component unchanged, and the component perpendicular to the surface has its sign reversed. In the other limit, we have diffuse reflection – the momentum of the reflected quasiparticle is random after the reflection.

Since the B phase order parameter has nonzero values in all directions, including perpendicular to the surface, the stability of the B phase will be disrupted. The anisotropic A phase should occupy a much larger portion of the phase diagram compared to the bulk. The angular momentum vector ℓ should

be oriented normal to the surface so that the node of the order parameter points in that direction. In that sense, the texture of the superfluid will be locked.

To explore the quantitative surface effects on the order parameter, we would like to rewrite the momentum unit vector $\hat{\mathbf{k}}$ in cylindrical coordinates. We choose our axes, such that the z-axis is perpendicular to the surface, and the angle ϕ is the azimuthal angle with respect to the y-axis. Then we have:

$$\begin{pmatrix} k_x \\ k_y \\ k_z \end{pmatrix} = \begin{pmatrix} \Delta_{\parallel} \sin\phi \\ \Delta_{\parallel} \cos\phi \\ \Delta_{\perp} \end{pmatrix} \tag{4.1}$$

The expressions for the Cooper pair wavefunction for the A and B phases respectively (Eq. 2.14 and 2.19) become:

$$\Psi_A = i\Delta_{\parallel}^A e^{-i\phi}\left(|\uparrow\uparrow\rangle + |\downarrow\downarrow\rangle\right) \Psi_B = i\Delta_{\parallel}^B e^{i\phi}|\uparrow\uparrow\rangle + i\Delta_{\parallel}^B e^{-i\phi}|\downarrow\downarrow\rangle + \Delta_{\perp}^B\left(|\uparrow\downarrow\rangle + |\downarrow\uparrow\rangle\right) \tag{4.2}$$

In the bulk $\Delta^A = \sqrt{3/2}\Delta^B$ and the values for the the parallel and perpendicular components of Δ^B are the same. Near a surface, however, the B-phase becomes distorted and we expect that $\Delta_{\perp}^B < \Delta_{\parallel}^B$.

Calculations for the suppression of the components of the order parameter near a surface for both A and B phases were done by Nagato, Yamamoto, Nagai in Ref. [46]. Their results are shown in Fig. 4.1. In their calculation they use a diffusivity parameter W: $W = 0$ corresponds to specular surface, and $W = 1$ corresponds to diffuse. We can see that the B phase should transform into Planar phase at the surface and into a planar-distorted B phase away from the surface. The effect of the surface is felt for about a distance of about five coherence lengths.

More recently, Vorontsov and Sauls calculated the suppression of the order

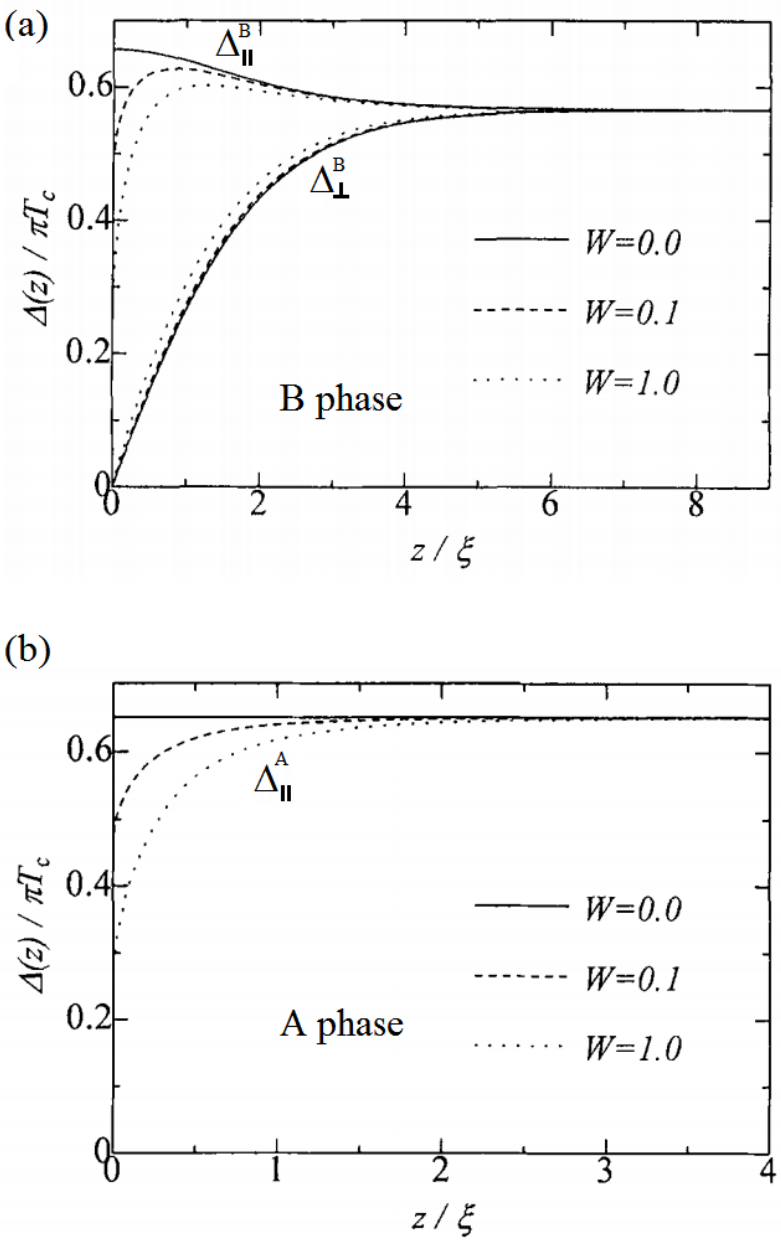

Figure 4.1: Order parameter near a surface. Parameter W refers to the diiffusivity of the surface; for specular reflection, we have W = 0; for diiffuse W = 1.
Plot on the top: A-phase order parameter perpendicular to the surface is zero. Parallel component is same as in bulk for specular, and suppressed near surface for diiffuse reflections.
Plot on the bottom: B-phase order parameter is suppressed near the surface. The perpendicular component is enhanced for specular, or suppressed for diffuse reflection. Near the surface, it is always true that $\Delta_{\perp} < \Delta_{\parallel}$. Plot courtesy of Ref. [46].
ξ is a the temperature dependent coherence length.

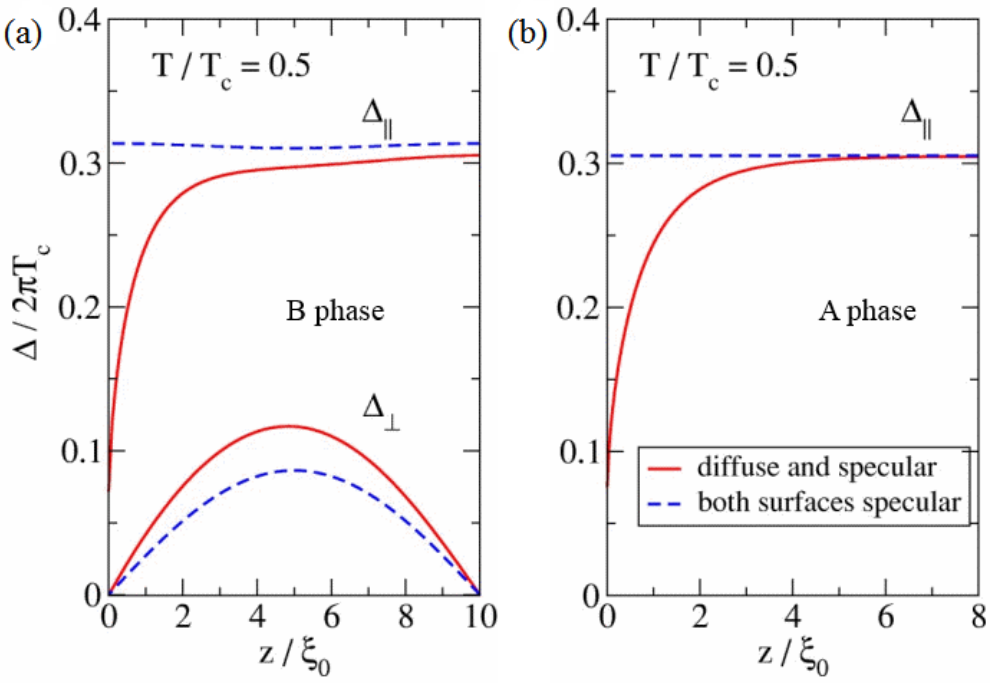

Figure 4.2: Order parameter values across a slab with one surface of the slab being specular and the other being diffuse (red solid line) or two specular surfaces (blue dashed line).
Calculation for a $10\xi_0$ thick slab and B phase fluid shown on the left (panel (a)).
Calculation for a $8\xi_0$ thick slab and A phase fluid shown on the right (panel (b)).
In all cases temperature is assumed to be $0.5T_c$. Source: Ref. [2]

parameter components in two different geometries: a film bounded by a diffuse and a specular surface (this would model a film adsorbed on a solid surface), and a film bounded by two specular surfaces [2]. Their results calculated in the weak coupling limit (zero bar) are shown in Fig. 4.2. Their results qualitatively agree with the calculations in Ref. [46]

4.2 Phase diagram for a thin slab

The experimental geometry we plan to study is that of ^{3}He confined to a high aspect ratio cavity with height $D \ll$ the width and length. The confined fluid will have the shape of a thin slab. A simple schematic outlining the experimental geometry is shown in Fig. 4.3.

As was shown in Eq. 2.33, the zero-temperature coherence length, ξ_0 is pressure dependent. Therefore, while the thickness of the slab D is fixed, we can still vary the effective confinement D/ξ_0 by varying the pressure. A phase diagram can be constructed by plotting the confinement parameter D/ξ_0 on the x-axis and the normalized temperature T/T_c on the y-axis. Such a phase diagram, proposed by Vorontsov and Sauls [2], is shown in Fig. 4.4. In the figure the superfluid transition temperature is marked as T_{AN}. If the fluid is bounded by a diffusive surface, one expects that the superfluid transition temperature will be suppressed. A model for the superfluid transition temperature suppression was developed by Kjäldman, Kurkijärvi and Rainer (KKR model) [47]. For films thicker than $\sim 6\xi_0$, bounded by two diffuse surfaces, they predict:

$$T_c^{slab} = T_c \exp\left(-\frac{\pi^2 \xi_0^2}{D^2}\right) \tag{4.3}$$

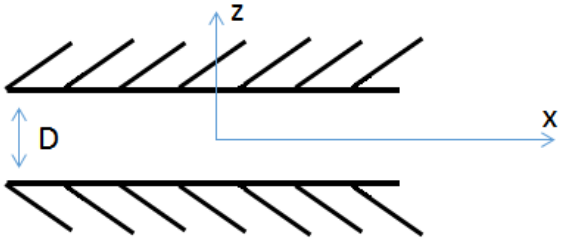

Figure 4.3: Schematic of the sample geometry. The fluid is confined to a thin slab within a cavity with a thickness $D \ll$ Width or Length.

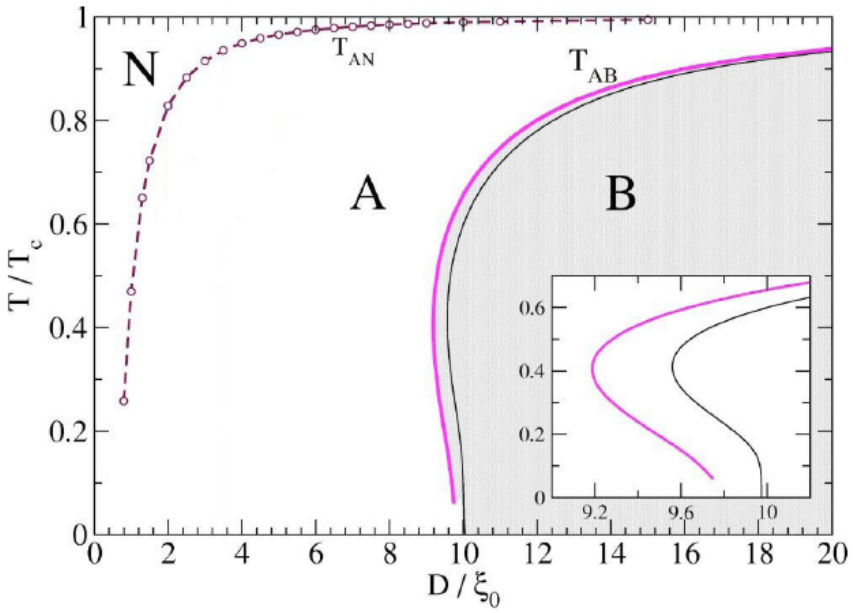

Figure 4.4: Phase diagram for the expected phase diagram for a slab with thickness D at 0 bar pressure. The bottom axis represents the degree of confinement parametrized by D/ξ_0. Black solid line separates the regions of stability for the A and B phases when one of the surfaces is diffuse and the other specular. Solid magenta line is for the case of two specular surfaces. Dashed purple line shows the superfluid transition suppression expected for the case of one diffuse and one specular surfaces.
Inset shows an enlarged portion of the A-B phase boundary, at the region where a reentrant A phase is predicted to appear.
Source: Ref. [2]

where T_c^{slab} is the transition temperature for the confined fluid (same as T_{AN}), and T_c is the bulk superfluid transition temperature. KKR model also predicts that superfluid transition temperature would not be suppressed by specular surfaces. The calculated values by Vorontsov and Sauls for a film with one diffusive and one specular surface agree with the KKR model provided that the thickness of the film is doubled. In other words, an adsorbed film on a solid surface with one free surface is equivalent when it comes to T_c suppression to a film twice the size confined between two diffusive surfaces.

In the weak coupling limit, Vorontsov and Sauls predict that the A phase and Planar phase will be degenerate, but the degeneracy is lifted in favor for the A phase when strong coupling corrections are factored in. At any rate, the A phase will be the only stable phase for thin slabs for all temperatures. As the thickness of the slab is increased, the A - B transition is recovered, with the A phase being the stable phase right below T_c and B phase appearing a lower temperatures. The A to B transition temperatures are shown in Fig. 4.4. The stability of the A phase is enhanced by having fully specular surfaces, that is because specular surfaces should not affect the A phase order parameter, but still suppress the B phase order parameter. A curious feature in the calculated values for T_{AB} is highlighted in the inset. At $D/\xi_0 \sim 10$ the A-B interface curves inwards, and if we lower the temperature down from T_c we transition from the A to B phase, only to transition from B to A phase again at lower temperatures. This is a really unusual behavior and it points to an instability at the A-B interface.

4.2.1 Stripe phase

The instability at the A-B boundary prompted Vorontsov and Sauls to revisit the problem a few years later. They predict that near the A-B transition line, the translational symmetry of the superfluid state will be broken [48]. The calculations were done in the weak coupling limit ($P = 0$ bar) and for a slab with one diffusive and one specular surfaces. Fixing $\xi_0 = 77$ nm (the value for the zero-temperature coherence length at zero bar), we can change the film thickness D to explore the phase diagram. As before, for thick films the B phase is stable at low temperatures. However, as the film thickness is decreased to a value D_{c_1}, which is larger than the value D_c calculated in Ref. [2] for the A-B

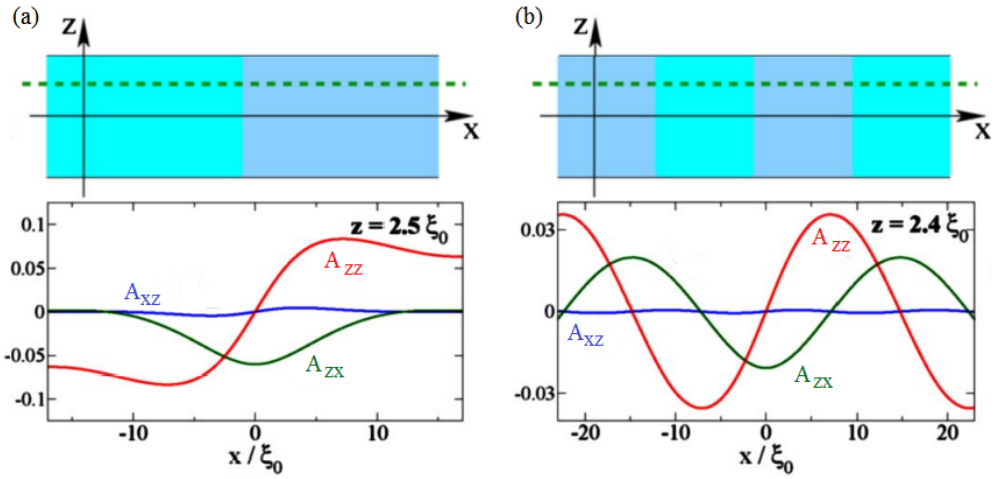

Figure 4.5: Components of the matrix order parameter (in units of $2\pi T_c$) in the *Stripe phase*.
(a) Thickness of the slab D is such that $D_c > D > D_{c_1}$. Values are shown for a slice $2.5\xi_0$ over the surface.
(b) Thickness of the slab D is such that $D_{c_2} > D > D_c$. Values are shown for a slice $2.4\xi_0$ over the surface.
Calculation done in the weak coupling limit (0 bar). Temperature is 0.5 T/T_c. Source: Ref. [48].

phase boundary, the B phase transforms into a state that consists of multiple degenerate domains of B phase. We refer to this state as *Stripe phase*. This state, in analogy with the FFLO state seen in exotic superconductors [49] breaks translational symmetry. Domain walls are expected to intercede the sample separating regions that differ through the sign of $\Delta_\perp^B$ in Eq. 4.2. A visual representation of the components of the matrix order parameter A_{ij} in the region between D_{c_1} and D_c is shown in Fig. 4.5a. The typical size of the domains is $\sim 1 - 10$ μm, and they are separated by a domain wall to which a non-B-like state is bound to. Domain walls have energy cost associated with them; this is the reason you don't have multi-domain samples in bulk. In thin slabs, having a non-zero order parameter component directed at the surface also costs energy; the presence of domain walls reduces that cost for a spatial distance of a few coherence lengths

around the wall. A simple explanation for why the *Stripe phase* could be stable in the thin slab geometry is that for thin enough samples, this reduction of the energy cost is greater than the energy cost due to the existence of the domain wall.

Moving on to thinner slabs, the domain sizes get smaller as we approach the thickness D_c and for samples with thicknesses D, such that $D_c < D < D_{c_2}$, we don't have well defined domains anymore, but rather a sinusoidal variation of the order parameter with a period of $\sim 30\xi_0$ (see Fig. 4.5b).

A refinement on the previously calculated phase diagram for the slab is shown in Fig. 4.6. In the plot the region of stability for the *Stripe phase* at the onset of the A-B transition is indicated. The calculation was done in the weak coupling limit and assumed that at least one of the surfaces of the slab is specular. Recently, Josh Wiman together with James Sauls has redone the calculations by accounting for strong coupling corrections and allowing both bounding surfaces to be diffuse scatterers. [50]. Above 5 bar pressure, strong coupling corrections destroy the *Stripe phase*. Maximum pairbreaking, highly diffusive surfaces would destroy the *Stripe phase*, but the *Stripe phase* survives some moderate degree of diffusivity of the surfaces, though the width of the region of stability of the *Stripe phase* will be somewhat reduced [51]. In order to test if this model is correct we need to look at a slab that has an A-B transition at low pressures and has sufficiently smooth surfaces. Surfaces can be made more specular by preplating with ^{4}He [52].

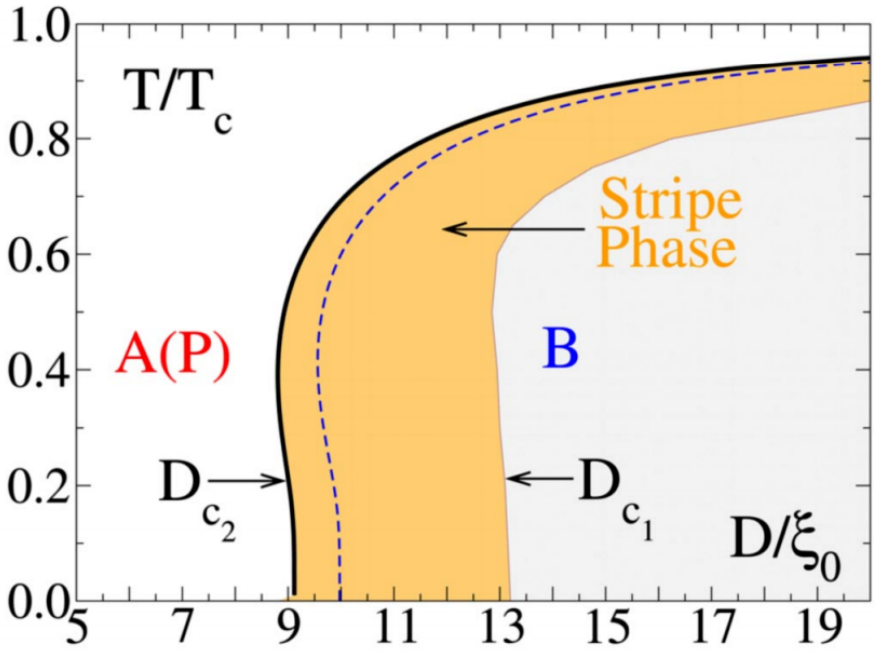

Figure 4.6: Refined prediction for the phase diagram for thin slabs of superfluid ^{3}He. Calculation is done in the weak coupling limit (0 bar), and assumes at least one of the surfaces is specular. Source: Ref. [48]

4.3 Surface states. Majorana fermions.

A superfluid gap is suppressed near a surface through the emergence of energy states within the superfluid gap. These states occur due to the changing of the sign of the order parameter normal to the surface upon reflection of quasiparticles. In the literature, these states are often referred to as Andreev bound-states. The emergence of mid-gap energy states is similar to the case of ^{3}He in aerogel we discussed in section 3.3. The difference between the two cases comes in when we consider the exact profile for the density of states. Exact calculation for the density of states at the superfluid gap when the fluid is near both a specular and a diffuse surface was done first by Nagato, et. al. in Ref. [46] and then by Vorontsov and Sauls in Ref. [2].

The case for ^{3}He near a specular wall is particularly interesting: the energy of the Andreev bound-states can be shown to be of the form[53, 54]:

$$E_{ABS} = \pm \frac{\Delta}{k_F} k_{\|} \tag{4.4}$$

Here the positive sign is for spin up quasiparticles and the minus sign is for spin down quasiparticles. In three dimensions the energy spectrum for the states bridging the superfluid gap will look like a cone with its vertex at the Fermi surface. It can be shown that in the context of the second quantization formalism, the creation operator for a quasiparticle with momentum component equal to $k_{\|}$ is equavilent to annihilation operator for a quasiparticle with a momentum component of $-k_{\|}$ and opposite spin [53]. At the vertex of the cone, there is only one state – it has the Fermi energy, and value for the parallel component of the momentum being zero. In that case the creation and annihilation operators for that state become equal to each other. This will be an example of a fermionic state that is its own anti-particle – a state referred to as *Majorana Fermion*.

The existence of Majorana states that bridge the superfluid gap was shown to be a direct consequence of the topology of the system by Salomaa and Volovik in Ref. [55]. ^{3}He near a surface is an example of a topological state of matter, and is part of a larger class of systems that exhibit similar physics, such as topological insulators and topological superconductors [56].

The thin slab geometry described in this work could potentially open the door to study the surface effects of the superfluid near a controlled surface and within a controlled geometry. In particular, the surface states will have a definite signature in the thermal conductivity across the slab, and in the measured superfluid fraction [57]. In bulk B phase, the majority of the fluid is in the superfluid state below $0.5T_c$, and for $0 < T < 0.5T_c$, the normal fraction decreases ex-

ponentially [8], whereas in the slab due to the contribution of the surface states, the normal fraction is predicted to decrease as T^3. Measuring the superfluid fraction at very low temperatures in such confined geometries can provide a direct test for the existence of the Majorana states near the surface.

CHAPTER 5

EXPERIMENTAL SETUP AND FABRICATION OF THE CELLS

In the three experiments described in this work, the fluid is confined within the head of a torsion pendulum. The pendulum is mounted on top of a $PrNi_5$ / Copper hybrid nuclear demagnetization stage, which is situated within a 7 Tesla superconducting magnet. The stage can be precooled to a base temperature of $\sim$ 7mK by a custom modified SHE dilution cryostat. To cool to sub-mK temperatures, one needs to disconnect the demagnetization stage from the cryostat via a superconducting heat switch and then ramp down the field.

5.1 Torsion pendulum setup

Torsion pendulum experiments have been instrumental in studying the superfluid fraction of helium. The normal state of ^{3}He fluid has large viscosity near the superfluid transition ($\sim$ 1 Poise). Viscous penetration depth, δ, which is the lengthscale over which the velocity of the fluid can change is given as:

$$\delta = \sqrt{\frac{2\eta}{\omega\rho}} \tag{5.1}$$

with η and ρ being the viscosity and the density of the fluid, and ω the angular frequency the fluid oscillates. For acoustic frequencies ($\sim 500-2000$ Hz), typical for torsion pendulum experiments, δ is of the order $\sim 100 - 500$ μm, a distance much larger than the distance between the strands of the aerogel or the size of the cavity defining the thin slabs. In all of these cases, the normal fluid should be well-clamped. On the other hand, the superfluid fraction will be decoupled from the pendulum due to its zero viscosity. As we go below the superfluid transition temperature, the total moment of inertia of the pendulum will de-

crease, and thus the pendulum's period will decrease. If the fluid is confined within a rotationally symmetric container, then the superfluid fraction can be determined by measuring the period of the torsion pendulum period shift ΔP through the following expression:

$$\frac{\rho_s}{\rho} = \frac{\Delta p(T)}{\Delta p_{max}} \tag{5.2}$$

In this expression, $\Delta p(T) = p_0(T) - p(T)$, where p_0 is the period of the pendulum when all of the fluid is fully coupled, and p is the measured period. Δp_{max} is defined as the difference between p_0 and the period of the empty cell p_{empty}. Since the viscosity of the fluid is largest at T_c, typically $\Delta p_max = p(T_c) - p_{empty}(T_c)$. One, however, needs to account for the empty cell period dependence on temperature, when $\Delta p(T)$ is calculated.

Schematics and photographs of the torsion pendulums used for the three experiments described in this thesis are shown in Fig. 5.1, Fig. 5.2, and Fig. 5.3. The pendulums are made of three main components: the torsion rod which also serves as a fill line, the experimental cell in which the fluid is contained, and two magnesium alloy wings mounted on the body of the torsion rod. The mirror-like polished magnesium wings are used to capacitively drive the pendulum into resonant motion, and to capacitively detect the motion. The wings are attached to the body using Stycast 1266 epoxy impregnated cigarette paper. That way they are electrically isolated from the body of the pendulum. Bias wires are attached to the wings using silver paint. A set of two matching electrodes is positioned very close to the wings of the pendulum. Bias voltage of $50 - 100$ V was established between the electrodes and the pendulum wings, provided by a battery pack on the top of the cryostat.

Technical drawings showing the exact dimensions for the torsion rods are

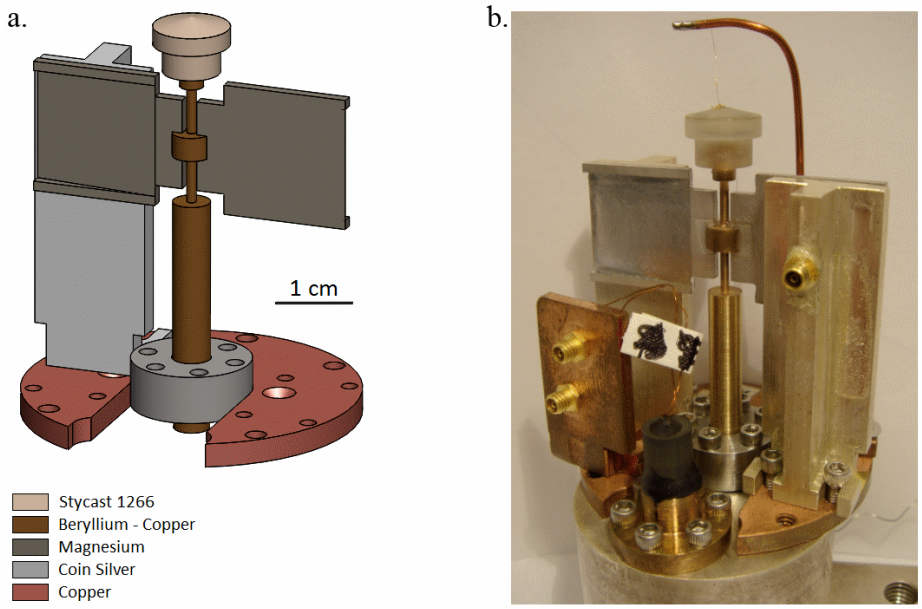

Figure 5.1: (a) 3D-rendering of the squeezed aerogel pendulum setup. (b) Photograph of the squeezed aerogel pendulum.

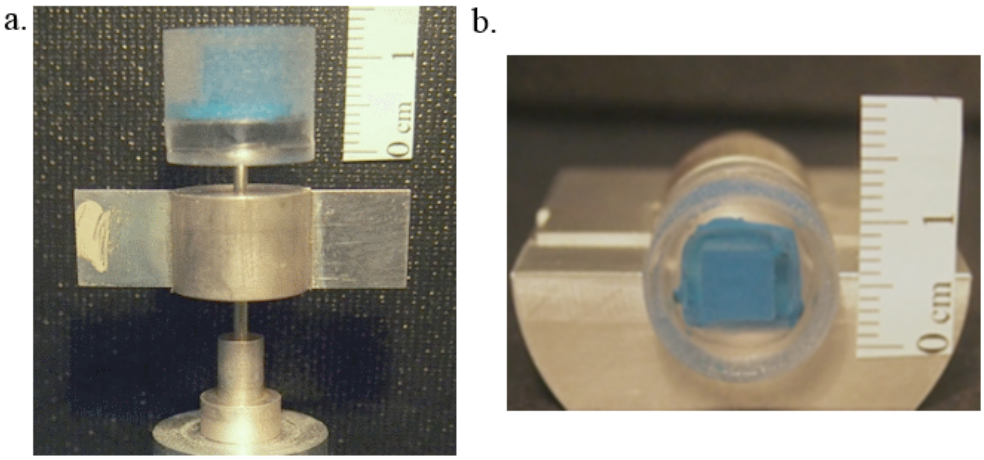

Figure 5.2: Photographs of the torsion pendulum used to study superfluid ^{3}He embedded in nematic aerogel. Photographs were taken with the pendulum at the lab bench, and show it from the side (a) and looking down its head (b). The blue cube visible in (b) is where the nematic aerogel sample is located.

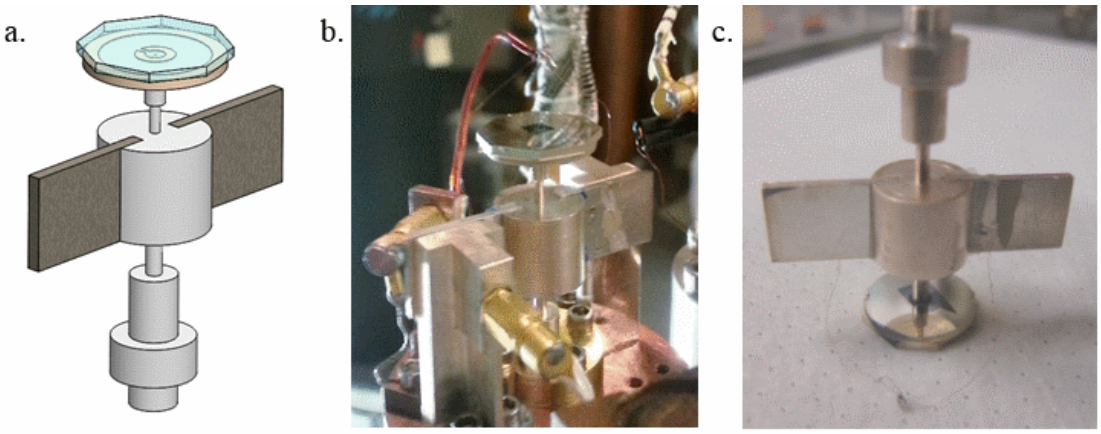

Figure 5.3: (a) 3D-rendering of the pendulum used to study confined superfluid ^{3}He within a 1.08 μm slab.
(b) Photograph of the pendulum setup as it is mounted on the cryostat. (c) Photograph of the pendulum, resting on its head on the lab bench.

shown in Fig. 5.4, Fig. 5.5, and Fig. 5.6. The torsion rod for the squeezed aerogel experiment was made from beryllium-copper alloy, but due to its strong temperature dependence of the elastic properties of beryllium-copper at low temperatures, the subsequent torsion rods for the nematcally ordered aerogel and the thin slab cell were made from coin silver (90% silver, 10% copper). All the torsion rods were thermally annealed after machining to relieve any built-in stresses and reduce the number of defects. A torsion pendulum made with a well-annealed torsion rod will have significantly higher quality factor, Q, and thus will give us higher frequency resolution.

5.1.1 Annealing recipe for coin silver

The annealing recipe for the coin silver torsion rods was the following:

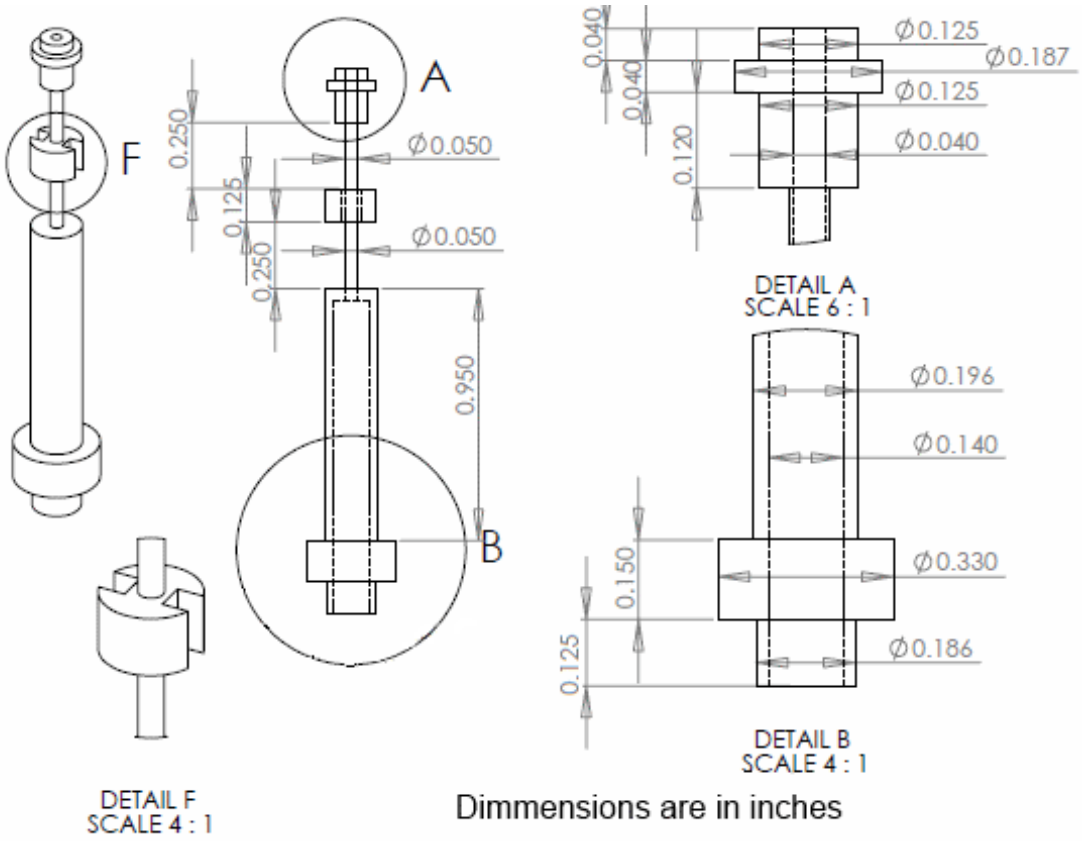

Figure 5.4: Drawing showing the dimensions of the torsion rod used in the experiment in which we study superfluid ^{3}He embedded in squeezed silica aerogel. The torsion rod is made from beryllium-copper alloy

Load the torsion rods in a vacuum tube furnace, and pump to $\sim 10^{-6}$ Torr. Then ramp up the temperature from room temperature to $600\,^\circ\mathrm{C}$ at a rate of $20\,^\circ\mathrm{C/min}$. Once that set point is reached, ramp the temperature up to $700\,^\circ\mathrm{C}$ at $5\,^\circ\mathrm{C/min}$. Finally, set the temperature to $727\,^\circ\mathrm{C}$, with a ramp rate of $1\,^\circ\mathrm{C/min}$. Hold the torsion rod at $727\,^\circ\mathrm{C}$ for two hours, before turning off the furnace and let it come back to room temperature overnight.

At these temperatures coin silver gets really soft and if it is not supported correctly it will sag due to its own weight. One needs to carefully position the

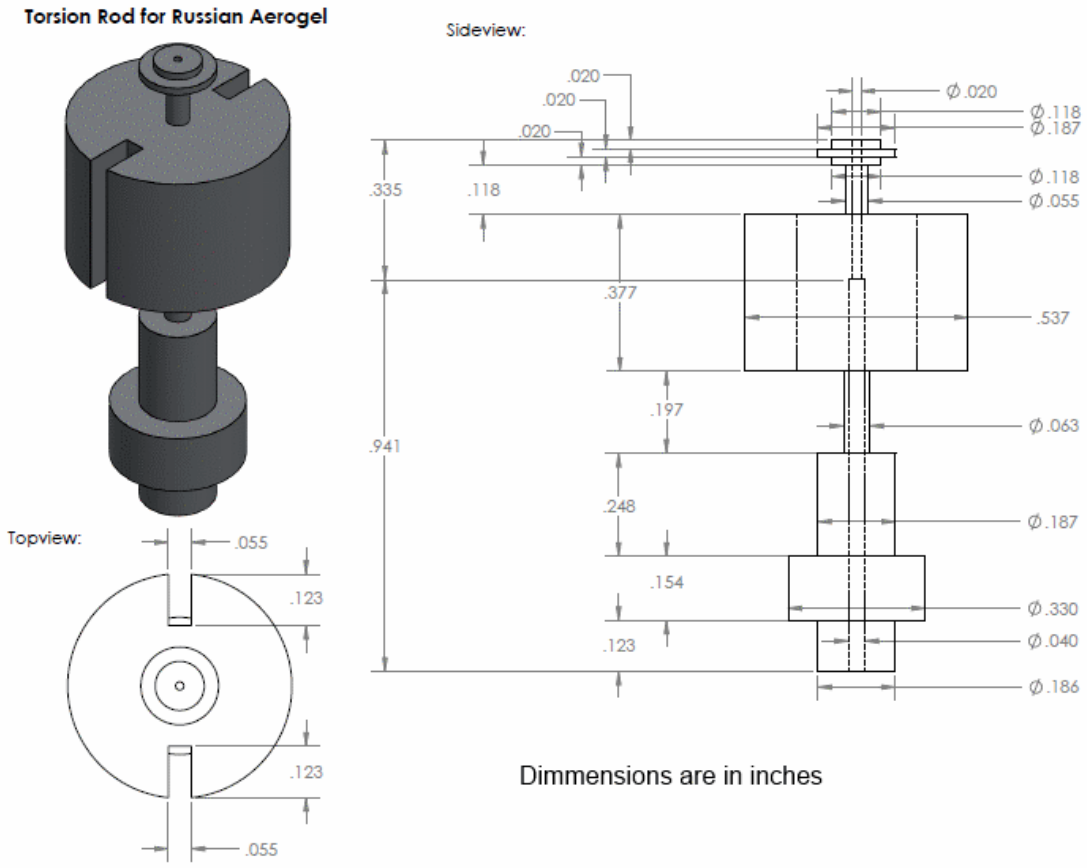

Figure 5.5: Drawing showing the dimensions of the torsion rod used in the experiment in which we study superfluid ^{3}He embedded in nematically ordered aerogel. The torsion rod is made from coin silver.

torsion rod withing a specially machined macor support so that its weight does not exert any torque on the structure.

Properly annealed torsion rod should allow the torsion pendulum to have a quality factor of $\sim 10^6$ at milli-Kelvin temperatures, which translates to a frequency resolution in our experiments in the range of $1 : 10^8 - 10^9$.

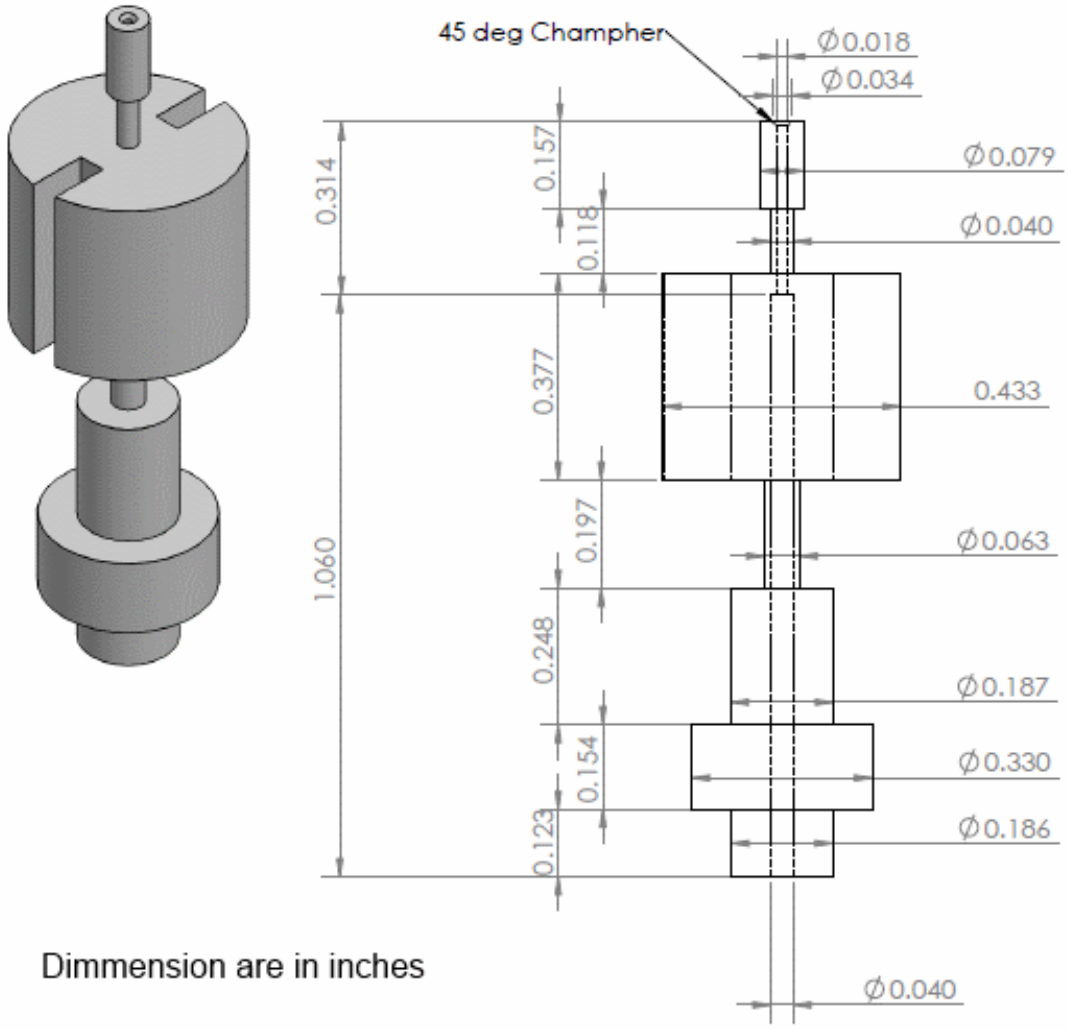

Figure 5.6: Drawing showing the dimensions of the torsion rod used in the experiment in which we study superfluid ^{3}He confined within a 1.08 μm cavity. The torsion rod is made from coin silver.

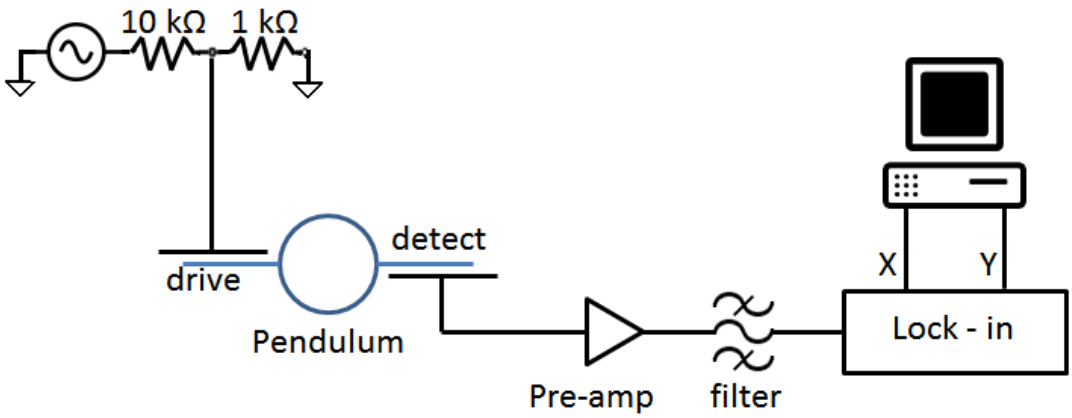

Figure 5.7: A schematic for the setup through which the pendulum is excited and through which its resonant motion detected.

5.2 Data acquisition setup

The output of a function generator was divided further by a resistive voltage divider to achieve amplitude of < 1 mV. The drive signal was fed into the drive electrode, which is biased with respected to the wings of the pendulum. The motion of the torsion pendulum would cause change in the capacitance between the detect electrode and the other wing of the pendulum. This generates a small ac-voltage which is fed into a pre-amplifier outside of the cryostat. To reduce noise in the signal we feed the output from the pre-amplifier to a narrow band-pass filter. The signal is then fed into the input of a dual-phase lock-in amplifier. The lock-in splits the signal into a component in-phase and out-of-phase with the drive. These two values are averaged over a period of a minute. The experimental setup is controlled by LabView virtual instruments, which also record and process the data. A simple schematic of the experimental setup is shown in Fig. 5.7.

We aim to measure the resonant frequency of the pendulum and its quality factor Q versus temperature. To do that we use the following scheme. We sweep the driving frequency across the resonance for a fixed temperature, T_0, to obtain a resonance curve. By fitting to that curve, we can find the quality factor at this temperature, $Q(T_0)$. We can also plot the values of the out-of-phase component of the signal (Y) versus the values of the in-phase component (X). Such a plot (Nyquist plots) forms a circle with a diameter equal to the signal amplitude at resonance, A, centered at $(A/2, 0)$. The high quality factor of the pendulum means that the time constant with which transients die out is long, and it takes hours to obtain a good frequency sweep. It is clear that doing frequency sweeps and finding the resonant frequency, f_{res}, and quality factor, Q, for each of them is impractical. Instead, we obtain the values for f_{res} and Q by inferring them from the values of Y and X while driving the pendulum at a frequency near the resonant frequency. Using geometrical arguments, and knowing the relationship between the phase of the response versus the drive frequency near resonance, we can derive the following relationships:

$$f_{res} = f_{drive}\left[1 + \frac{Y(T)}{2QX}\right] \tag{5.3}$$

$$Q = \frac{V_{drive}(T_0)}{V_{drive}}\frac{Q(T_0)}{A(T_0)}\frac{X^2 + Y^2}{2X} \tag{5.4}$$

where $Q(T_0)$, $A(T_0)$ were determined from the sweep at the fixed temperature T_0. Since it is possible that the resonant properties of the pendulum are dependent on its amplitude (due to nonlinear terms in restoring force), we adjust the drive amplitude to keep the signal amplitude within a predetermined range. We also adjust the drive frequency periodically so that it is close to the resonant frequency at all times.

5.3 Resonant modes of the pendulums

The pendulums have two torsion rods with a wide body holding the wings between them. The extra torsion rod acts as a further mechanical isolator that filters the vibrations coming from the base of the pendulum towards the head. Because of the torsion rods, there are two torsion resonant modes for the pendulums.

The first resonant mode is the symmetric mode in which the wings and the head move in phase and the node in the angular velocity is at the bottom torsion rod. The frequency of that mode is determined by the restoring force coming from the lower torsion rod and the net moment of inertia of both the body plus the wings and the head, i. e. roughly the moment of inertia of the whole pendulum.

The second resonant mode is the antisymmetric mode in which the wings and the head move out of phase. The node in the angular velocity is at the upper torsion rod. The frequency of the antisymmetric mode is determined by the restored force from the upper torsion rod and the moment of inertia of the head. As long as the moment of inertia of the body plus wings is much larger than the moment of inertia of the head, it contributes little to the resonant frequency of the antisymmetric mode.

To determine the effect of any changes of the moment of inertia of the fluid within the head one needs to divide that change by the moment of inertia of the head in the antisymmetric mode and by the moment of inertia of the whole pendulum in the symmetric mode. Change of the resonant frequency of the antisymmetric mode is significantly more sensitive to the shifts in the inertia of the

fluid compared to the symmetric mode, because the inertia of the head is lower and also the noise of the antisymmetric mode is lower than the corresponding values for the symmetric mode.

In addition to the torsion modes of the pendulum, it can also have a number of "floppy" modes, in which there is a sideways bending motion within the torsion modes. These modes are not useful for the study of the superfluid, because even when the viscosity of the superfluid decreases to zero, the superfluid is still clamped to the torsion pendulum head by the walls of the cell.

During the design of the pendulum, we aim to characterize the resonant modes. We can do that by modeling a 3d-sketch of the pendulum in SolidWorks, and run a dynamic simulation that finds the first few resonant modes. We take note which two modes are the torsion modes and make sure they are far in frequency from the other "floppy" modes.

5.4 Thermometry

Primary thermometer was provided through a ^{3}He melting curve thermometer (MCT) cell. The cell has a solid ^{3}He plug coexisting with molten liquid. The melting pressure of ^{3}He depends strongly on temperature in the range from 1 K to 0.905 mK. Measuring the pressure in the MCT cell using a capacitive pressure gauge we can find the temperature with accuracy up to less than 0.001 mK. At 0.905 mK, the crystal lattice ordering in the solid changes, and the melting pressure dependence on temperature becomes a lot smaller, hence the temperature noise increases. The melting curve thermometer is useful down to $\sim 0.3 - 0.4$ mK.

The main problem with the melting curve thermometer is that it is not in direct contact with the helium in the experimental cell, but rather measures the temperature of the nuclear demagnetization stage. The stage is thermally coupled to the fluid via silver sinter heat exchangers, which have thermal boundary resistance to the helium varying as T^{-3}. At low temperatures the thermal time constant between the MCT and the fluid can be significant.

To remedy that, a quartz tuning fork immersed in the ^{3}He fluid, which allows for a more immediate reading of the temperature of the ^{3}He within the pendulum. The fork is either continuously swept through resonance or run through a digital phase-locked-loop the same as the torsion pendulum. Due to the rapid change of density and viscosity of the fluid below the superfluid transition, the fork's resonant frequency and quality factor can be related to the temperature of the fluid. Thus, the quartz tuning fork can be used as a secondary thermometer, especially useful in the superfluid state.

5.5 Making the aerogel cells

5.5.1 Compressed aerogel

A 98% open silica aerogel was grown directly into a pillbox shaped stainless steel cavity consisting of a tightly fitted lid, a base and a shim inserted between them. The aerogel was then compressed by 10% along its main axis by removing the shim and pressing the lid onto the base, bringing the height of the cell to 400 μm. The height was chosen to be small enough to couple the aerogel well to the walls (though aerogel displacement relative to the walls of the cell still needs

to be considered), but large enough to ensure fine resolution in determining the fraction of superfluid. The moment of inertia of the torsion head and aerogel filled cell is calculated to be 0.064 g-cm^2 and that of the helium at saturated vapor pressure – 5.85×10^{-5} g-cm^2, or about 1 part in 10^3 of the inertia of the head.

The steel cavity was dry fitted into an already hardened epoxy cast in order to reduce possible contamination of the aerogel by any epoxy penetrating through holes in the stainless pillbox. Despite careful machining of the epoxy cast, there appeared to be empty regions around the periphery of the cell occupied by ^{3}He not embedded in the aerogel (bulk fluid). In addition, we need to consider the bulk fluid within the fill line inside the upper torsion rod in our subsequent analysis.

A schematic of the torsion pendulum head is shown at Fig. 5.8. The locations of the inferred bulk fluid regions are also indicated.

5.5.2 Nematic aerogel

The aerogel sample was carefully cut using thin razor blades into the shape of a cube with sides of about 5 mm and coated with epoxy. Two L-shaped pieces of hardened Stycast 1266 epoxy were coated with Tra-bond 2151 epoxy (blue in color) and brought into contact with the aerogel cube. Tra-bond 2151 epoxy has very high viscosity and forms high contact angle with the aerogel surface, which prevented the epoxy from being drawn into the aerogel voids by capillary action. After hardening of the epoxy, the remaining aerogel surface was coated with another layer of Tra-bond 2151. The rest of the torsion pendulum head was

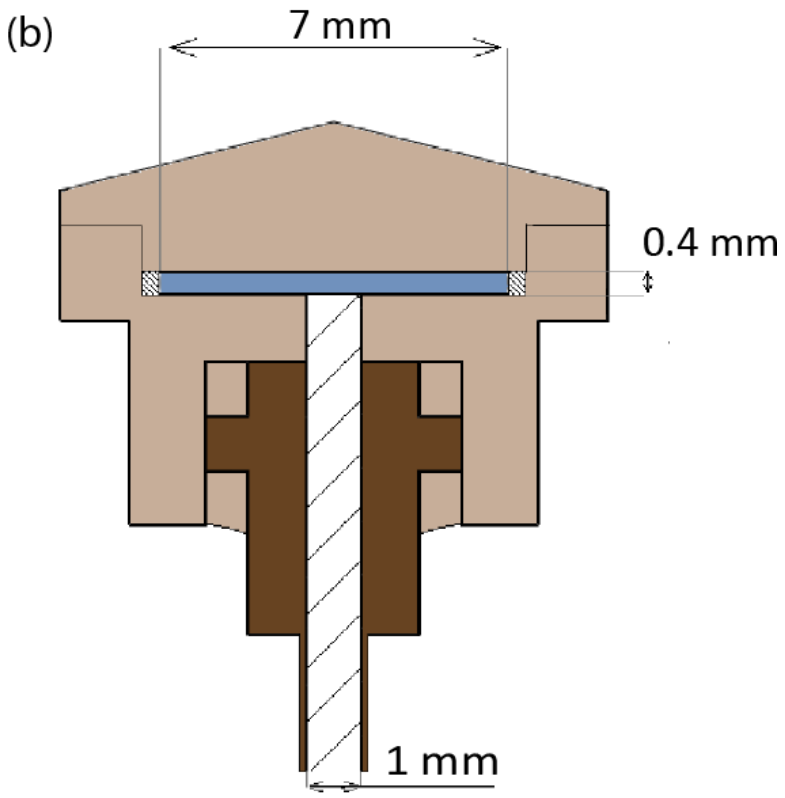

Figure 5.8: A schematic for the head of the torsion pendulum which contains the uniaxially compressed silica aerogel sample (shown in blue). The rest of the pendulum head is made from hardened Stycast 1266 epoxy, and the torsion rod made from beryllium-copper alloy.

made from Stycast 1266 hardened epoxy shell. The coated aerogel was inserted into the shell, and newly mixed Stycast was poured in to fill all the voids and complete the pendulum head.

5.6 Making the nanofabricated cavity cell

To make the cell in which we confine the fluid, we bond a pre-cut piece of glass to a patterned piece of silicon in which the cavity is defined and etched. An image of the completed cell is shown in Fig. 5.9.

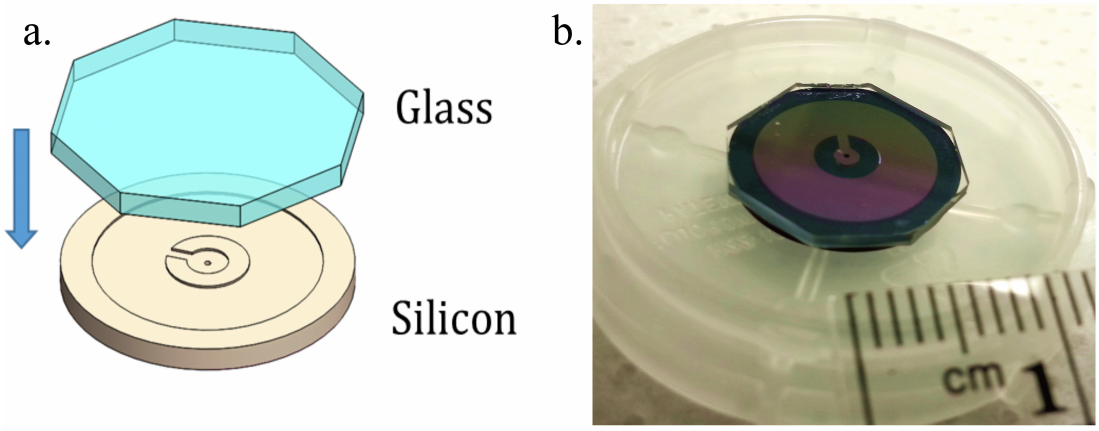

Figure 5.9: (a) The torsion pendulum head in which the fluid is confined within is made by bonding a patterned disk-shaped piece of silicon and an octagonal piece of smooth glass
(b) The completed cell. The cavity in which the fluid is contained can be seen easily due to light interference.

5.6.1 Outline of the process flow

We used the tools at the Cornell Nanoscale Science and Technology Facility (CNF) to make the experimental cell.

An important consideration in the beginning of the process is choosing the right wafers from which to make the cells. For the silicon part of the cell we used a double sided polished silicon wafer ([100] crystal orientation). We want the cell to be able to withstand significant pressure without excessively bowing and deforming its shape, so we needed to use the thickest wafers feasible. In a previous round of fabrication, 3 mm thick wafers were used, but these proved to be really hard to work with. Instead, 1 mm thick wafers were used for the assembly (to the point of anodic bonding) of the cell described in this work. This allowed us to use the tools at CNF without limitations and complete the entire cell inside the CNF clean room.

The fabrication process can be broken into five major steps. First, create the step in the silicon surface for the cavity. Second, etch through the fill line hole and the backside concentric circles to ease the epoxy keying in. Third, polish and cut the glass. Fourth clean and prepare the surfaces, and then bond the silicon and the glass to complete the cell. Final step is to deposit a thick film of silver which is expected to help with thermalizing the silicon and glass at ultra-low temperatures. A detailed sketch of the process flow is shown if Fig. 5.10. Each step is described in more details in the following subsections.

5.6.2 Cavity design

In each four inch wafer we fitted sixteen cells in a four by four pattern. Each cavity has a diameter of 11 mm. At the middle of the cavity sits the fill line which is a 335 μm through hole. To reduce bowing and prevent collapse of the cavity during bonding, we have designed a C-shaped region around the middle of the cell at which the silicon is bonded to the glass just like it is outside of the cavity. The outer diameter of the C-shaped region is 4 mm and the inner diameter is 1.5 mm. Thus, the cavity from which the superfluid signal comes from (main experimental cavity) has an annulus shape of inner diameter of 4 mm and outer diameter of 11 mm. The central region where the fill line is located is connected to the main experimental cavity through a channel of 1.25 mm length and 0.6 mm width.

To ensure structural integrity and leak-tightness of the cell, the diameter of the silicon disk that makes the cell needs to be somewhat larger than the outer diameter of the annulus comprising the cavity, so that there is enough area of

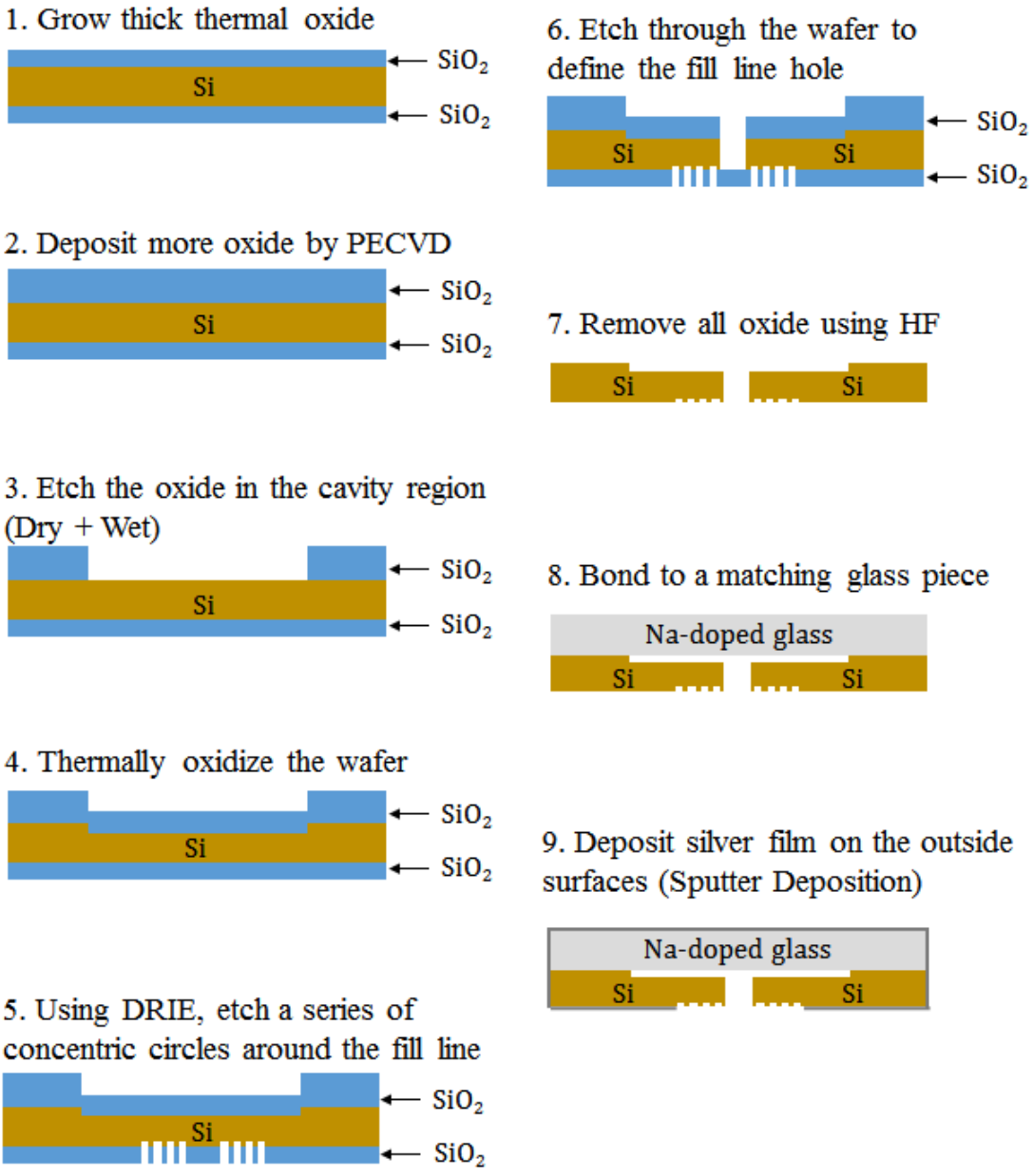

Figure 5.10: Detailed step by step description of the steps required to fabricated the 1.08 μm cavity cell.

silicon and glass bonded around the cavity. We chose the diameter of the silicon disk to be 14 mm.

In order to separate the silicon disks from the four inch wafer, we etched through two arcs around each cell. This way the silicon disks were connected to the main wafer only through two small bridges. In order to separate the disks from the main wafer we made a scribe mark using a diamond scriber at those bridges and push on the disk to break the bridges.

Figure 5.11 shows the pattern of the four by four cells on each wafer. The green color shows the places where the 1.08 μm recess for the cavity is. Purple shows the two etched through arcs around each silicon disk, which define the circular shape of each silicon piece. Not shown in this zoomed out figure are the fill line holes at the center of each cavity.

Figure 5.12 shows the area near the fill line at each cell in more detail. The fill line hole is shown in blue. A series of concentric circles that are on the backside of the silicon wafer surface are shown in dark yellow. These concentric circles are each 20 μm thick and are spaced 20 μm apart. This pattern is on the outside surface of the cell and is etched ~ 20 μm deep. It is intended to provide a larger surface area in which the epoxy connecting the coin silver torsion rod and the cell can key in.

5.6.3 Step creation for the cavities

We made the step in the silicon surface which produces the experimental cavity upon bonding by using a modified local oxidation process. The goal is to

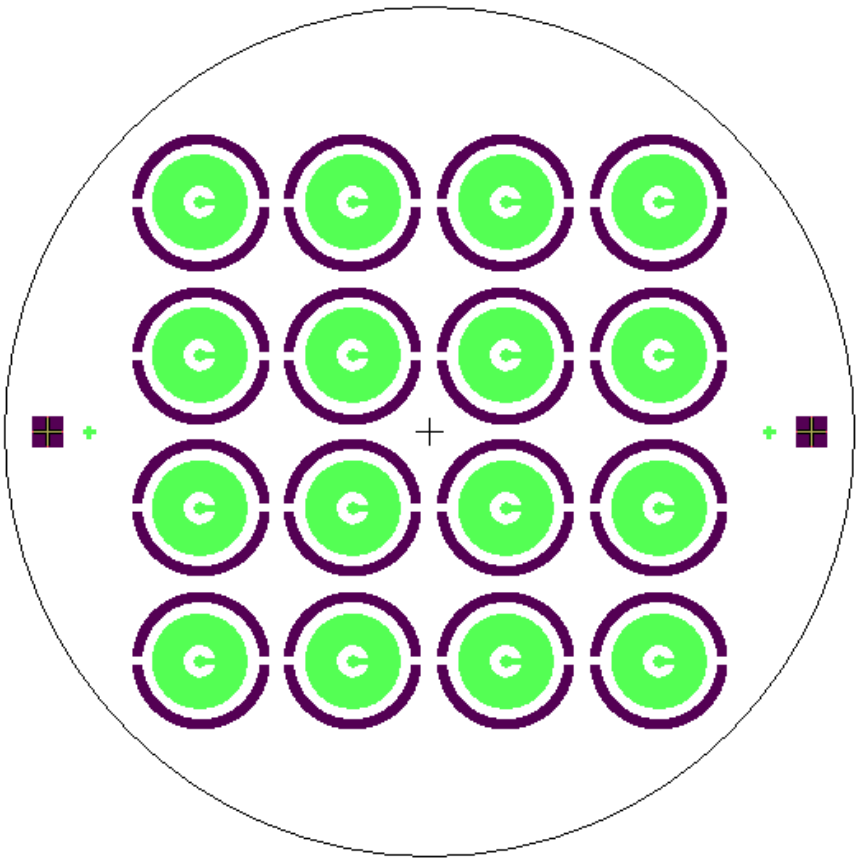

Figure 5.11: An overview of the pattern on each silicon wafer. Green layer is the layer of the cavities, purple is etched through the wafer. Not shown at this scale the through hole for the fill line and the backside concentric circles.

oxidize the silicon surface in the cavity area deeper than the region outside the cavity. That way by removing all oxide, we are left with a recess in the silicon surface. We could have etched the silicon surface using Reactive Ion Etching, however, this would have produced a much rougher surface at the bottom of the cavity and also would have resulted in significant variations of the cavity depth across the wafer and also across a single cell. Cavity depth uniformity and surface smoothness are extremely important for the proposed experiment.

The first step of the process involved covering the surface of the wafer with

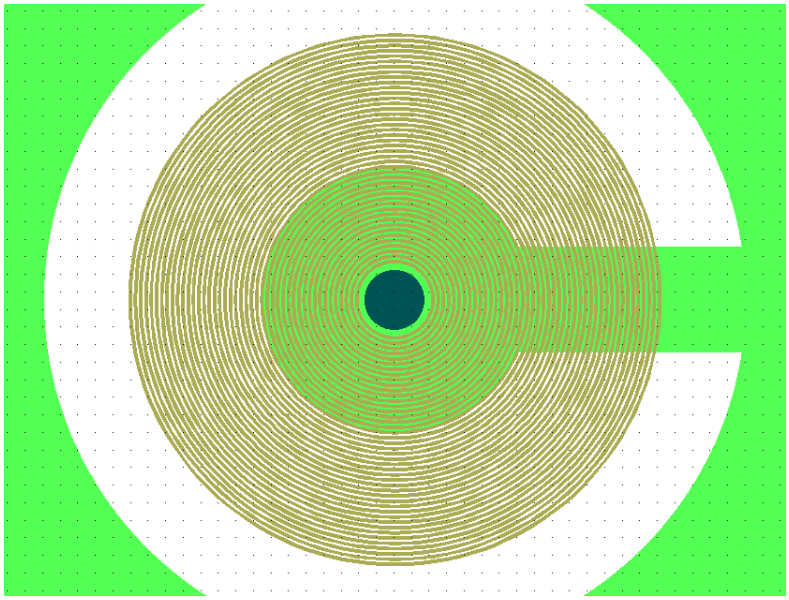

Figure 5.12: A closer view of the center of each cavity. Shown are the fill line (blue) and the backside concentric circles pattern (dark yellow).

a thick oxide. The thicker the oxide, the easier would be to create a deeper cavity in the second oxidation step. About 2.5 - 3 μm of oxide was grown on the wafer surfaces by oxidizing them for 12 hours at $1200\,^{\circ}\mathrm{C}$ in an atmospheric furnace. Hydrogen and oxygen (no HCl) were flowed into the furnace tube, providing the necessary conditions for wet oxidation. As the film thickness increases, the rate of the thermal oxide growth slows down significantly. Thus to get even thicker films, we want to deposit extra oxide rather than try to grow more. Plasma Enhanced Chemical Vapor Deposition (PECVD) process was used to grow additional 2 μm of oxide on the front wafer surface. PECVD deposition is fairly fast, but the film quality is significantly lower compared to thermally grown film. However, since we use this film as a mask layer, this is not as important and using PECVD oxide is acceptable.

After having this really thick oxide layer on the wafer surface, next step was

to spin, bake and develop positive photoresist (SPR 220-3.5). The cavity pattern was exposed using UV light, and the regions of the resist exposed to it were dissolved away in the developer solution. Since we were using a very thick photoresist, proximity plate bake was used ($1200\,^\circ\mathrm{C}$ for 120 s). The wafer was not quenched on a cold surface but rather left to cool by itself in the wafer box. Exposure time was 25 s.

After the lithography step, the wafers were placed in a Reactive Ion Etch plasma chamber, where a CHF_3 + O_2 recipe was used to dry etch the majority of the exposed oxide in the cavity regions. Since we wanted to keep the cavity surfaces as smooth as possible, the oxide was not etched fully. Instead, the last 150-200 nm of oxide was etched using Buffered Oxide Etch (BOE 1:6). BOE does not attack the silicon, so it removes all the oxide in the cavity region while leaving the silicon surface pristine and smooth.

After removing all the resist and carefully cleaning the wafers, we place the wafers back into the oxidation furnace for a second oxidation step. The rate of oxide growth is given by the Deal-Grove model [58]. For very thin oxide films the film thickness grows linearly with time, while for thick films, the film thickness grows with the square root of the time. The silicon surface outside the cavity region is covered by a very thick layer of oxide. The rate of growth of oxide in this region will be much slower than at the cavity region where the silicon surface is exposed.

An important point of consideration is that the silicon swells upon oxidation. it takes 2 nm of silicon consumed to produce 4.5 nm of SiO_2. Thus, to create a step of x nm, we need to create a difference in the oxide growth inside and outside the cavity of of $2.25x$.

5.6.4 Etching the fill line and patterning the backside

We want to have a fill line hole that has straight walls and has a well defined small diameter. Previous attempts to drill the hole using diamond drills or grind it away using diamond slurry [59] proved possible but extremely difficult. Fear of contamination and scratching the surfaces was another reason why we preferred to make the hole using the tools inside the CNF clean room. We used a Deep Reactive Ion Etch (DRIE) tool to etch through the silicon. It is important to note, that we would not have been able to use this tool if the wafers were thicker, e.g. 3 mm thick as they were in the first attempts of making these cells.

To make the whole pattern, we spin thick resist (SPR 220-7) and expose and develop. To harden the resist further so it can survive the subsequent plasma etching, we leave the wafers in a $90\,^{\circ}\mathrm{C}$ convection oven overnight. There is oxide on both sides of the silicon wafer, we need to etch away the oxide in the hole area from the cavity side, and keep the oxide on the other side to serve as a stop for the plasma once the hole is completed. The oxide in the areas of the holes is etched using reactive ion etching. The remaining resist and the oxide outside of the hole area provides a mask through which the wafer can be etched through (the DRIE process has a high selectivity for silicon versus resist, and even higher versus oxide).

The concentric circles pattern on the backside of the wafer is also etched using DRIE but only to $20\,\mu$m depth. An optical microscope image of the backside of the completed fill line hole is shown in 5.13.

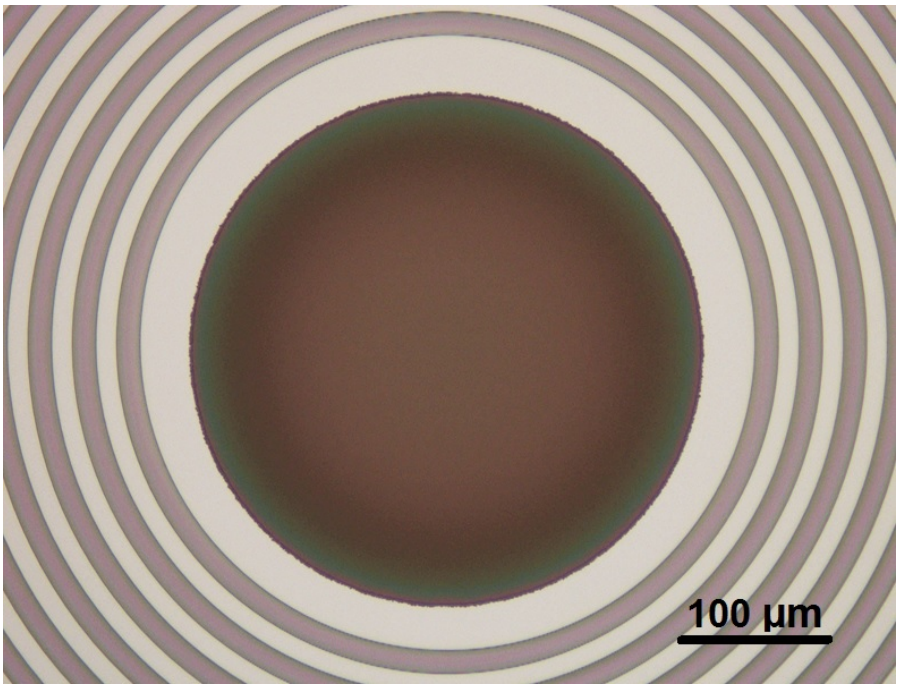

Figure 5.13: Optical microscope image of the fill line hole. Shown is the backside silicon surface where the epoxy seal is to be made.

5.6.5 Polishing and cutting the glass

As mentioned in section 4.2.1, in order to observe the stripe phase we need smooth cell surfaces. Rough and diffusive surfaces tend to suppress the stability of the stripe phase. In fact, original calculations were done for two perfectly specular surfaces (e.g. free surfaces), and how adding real rough surfaces changes the result is not investigated systematically. Also, defects on the surfaces could pin the phase boundaries and broaden the transitions. This is why we want to fabricate a cell with walls as smooth as possible.

We use Atomic Force Microscopy (AFM) to quantify the smoothness of the surfaces. The silicon surface of the cavity maintains its atomic smoothness since its never directly etched, instead it is consumed in a diffusion driven oxidation process. A typical AFM image that shows the smoothness of the silicon surface

is shown in Fig. 5.14a.

The glass we use to bond to the patterned silicon (Hoya SD-2) had a much rougher surface as shipped to us. We further polished the front surface of the glass wafers using Chemical Mechanical Planarization (CMP) process. A standard polishing cloth was used. The polishing slurry contained colloidal silica particles suspended in KOH solution. AFM image of the glass surface after polishing is shown in Fig. 5.14b.

After polishing, the next step was to dice the glass in the octagonal shape needed for our cell. We spun a thick layer of resist which is subsequently hard baked overnight in a convection oven to harden the resist further for it to be effective as a protective layer during the dicing process. The wafer was put on a sticky dicing tape and was diced in the diamond coated dicing saw tool in the CNF clean room. The wafer was first diced into squares, then the squares were put in the tool one by one and had their four corners cut off to produce an octagon.

5.6.6 Cleaning and anodic bonding

At this stage we were ready to bond the silicon and glass to finish the cell. We soaked the silicon in hydrofluoric acid (HF) to remove the oxide on the wafer chip surface. This step should have underetched any contamination on the silicon surface. However, we could not do the same with the glass pieces, since HF is extremely corrosive to glass. Instead a long basic RCA clean recipe was used to clean the glass surface. While this step was not necessary for the silicon, we put the silicon pieces in the solution as well in order to clean any possible

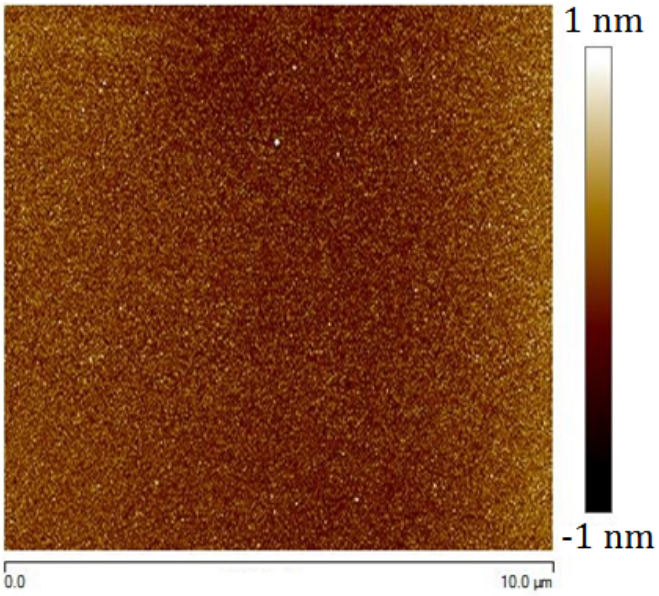

Typical AFM height profile of the Si surface

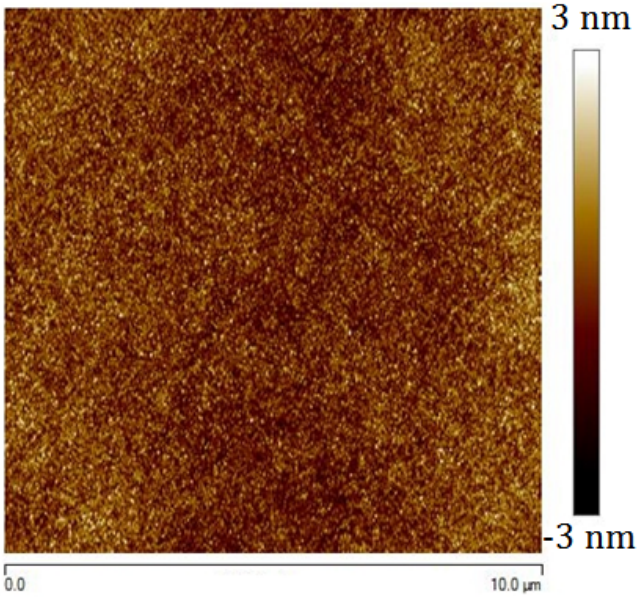

Typical AFM height profile of the Polished Glass Surface

Figure 5.14: AFM images of the cell surfaces. (a) shows the silicon surface imaged right before bonding. (b) shows the glass surface imaged right before bonding.

contamination they might have picked up after the HF bath. The RCA clean recipe was the following: 1 part NH_4OH, 1 part H_2O_2, and 5 parts of deionized water heated to $75 - 80\,^\circ\mathrm{C}$. The solution was stirred very vigorously using a magnetic stirrer while the pieces were immersed, hoping that the flow would dislodge further any particles on the surface. The pieces were immersed in the solution for about half an hour. We note that similar cleaning steps were taken multiple times throughout the process, before each lithography step and before the oxidation steps.

Once the pieces are cleaned and their surfaces imaged using AFM, we were ready to put their surfaces in contact. The bonding process was completed using a custom made bonding jig shown in Fig. 5.15. A macor spacer with a carefully machined hole which matches the dimensions of the cell was placed on top of the bottom electrode. The silicon piece was first dropped in the hole, and then the glass piece was dropped on top of it. The macor spacer ensured that the silicon and glass did not move laterally during the bonding process. After the glass was inserted and placed in contact with the silicon the top electrode was placed on top of the glass. A steel ring separated by another macor spacer was placed on top of the electrode. The steel ring was connected to the bottom electrode through twelve screws which are carefully tightened (extremely gently, otherwise the glass or the silicon can break) to apply pressure on the glass silicon stack.

The bonding jig was placed in an air furnace and heated to $425\,^\circ\mathrm{C}$. The two electrodes were connected to a high voltage power supply while the jig was still in the furnace. Applying voltage of 200 V for about 5 minutes was sufficient to create a reliable bond between the silicon and the glass. The glass we use

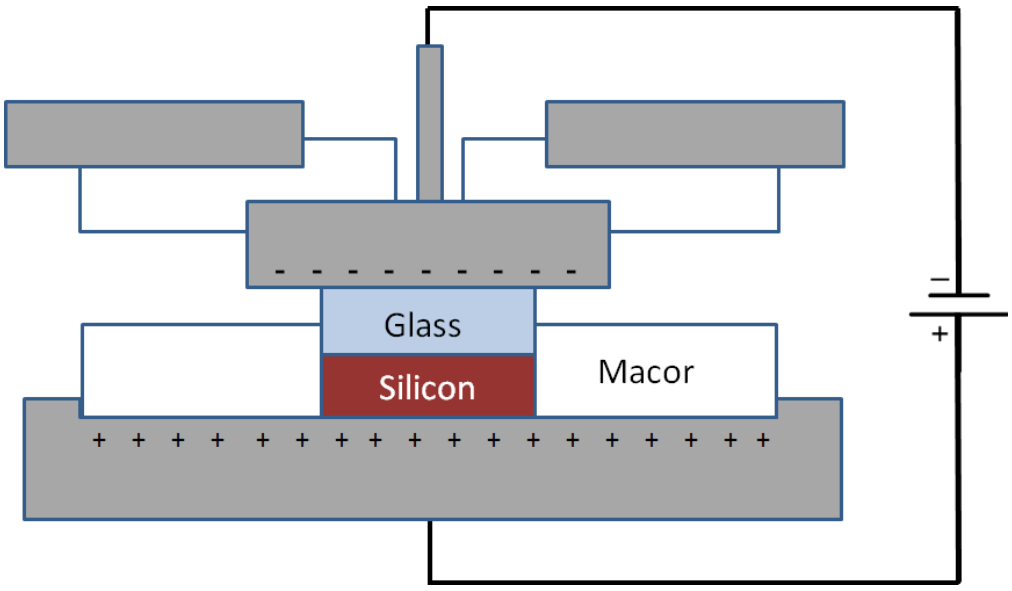

Figure 5.15: Schematic of the custom made bonding jig. Grey represents stainless steel and white – macor. The jig is placed in an air furnace during the bonding process.

is sodium doped; when voltage is applied at high temperatures the sodium is expelled from the glass-silicon interface. This results in dangling bonds for the glass which are then connected to the silicon atoms on the silicon surface. The bond achieved this way is so strong that pressurizing the cell to failure ($>$ 30 bar pressure) results in the glass breaking, rather than the glass-silicon bond separating.

The temperature of the bonding process was chosen so that the total thermal expansion between room temperature and the bonding temperature is the same for both the glass and the silicon. This was so that no bowing or distortion occurs to the cell as it cools down. A small degree of bowing might occur, however, when cell is cooled from room temperature to cryogenic temperatures.

5.6.7 Metal deposition

The final step in the fabrication was to deposit a thick layer of silver on the outside surfaces of the cell. The fill line hole was plugged with a piece of kapton tape. A small piece of kapton tape was put on the glass side of the cell opposite of the fill line hole to shield a window in which we can see through the cavity end of the fill line. This is to check that epoxy has not run into the cell when attaching the cell to the torsion rod.

A teflon holder that clamps the cell by its edge was machined. The holder was screwed onto a rotation plate inside a sputter deposition chamber. This way the cell can be silvered on all sides. In order for the deposited silver film to stick well to the silicon and the glass, a thin titanium adhesion layer was deposited first. Since titanium becomes superconducting at low temperatures and hence its thermal conductivity decreases significantly, we want to deposit as thin of adhesion layer as possible – $\sim 5 - 10$ nm thickness. The silver film deposited had a thickness of approximately 1 μm.

5.6.8 Fill line epoxy seal

Connecting the silicon surface of the cell to the silver torsion rod proved to be non-trivial. There were three unsuccessful attempts to do this experiment, all thwarted by the epoxy joint leaking when the experiment was cooled to cryogenic temperatures. A leak from the pendulum would break the vacuum inside the vacuum can of the cryostat and provide a thermal link between the pendulum and the 4.2 Kelvin walls of the can.

The stress on the epoxy comes from the large difference in the thermal expansion coefficients of the silver, epoxy and silicon. Conventional epoxies have thermal expansion coefficient that is about twice as large as that of silver. We would like to find a strong and impact resisting epoxy that has a much lower thermal expansion coefficient. Out of the multiple different epoxies tried, it was determined that Tra-bond 2151 was the best candidate for the job. This filled epoxy had the lowest thermal expansion coefficient from all tested (lower than that of silver), and it proved to be extremely strong. It also had large enough viscosity so it would not run into the fill line hole and contaminate the cavity.

The other key component in making a successful leak tight joint is turning shear stress into compressive stress. Most materials have a significantly higher yield strength under compression than under shear. Below we describe the procedure to make the epoxy joint.

First, we take a hollow glass tube (inner diameter 100 μm, outer diameter 310 μm). We cleave the tube so that its length is approximately 4 mm. Then we coat the outer surface of one of its ends with a thin layer of epoxy. We have made an elaborate setup for aligning and inserting the glass tube in the cell. The cell is position on top of x, y, z translation stage platform, which is positioned at the base of a small drill press. The glass tube is held by a teflon sleeve which is inserted into the drill chuck. The teflon is squeezed just enough so that the glass tube is held securely, but it can move up or down provided small amount of force is applied. A stereo microscope is focused on the cell hole and is used to align the glass tube with respect to the fill line hole. When the alignment is deemed good, the glass tube end coated with epoxy is lowered into the hole. After the epoxy is cured the chuck is carefully loosened and lifted up. The end

of the torsion rod is now inserted into the chuck. Fresh epoxy is put around the area of the glass tube - silicon surface joint. Then the torsion rod is carefully lowered onto the silicon squeezing out the freshly applied epoxy. Some of the epoxy fills the space between the silver and the glass tube, while the rest comes out on the perimeter of the joint. The excess epoxy is wiped out and the joint is left to cure. Fig. 5.16 provides a schematic for the geometry of the joint, and illustrates the two step process involved.

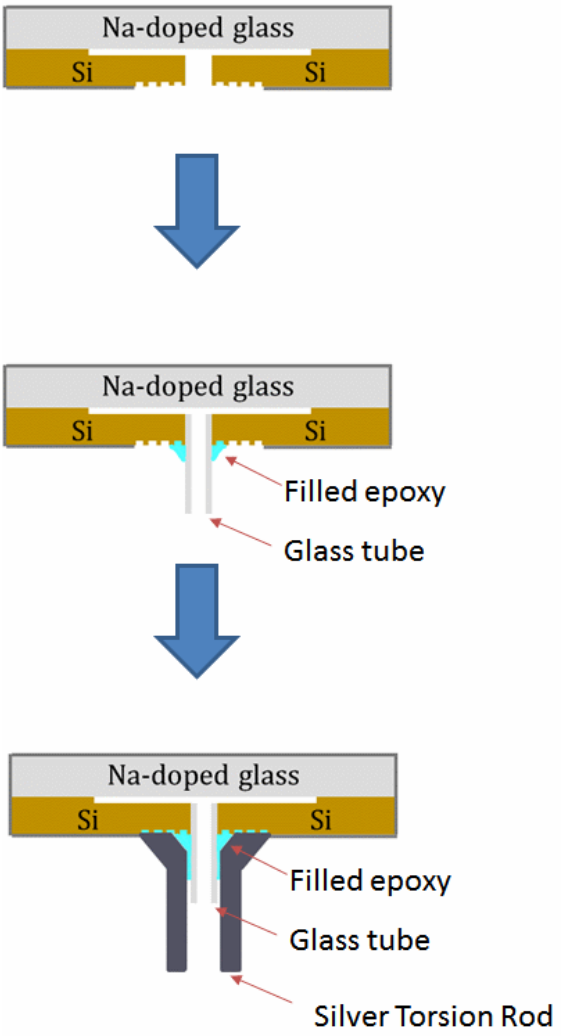

Figure 5.16: A schematic illustrating the 2 step procedure for making the epoxy seal. First epoxy joint is between a glass tube and the cell. Second epoxy joint is between the silver and glass tube and silicon.

CHAPTER 6

SIGNATURES OF THE SUPERFLUID STATES OF ^{3}HE CONFINED TO 10% UNIAXIALLY COMPRESSED AEROGEL

We carefully mapped the torsion pendulum period and dissipation for a large number of pressures, both in the normal state (temperatures from 100 mK to about 1-2 mK) and in the superfluid state.

6.1 Empty cell data

Before we can make inferences for the superfluid fraction measured from the frequency shift, we need to carefully characterize the resonant properties of the empty pendulum. The empty cell data is necessary in finding the fraction of the moment of inertia of the fluid that is decoupled from the cell according to Eq. 5.2.

The empty oscillator's resonant frequency and Q were first measured between 100 mK and 1.5 mK. In Fig. 6.1 we plot the measured empty cell background (Q^{-1} and oscillator period). The background Q ranged from $\approx 8\times10^4$ at 100 mK to $\approx 5.7\times10^5$ at low temperatures. The period shift showed a minimum around 30 mK. We also plot the measured Q^{-1} and period for the oscillator after it was filled with ^{3}He at 0.14 bar.

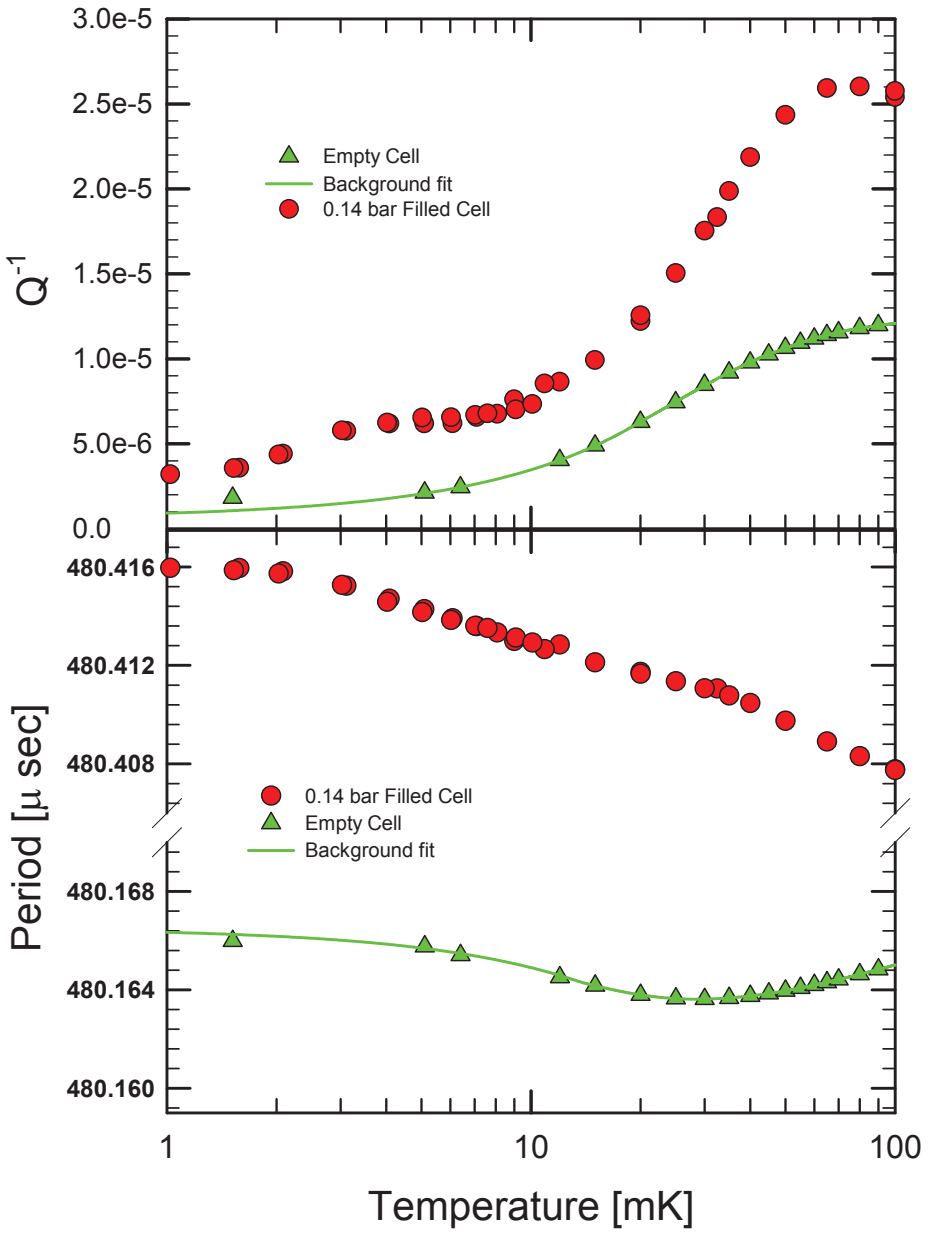

Figure 6.1: (Top Panel): The measured Q^{-1} vs temperature (solid triangles) for the empty oscillator, together with fit (solid line). We also plot data obtained for the cell filled with ^{3}He at 0.14 ± 0.03 bar (solid circles). The fit for the empty cell data is subtracted from the filled cell data to obtain the signal from the ^{3}He. (Bottom Panel): We plot the period of the empty cell (solid triangles) together with the fit through the empty cell data (solid line). The data for the cell filled with 0.14 ± 0.03 bar of ^{3}He is shown as solid circles. Note the offset in the period.

6.2 Bulk fluid contribution

In order to perform a careful analysis on the data in the superfluid state, we need to account for any contribution due to bulk fluid outside of the aerogel sample.

We expect the normal state helium liquid to be well locked to the strands of the aerogel. Thus, in the normal state any change in the resonant frequency compared to that of a cell with a fully locked fluid should originate from the bulk-like fluid regions of the cell. Figure 6.2 shows data representing the fraction of the moment of inertia not coupled to the walls of the cell at the four experimental pressures 0.14, 2.6, 15.2, and 25.7 bar. The decoupled fluid fraction and dissipation show temperature dependent behavior characteristic of two distinct bulk fluid regions (two peaks in the normal state dissipation data, two "shoulders" in the normal state decoupled fraction data).

The effective length and diameter of the fill line in the torsion rod and the cast epoxy cell are 6 mm and 1 mm. The bulk fluid column amounts to 0.8% of the inertia of the fluid in the cell and is designated as bulk fluid Region 1. In order to calculate the contribution to dissipation and period shift coming from the fluid in the fill line, we start by calculating the angular velocity profile $\Omega(r)$ by using the Navier-Stokes equation in a tall cylindrical geometry, which leads to

$$\frac{\partial^2\Omega}{\partial r^2} + \frac{3}{r}\frac{\partial\Omega}{\partial r} + \frac{i\omega\rho}{\eta}\Omega = 0 \tag{6.1}$$

with $\Omega(\text{radius of the cylinder}) = \Omega_{cell}$.

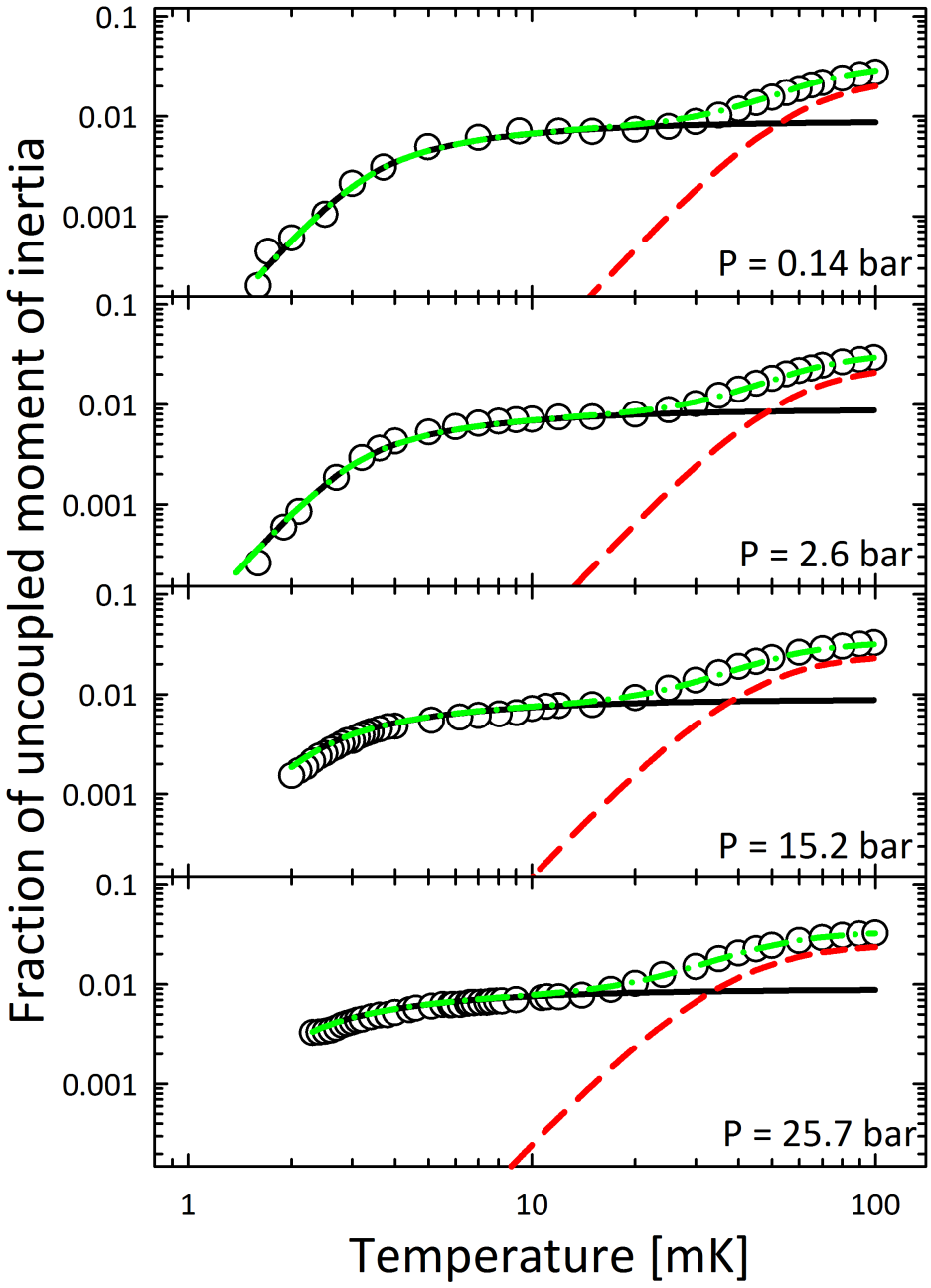

Figure 6.2: The fraction of fluid decoupled from the pendulum vs temperature for four pressures after background subtraction (open circles). Also shown are the fits for the bulk fluid contribution for two components - Region 1, fluid in the fill line, a 1 mm diameter, 6 mm long cylinder comprising 0.8% of the total fluid moment of inertia (solid (black) line), and Region 2, fluid at the periphery of the cell, modeled as a cavity of height 28 μm (dashed (red) line) comprising 3.2% of the moment of inertia. The dash-dotted (green) line shows the sum of the contributions from the two bulk fluid components.

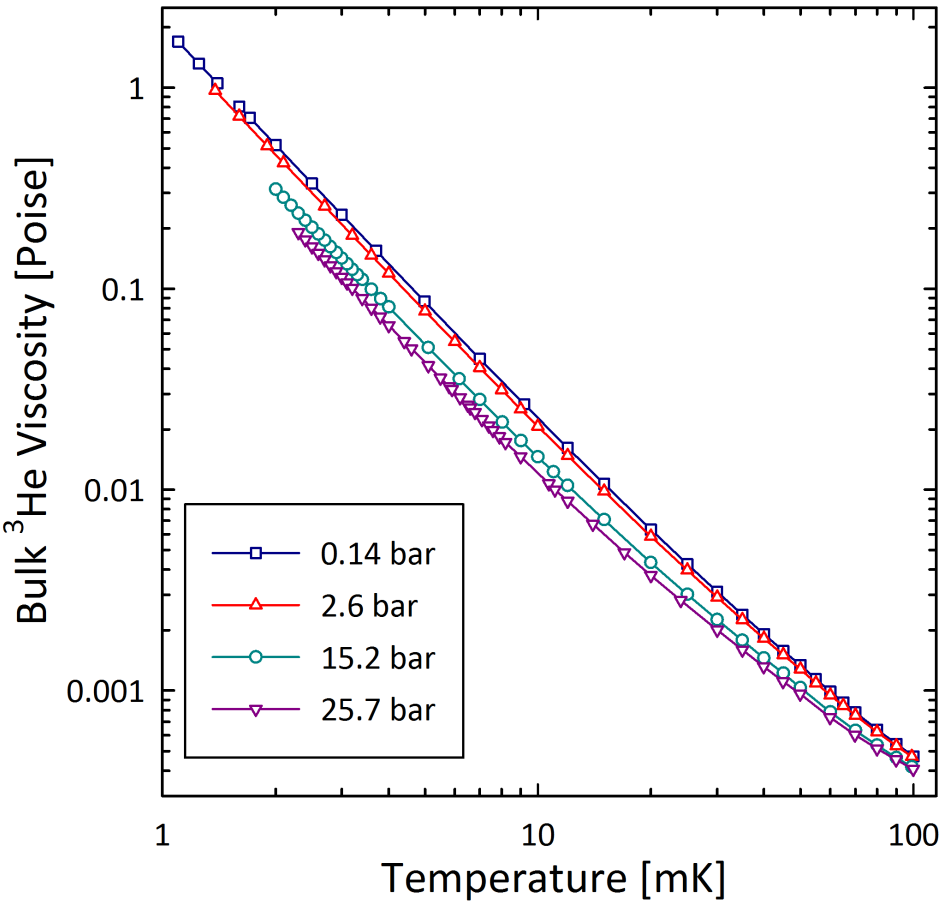

Figure 6.3: Values of viscosity in the normal state at the four experimental pressures for which we have data in the normal state.

Solving for Ω we find the torque exerted by the fluid:

$$N = 2\pi R^3 h\eta \left(\frac{\partial \Omega}{\partial r}\right)_{r=R} = \beta_1 + i\omega\beta_2 \tag{6.2}$$

where β_1 contributes to the damping of the pendulum and β_2 to the moment of inertia. Temperature dependence of these values is determined by the temperature dependence of the viscosity of the fluid, $\eta(T)$.

Near T_c we expect the normal state bulk viscosity to scale as T^{-2}. Above $T > 10$mK the viscosity deviates from the Fermi liquid T^{-2} behavior and we use the following relations between the thermal conductivity (κ), heat capacity

(C_V) and the viscosity (η) to calculate higher temperature values for η:

$$\kappa = \frac{1}{3} C_V v_F^2 \tau_\kappa \tag{6.3}$$

$$\eta = \frac{1}{5} \frac{m^*}{m} \rho v_F^2 \tau_\eta \tag{6.4}$$

$$C_V = m^* \frac{\pi^2 k_B}{\hbar^2} (\frac{V}{3\pi^2 N})^{2/3} RT \tag{6.5}$$

Assuming that density and molar volume do not change in the temperature range 1-100 mK, and assuming $\tau_\eta \propto \tau_\kappa$, we can infer that $\eta \propto \kappa$. To find the exact values for the viscosity in the normal state, we use the values for $\eta(T_c)$ given in Ref. [60] and Ref. [61], and $\kappa(T_c)$ in Ref. [62] and divide the two values to find the proportionality factor. We then multiply $\kappa(T)$ from Ref. [62] by this factor for each of the pressures we are interested and we find $\eta(T)$ up to 100 mK. The values for the viscosity for the four experimental pressures we used to calculate bulk fluid contribution in the normal state are shown in Fig. 6.3 In the superfluid state, experimental values for the superfluid fraction are taken from Ref. [63] and for the viscosity from Ref. [64]

Numerically solving Eq. 6.1, we can calculate the contribution from the bulk fluid in the fill line. This contribution is shown with a solid (black) line in Fig. 6.2. It is evident in Fig. 6.2 that there is bulk fluid within the cell we have not yet accounted for.

The steel cavity containing the aerogel was dry fitted in the epoxy cast to prevent epoxy running in. We believe this resulted in small pockets of bulk fluid existing around the periphery of the cell. While we cannot do an exact calculation for the effects of these regions the same way as we did for the fluid in the torsion rod, we can still use the uncoupled moment of inertia data (Fig. 6.2) to estimate the contribution to the pendulum's dissipation. We assume that the relationship between the real and the imaginary part of the torque arising

from the cell periphery bulk fluid is the same as that of a uniform thickness film encompassing all of the cell. For a thin film of fluid with a thickness h and inertial contribution I_{per}, the torque exerted is $N = \beta_1 + i\omega\beta_2$, with:

$$\beta_1 = \omega I_{per} \frac{\delta}{h} \frac{\sin(h/\delta) - \sinh(h/\delta)}{\cos(h/\delta) + \cosh(h/\delta)} \tag{6.6}$$

$$\beta_2 = I_{per} \frac{\delta}{h} \frac{\sin(h/\delta) + \sinh(h/\delta)}{\cos(h/\delta) + \cosh(h/\delta)} \tag{6.7}$$

where $\delta = \sqrt{2\eta/\rho\omega}$ is the viscous penetration depth of the fluid. Fitting to the unaccounted portion of the data in Fig. 6.2, we find $h = 28$ μm and $I_{per} = 0.032 I_f$, where I_f is the moment of inertia of all the helium in the torsion pendulum head. These values are consistent with our expectations. The accuracy to which the epoxy cast and stainless steel cell are machined is within one-thousand of an inch, i.e. 25 μm, and a film of that thickness around all of the cell surface amounts to $0.05 I_f$. Since the bulk fluid is more likely coming from a few separate regions around the periphery, rather than from a continuous film, we would expect that $I_{per} \lesssim 0.05 I_f$. We also use these values and the viscosity of ^{3}He to obtain the fraction of decoupled fluid from the periphery (Region 2) which we plot as the dashed (red) line in Fig. 6.2.

6.2.1 Fourth sound resonances

At the lowest experimental pressures (0.14, 2.6 and 4 bar), the liquid in the aerogel does not transition to a superfluid state in the temperature range we have performed our experiments. In this case, the resonance period shift below T_c originates entirely from the bulk fluid regions. Plotting the data and the calculated period shift coming from the bulk we see very good fit (see Fig. 6.4), apart from a series of "peaks" and "ripples" in the observed dissipation and

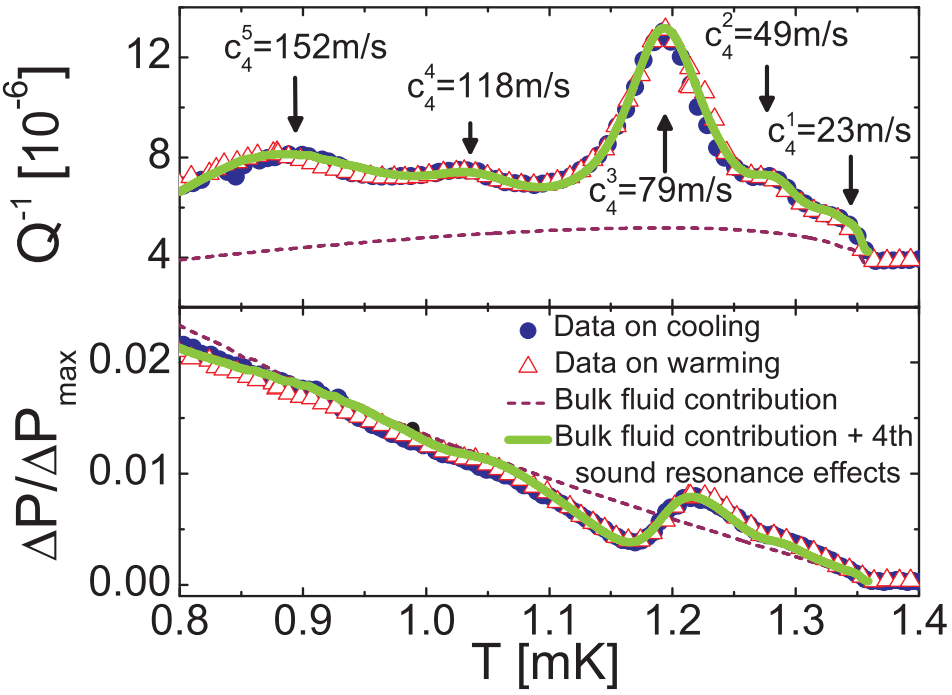

Figure 6.4: Data and fits for the Q^{-1} and ΔP at 4 bar.

period shift respectively (Fig. 6.6). We attribute these features to the effects of 4th sound modes of the bulk ^{3}He in the aerogel-free cavities.

The 4th sound velocity for ^{3}He, c_4, is the velocity for a sound mode in which only the superfluid component moves, while the normal component is clamped. The 4th sound velocity is given by $c_4 = \sqrt{\rho_s/\rho}\, c_1$, where c_1 is the ordinary longitudinal (1st) sound velocity. As the sample cools below T_c^{bulk}, c_4 increases, as does the resonant frequency of a particular mode (f_4) until it approaches f_{dr}, the driving frequency of the torsional oscillator. As the two frequencies approach one another, the 4th sound mode absorbs energy from the torsional mode, leading to an increased Q^{-1} near the mode crossing. The frequency (and period) of oscillation are also "pulled" by the mode crossing. The correction to the period shift due to 4th sound is given in terms of the width of the 4th sound resonance

Δf as:

$$\Delta \mathrm{P}_4 = P_s \frac{1 - \frac{1}{\chi}\frac{\rho_s}{\rho}}{4(1 - \frac{1}{\chi}\frac{\rho_s}{\rho})^2 + (\frac{\Delta f}{f_{dr}})^2} \tag{6.8}$$

We first identify the 4th sound resonances in Q^{-1} and estimate Δf and χ, a tortuosity parameter. Then, we adjust the scale parameter P_s to match our data for the period shift. Fig. 6.4 shows data for a pressure of 4 bar, chosen because T_c and T_{ca} are well differentiated and the individual Q^{-1} peaks are readily identified. Five 4th sound resonance modes (no attempt was made to differentiate between the two cavities or calculate the exact sound modes we are exciting) were identified at that pressure with $c_4^1 = 23$ m/s, $c_4^2 = 49$ m/s, $c_4^3 = 79$ m/s, $c_4^4 = 118$ m/s, $c_4^5 = 152$ m/s, corresponding to cavity length scales of the order of a cm, consistent with the lateral dimensions of the cell.

6.3 Superfluid Data

To identify the signatures of the different superfluid phases and the transitions between them, let us first look in more detail at the data for a particular pressure, $P = 32$ bar. It is evident from fig. 6.5 that there is large hysteresis loop between cooling and warming. This is a signature of the first order transition between A and B superfluid states. On cooling, we transition into the A phase and we stay in the A phase for quite a while as we cool down. Supercooling the A deep into the superfluid state is expected for the fluid within aerogels, as was discussed in section 3.3.1. The hysteresis loop at low temperatures closes upon the A to B transition. The temperature region over which the A to B transition occurs is shown between the dotted lines in fig. 6.5. Upon warming after a full transition into the B state, we observe the fluid persisting in the B state until

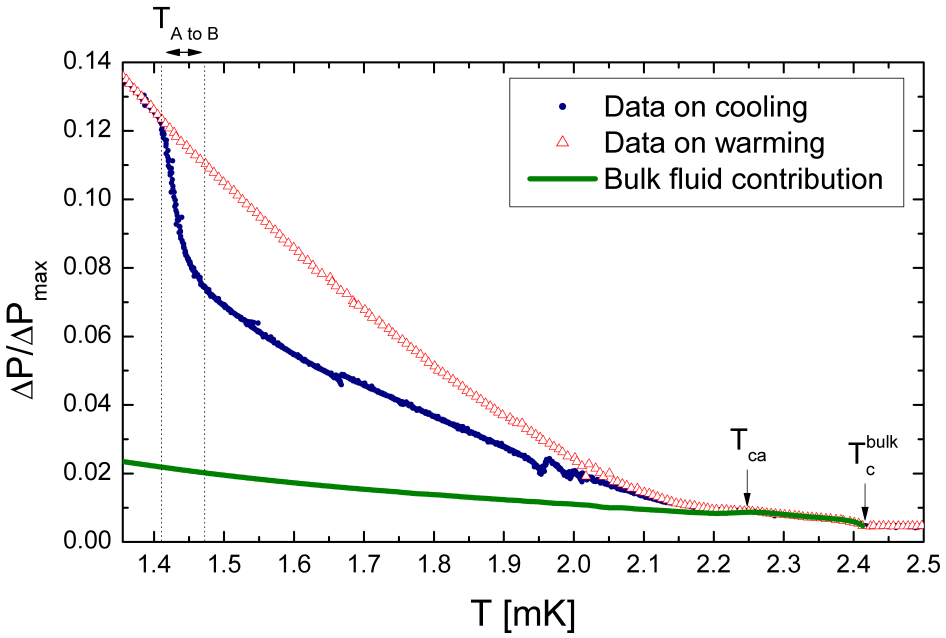

Figure 6.5: Torsion pendulum period shift vs temperature at 31.9 bar showing data taken while cooling (filled (blue) circles) and warming (open (red) triangles). The solid (green) line is a fit of the bulk superfluid period shift. Indicated is the bulk transition temperature T_c^{bulk}, the superfluid transition temperature for the fluid in the aerogel, T_{ca}, and the the range of temperatures for the A to B transition.

close to the superfluid transition for the fluid within the aerogel T_{ca}.

Shown in fig. 6.5 is also the calculated bulk fluid contribution to the period shift of the pendulum. The superfluid in aerogel transition temperature T_{ca} is determined as the temperature at which the experimental data deviates from the calculated bulk contribution. Also shown is the bulk superfluid transition temperature T_c^{bulk}, which is clearly indicated by the response of the quartz tuning fork thermometer.

Fig. 6.6 shows in its top panel a zoom in at the data from fig. 6.5 near T_c. To extract the actual superfluid fraction for the fluid within the aerogel, we subtract the bulk contribution from the period shift of the pendulum we measured. The

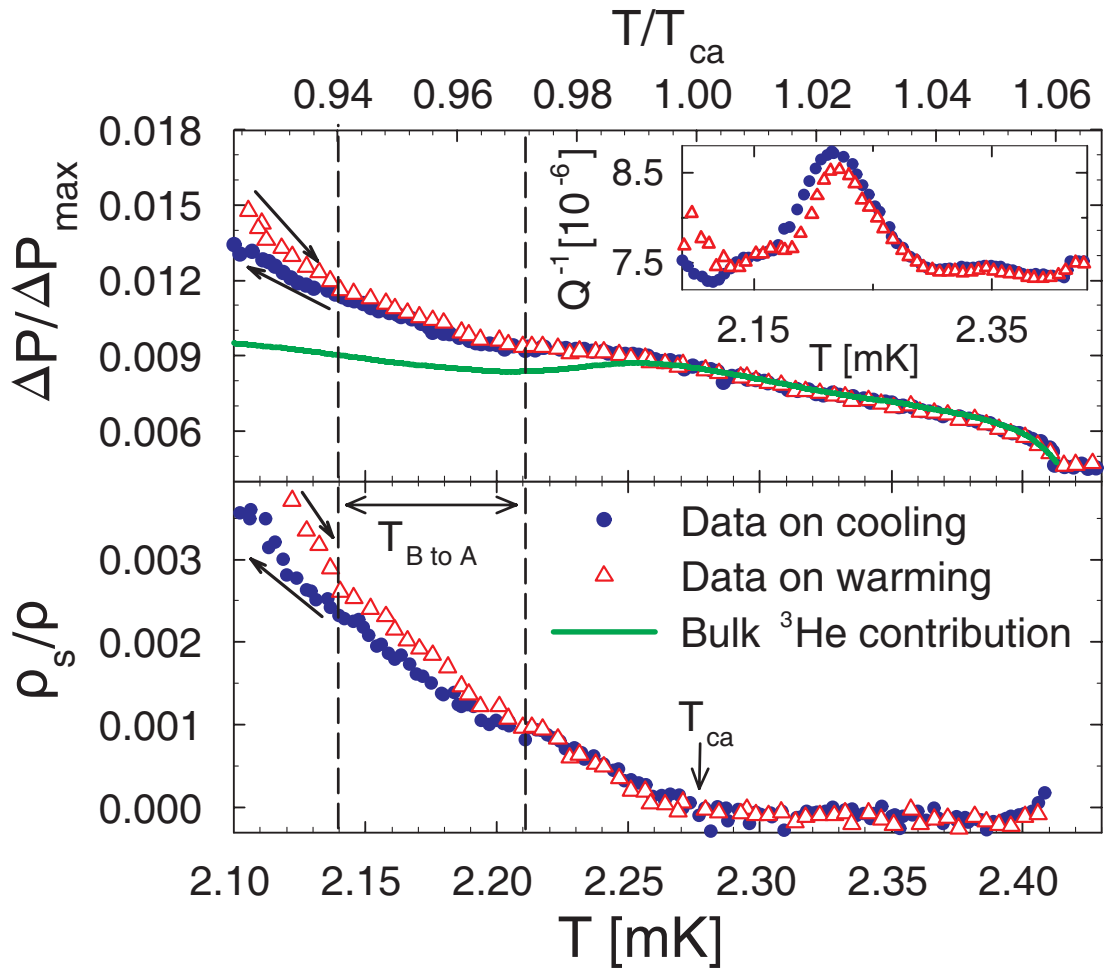

Figure 6.6: (Upper panel) Torsion pendulum period shift vs temperature near the superfluid transition at 31.9 bar. Inset shows the corresponding dissipation (Q^{-1}) and broad 4$^{\text{th}}$ sound resonance. (Lower panel) After subtraction of the bulk superfluid contribution we show the superfluid density of ^{3}He in the aerogel. The arrow designates the onset of superfluidity and dashed lines define the width of the $B \rightarrow A$ transition.

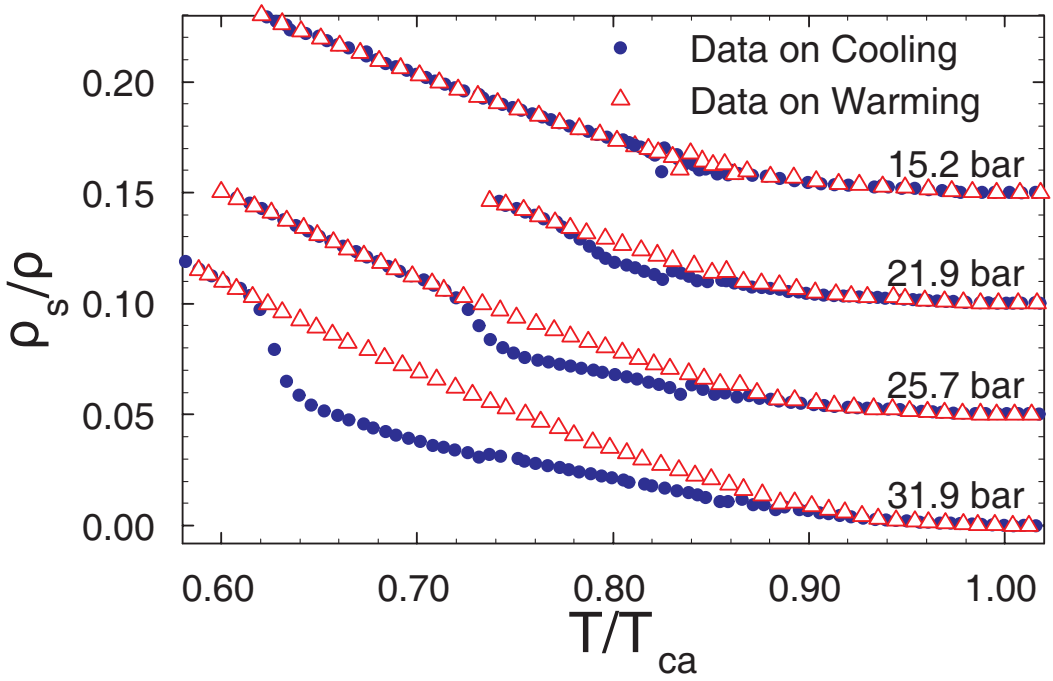

Figure 6.7: The superfluid fraction (ρ_s/ρ) vs temperature after the bulk superfluid contribution is subtracted. The (blue) circles and (red) triangles represent data obtained while cooling and warming respectively at various pressures (offset by 0.05 for clarity).

superfluid fraction determined this way is shown on the lower panel of fig. 6.6.

One of the goals for this experiment is to determine whether the A phase would reappear on warming. As mentioned in section 3.3.1, in isotropic aerogels, the A phase does not reappear on warming. However, in fig. 6.6 we observe that the cooling and warming traces join at temperature lower than T_{ca}, and at nonzero superfluid fraction. This indicates that the fluid is in the same state at the region right below T_{ca}, namely the A phase. Unlike isotropic aerogels, the A phase reappears on warming.

Orientation of the ℓ-vector

From fig. 6.5, it is evident that the superfluid fraction of the A phase is significantly smaller than the B phase. In fact the ratio of the measured superfluid fractions in the A vs B phase is very similar to what was observed in uncompressed aerogels [39]. In section 3.4, we noted that there were two competing predictions for the alignment of the ℓ-vector by anisotropic disorder: ℓ-vector being in the "easy axis" – the direction of the compression axis or in the "easy plane" – perpendicular to the compression axis. From our data, we can conclude that the prediction by Volovik in [42] was not realized, if the ℓ - vector was aligned in the direction of compression we will measure larger superfluid fraction in the A phase compared to the B phase. Instead, our measurements support the hypothesis of ℓ-vector being aligned perpendicular to the compression axis.

Pressure dependence

Data for several experimental pressures is shown in fig. 6.7. As the pressure is lowered, the hysteresis window of metastability of the A and B phases on cooling and warming respectively shrinks. Also the difference between A and B phases gets less pronounced. At pressures below 10 bar, we cannot distinguish the exact beginning and end of A to B and B to A transitions. This is partly due to the interference of the interceding slow-mode resonance modes [65] that obscure the data at the region where the A - B hysteresis loop should be.

As the pressure is lowered the transition temperature of the fluid in the aerogel, T_{ca} is more and more suppressed compared to the bulk. Also, as seen in fig.

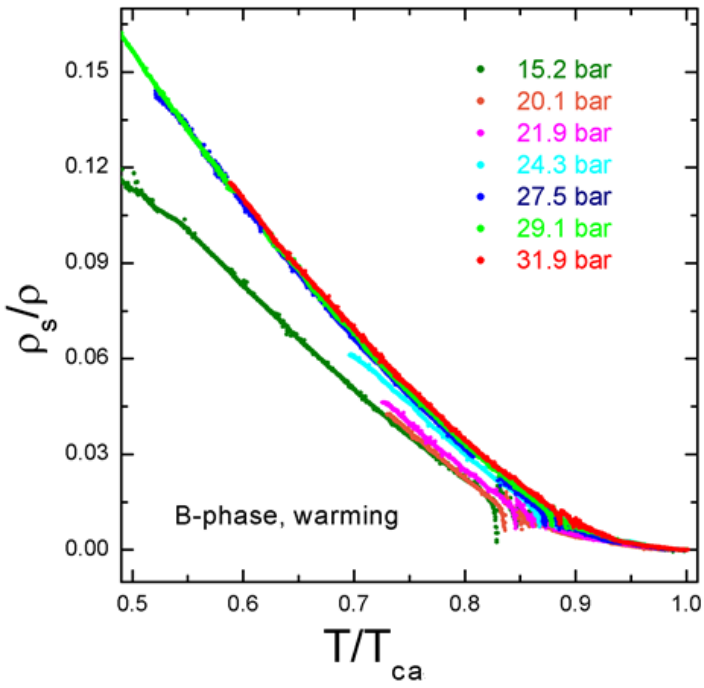

Figure 6.8: Pressure dependence of the measured superfluid fraction for various experimental pressures. Plotted is the data in the B phase (data taken on warming) versus T/T_{ca}.

6.8, the superfluid fraction (and hence the size of the superfluid gap) is seen to be lower as pressure is lowered. This ties in with the concept of gapless superfluidity discussed in section 3.3. The lower the pressure, the more the gap and subsequently the superfluid transition temperature suppression is. At the lowest experimental pressures (below 4 bar), no superfluid transition was observed down to the lowest measured experimental temperatures (~ 0.4 mK).

6.3.1 Width of transitions. Identifying the boundaries of the B to A transition

The A to B transition on cooling is not instantaneous unlike in bulk; it has a finite width of $\approx 70\,\mu$K. It is likely that this is due to inhomogeneity of the sample or due to pinning of the phase boundary by impurities. The observed width of the $A \rightarrow B$ transition suggests that the $B \rightarrow A$ transition might also be wide. Thus we sought to resolve the conversion of B phase to A phase by conducting a series of "turn around" measurements warming the pendulum at 30-60 μK/hr followed by a period of several hours where the pendulum was warmed slowly (2-3 μK/hr) until we reached our target temperature. The cell was then cooled again at 30-60 μK/hr back into the B phase. It was evident that the Q^{-1} signature at the $A \rightarrow B$ transition was a very sensitive indicator of the presence of A phase, B phase or an admixture of the two. Data for $Q^{-1}(T)$ at 31.9 bar, as turn arounds proceeded to successively higher temperatures, are shown in Fig. 6.9. Based on these turnarounds this sample the width of the $B \rightarrow A$ transition can be seen to be $\approx 70\,\mu$K. The nucleation of the B phase in aerogel is not influenced by the adjacent bulk B phase evidenced by the persistence of A phase below the bulk $A \rightarrow B$ transition (Fig. 3). At temperatures between the beginning and the end of the transition, we have part of the fluid in the aerogel being in the A phase, and part in the B phase. This distribution of admixture of A and B phases persists upon subsequent cooling to low temperatures until we reach the temperatures of the A to B transition.

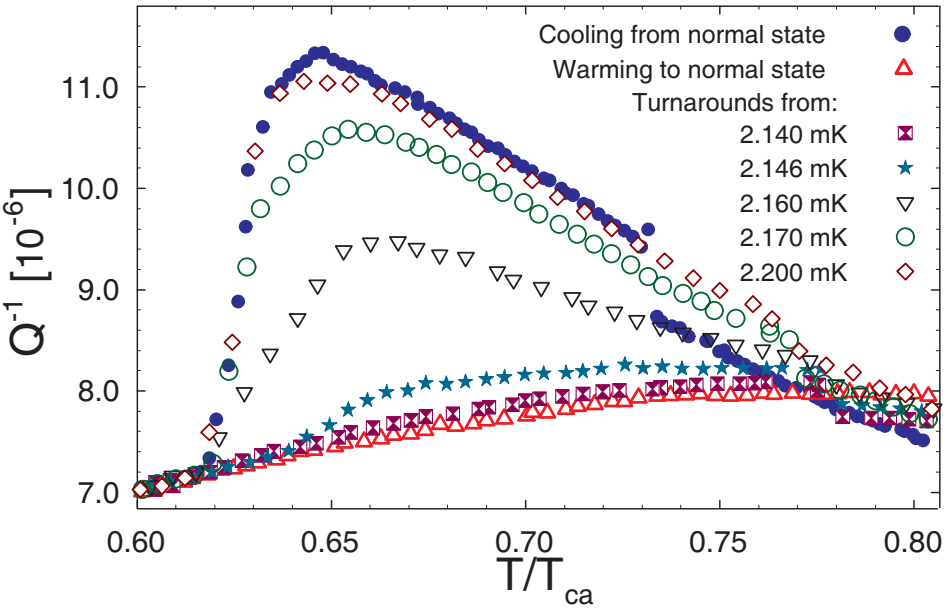

Figure 6.9: Dissipation data for turn around measurements at 31.9 bar, in the vicinity of the $A \rightarrow B$ transition. The (blue) circles and (red) triangles represent data taken on cooling from, and warming to, T_{ca} respectively. The intermediate points represent data taken on cooling, following turn-arounds at the temperatures given in the legend. The abrupt jump near $0.73T/T_{ca}$ in solid circles is the signature of the bulk $A \rightarrow B$ transition.

6.3.2 Phase Diagram

Determining the superfluid transition temperature and the temperatures for the A to B and B to A transitions we can put all together in the phase diagram shown in fig. 6.10. On cooling the A phase persists to lower temperatures compared to the bulk transition temperatures (even when the bulk is supercooled). The anisotropy of the aerogel is seen to extend the region of stability of the metastable A phase.

A phase reappears on warming, so a thermodynamically stable region in which A phase is the minimum energy state for both cooling and warming is observed. Unlike the bulk, there is no polycritical point in the phase dia-

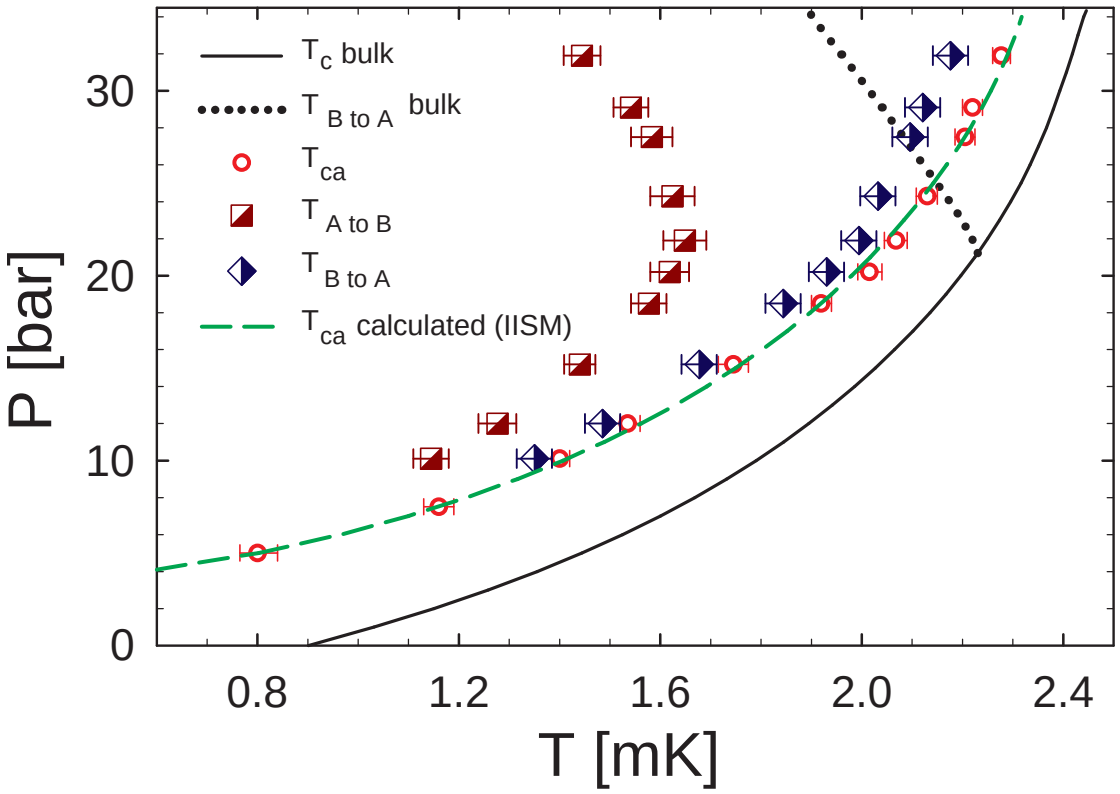

Figure 6.10: The phase diagram for superfluid ^{3}He in 10% axially compressed, 98% open aerogel determined by this experiment.

gram. Instead the region of stability forms a sliver that thins as the pressure is lowered, but persists to pressures far lower than the polycritical point pressure (21.22 bar). Disappearance of the polycritical point and sliver-like shape for the A phase stability region is seen in bulk when magnetic field is applied (as discussed in section 2.6). In the present experiment, the magnetic field is zero, but the effect is precipitated by the anisotropy of the aerogel induced disorder.

T_c suppression. Mean-free-path and the aerogel coherence length

As discussed in section 3.3.1, there are several models that can describe the suppression of the superfluid transition temperature and the superfluid gap for the ^{3}He embedded in the the aerogel. These models were well summarized in Ref. [36] and [66]. The Isotropic Inhomogeneous Scattering Model (IISM) proposed and described in these references has been very successful in fitting the several sets of existing experimental data for the T_c suppression caused by the presence of aerogel impurity. Fitting to our data (green line in Fig. 6.10), we observe an excellent fit, given that the mean-free-path limit for the quasiparticles within the aerogel is 140 nm and the aerogel coherence length is 45 nm.

6.4 Anomalous dissipation in the superfluid state

Previous experiments mostly concentrated on the pendulum period shift of the pendulum due to the superfluid. This experiment is the first such experiment where the pendulum dissipation in the superfluid state has been investigated thoroughly. A model for the pendulum dissipation due to the normal fluid embedded in the viscoelastic aerogel was proposed and tested. The results of these measurements were published in [67].

Here, we will touch on the pendulum dissipation that was seen in the superfluid state. As was already seen in fig. 6.9, the measured dissipation was seen to be significantly higher in the A phase than in the B phase. A comprehensive summary of the measured dissipation for several experimental pressures plotted versus the superfluid fraction are shown in fig. 6.11. Panel (a) shows the

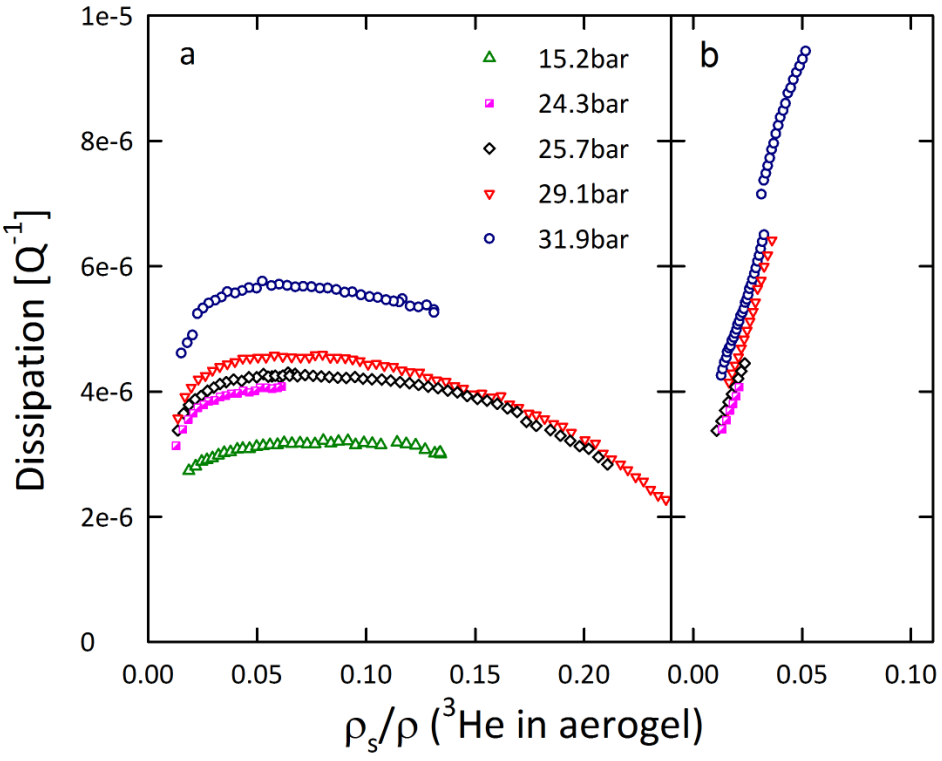

Figure 6.11: (a) Data for Q^{-1} in the B-phase vs ρ_s/ρ for various pressures combined in one plot.
(b) Plot of Q^{-1} in the A-phase vs ρ_s/ρ for various pressures. Discontinuities in the data are due to the bulk $A \rightarrow B$ transition on cooling.

dissipation measured in the B phase and panel (b) shows the dissipation in the A phase.

The two superfluid phases have fairly different signatures and superfluid fraction dependence. In the B phase, the dissipation has a broad peak, it rises up shortly below T_{ca} to a maximum value at around $\rho_s/\rho = 0.07$, and then steadily decreases as we go deeper in the superfluid state. In contrast, the dissipation seen in the A phase rises up sharply and steadily in a linear fashion as we go deeper into the superfluid state. This is at odds with our *a priori* expectations. While it is expected to see higher dissipation in the A phase than in the B phase

due to the gap nodes, normally dissipation is seen to decrease with the rise of the superfluid fraction. It is also interesting to note the pressure dependence of the dissipation data: dissipation is seen to increase with pressure.

The "anomalous" dissipation dependence on the superfluid fraction (and not on the temperature) is a clear mark that this effect comes from the fluid embedded in the aerogel. Note that we have subtracted the expected contribution from the bulk. While the extra dissipation could be associated with the presence of low energy surface states within the superfluid gap, it is not clear why the dissipation would rise with increase in pressure (which should increase the size of the gap for the "dirty" superfluid) or with increase in the superfluid fraction.

A more compelling explanation is that the "anomalous" dissipation seen in the A phase related to the orbital viscosity of the superfluid texture. The orbital viscosity parametrizes the resistance of the ℓ-vector field to a change in direction [68, 69]. Previous experiments with samples of aerogel attached to vibrating wire resonators immersed in ^{3}He show that flow tends orient the ESP state orbital texture along the flow [70]. Such an effect is clearly demonstrated for velocities significantly larger than the velocities of the fluid in our experiment, but alignment of the ℓ-vector is possibly realized also at lower velocities, albeit with a smaller magnitude. Changing the direction of the ℓ-vector will dampen the flow due to the orbital viscosity of the superfluid and manifests itself as the extra dissipation of the pendulum observed in the ESP state. A similar (but smaller) effect has been shown for the B-phase if the order parameter is slightly anisotropic.[71]

6.5 Conclusion

In this experiment we showed that the addition of anisotropic disorder in the form of a uniaxially compressed aerogel radically alters the superfluid phase diagram for the embedded ^{3}He fluid, compared to the bulk. The anisotropy of the aerogel has the effect of enhancing the width of the metastable A phase and increasing the width of the region where the A phase is the lowest energy state (even when compared to an identical uncompressed sample), all in zero magnetic field. The reappearance of the A phase from the B phase on warming is manifested at pressures well below the bulk polycritical point.

Alignment of the angular momentum ℓ by compression, predicted in Ref. [42], is not observed. In addition, we observed increase of the measured dissipation due to the rise in the superfluid fraction, especially in the superfluid state. Such an effect is counter to what we would expect in the bulk and could be related to the damping of the motion of the superfluid texture by the aerogel or to the presence of low lying energy states that emerge within the superfluid gap due to the presence of the aerogel disorder.

Results presented in this chapter have been published in two journal publications: [67] and [72]. Portions of the text and several figures presented in this chapter have been taken from these two sources.

CHAPTER 7

SUPERFLUID ^{3}HE IN NEMATICALLY ORDERED AEROGEL

We measured the superfluid the period shift and the dissipation of the pendulum for six experimental pressures – 0.1, 3.6, 7.5, 15.4, 29.1, and 32 bar. This allowed us to infer the superfluid fraction of the fluid embedded in the strongly anisotropic aerogel, and observe signatures of multiple phase transitions. Our torsional oscillator experiment probes the superfluid density in the direction perpendicular to the pendulum axis, and hence perpendicular to the aerogel strands.

Data for 7.5, 15.4, 29.1 and 32 bar were obtained by filling the aerogel with pure ^{3}He (less than 10 ppm of ^{4}He). Data for 0.1, 3.6 bar as well as repeated measurements at 15.4 and 29.1 bar were taken after the aerogel surface was pre-plated with ~ 2 monolayers of ^{4}He. No substantial change in the transition temperatures at 15.4 and 29.1 bar was seen between measurements with or without pre-plated ^{4}He surfaces. It is not clear if the ^{4}He changed the specularity at the aerogel surface. Pre-plating with ^{4}He, however, changed the spectrum of the sound modes which are excited in the superfluid (more details on these sound modes will be discussed in the following sections).

7.1 Empty cell data

In order to extract the inferred superfluid fraction from the period shift of the torsion pendulum, we need first to characterize the temperature dependence of the period of the empty pendulum. Data for the empty pendulum period ver-

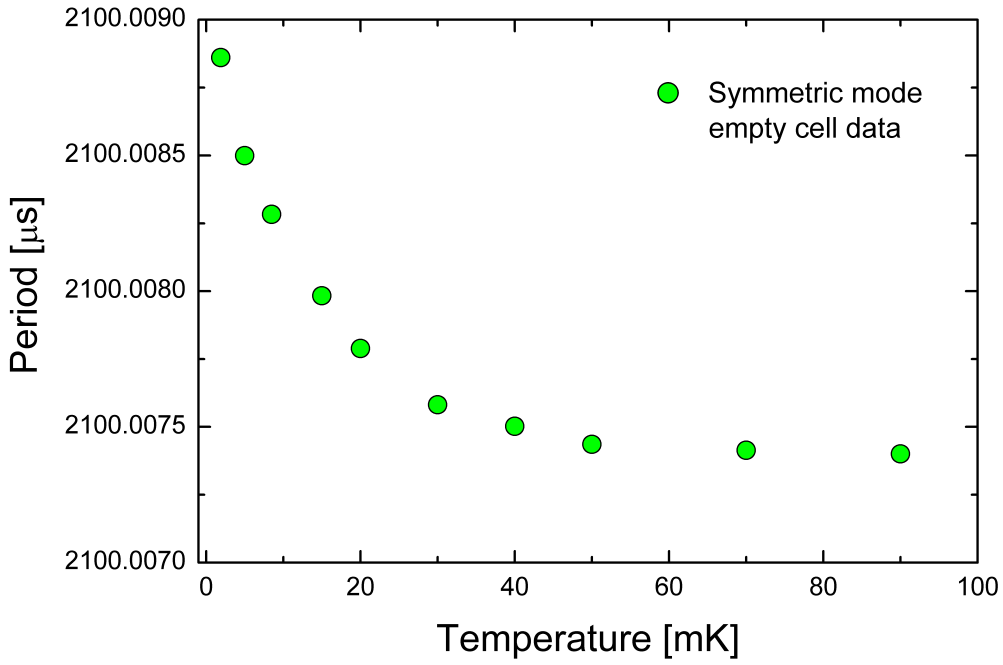

Figure 7.1: Torsion pendulum period versus temperature for the empty cell in the symmetric torsion mode.

sus temperature when the pendulum is excited in its symmetric torsion mode is shown in fig. 7.1. Unlike the squeezed aerogel experiment, the torsion rod was made from coin silver, which has a significantly smaller temperature dependence of its period, compared to torsion rods made from beryllium-copper. Any uncertainty in our measurements due to empty cell period estimation is minimal.

7.2 Calibration with ^{4}He

Because the shape of the aerogel sample is not rotationally symmetric, the fluid in the corners will contribute to the pendulum moment of inertia even in the superfluid state. To account for this and also for the entrainment of the fluid

by the strands of aerogel (Kelvin drag), we calibrated the superfluid fraction by filling the sample with pure ^{4}He. Because the healing length of ^{4}He is $\sim$ 0.1 nm, it is expected that the entire sample should be superfluid (aside from 1-2 monolayers of disordered solid on the surfaces). Thus from a measurement of the frequency of the empty cell, of the pendulum above the lambda transition, and at low temperatures well below T_λ, we determined that three quarters of the fluid inertia decoupled. Thus to find the superfluid fraction, we need to modify eq. 5.2 into:

$$\frac{\rho_s}{\rho} = \frac{1}{3/4}\frac{\Delta p(T)}{\Delta p_{max}} \tag{7.1}$$

7.3 Determination of the bulk fluid contribution

The period and the quality factor of the oscillator changes below T_c^{bulk}, indicating the decoupling of the superfluid fraction of bulk fluid. While the aerogel sample is completely encapsulated with epoxy, so no voids should exist along its periphery, electron microscope images taken on this type of aerogel show the presence of discontinuities and micro-cracks dispersed throughout the sample that could harbor bulk-like fluid.

As we go to temperatures below T_c^{bulk}, a faster drop in the resonant frequency (rise in the superfluid fraction) is observed below a temperature T_{ca}, which we identify as the transition temperature for the fluid within the aerogel. Fig. 7.2 shows the superfluid fraction calculated by eq. 7.1 for 0.1 bar. At 0.1 bar, the difference between T_c^{bulk} and T_{ca} is the largest. Using the values for the bulk superfluid fraction from [63], and scaling them by a factor of 0.03, we obtain a good fit to the data between T_c^{bulk} and T_{ca}, indicating that the bulk fluid moment

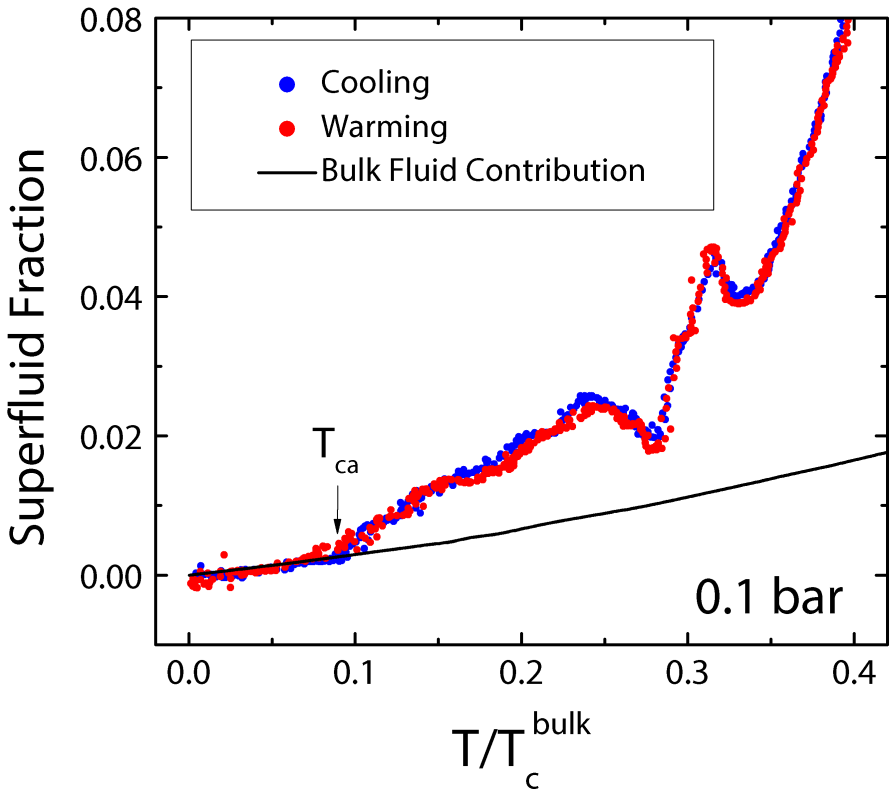

Figure 7.2: Superfluid fraction versus T/T_c^{bulk} for 0.1 bar. Shown is data on cooling and warming (blue, red dots), as well as the estimated bulk fluid contribution to the superfluid fraction (black line). The superfluid transition for the fluid in the aerogel is marked by an arrow.

of inertia amounts to about 3% of the total fluid inertia in the pendulum. In this case, eq. 7.1 needs to be modified in order to determine the superfluid fraction only of the fluid within the aerogel in the following way:

$$\frac{\rho_s}{\rho} = \frac{1}{3/4}\frac{\Delta p(T)}{\Delta p_{max}} - 0.03\frac{\rho_s}{\rho}^{bulk} \tag{7.2}$$

7.3.1 Slow mode sound resonances

Starting from the two fluid model for superfluids, there are many ways in which sound can propagate though the liquid medium. In bulk ^{3}He one finds first (normal and superfluid components move in-phase), second (normal and superfluid components move out-of-phase) and fourth sound (as discussed in section 6.2.1, the normal component is clamped, but the superfluid component oscillates). In aerogel, the normal fluid is well clamped to the aerogel strands, while the superfluid is free to move, very much like in the case of fourth sound. However, the aerogel is not perfectly rigid, but can flex as well. Thus sound modes for ^{3}He in aerogel are composite modes in which the aerogel, the normal and the superfluid components all move. Two such modes are possible, the fast mode in which all components move in phase, and a slow mode in which the superfluid component is out-of-phase with the flexing of the aerogel strands and the normal component [65]. The sound velocity of the slow mode, c_s, is related to the speed of sound in aerogel, c_a, and the superfluid fraction, ρ_s/ρ, through the following expression:

$$\frac{c_s}{c_a} = \left(\frac{\rho_a}{\rho(P)} \frac{\rho_s}{\rho} \right)^{1/2} \tag{7.3}$$

where $\rho(P)$ is the density of the fluid at the particular pressure. Since c_s depends on ρ_s/ρ, the slow-mode sound velocity (and therefore the wavelength at a particular excitation frequency) changes rapidly with temperature below the superfluid transition, starting at zero at T_{ca}.

As we already discussed in the context of fourth sound resonances (section 6.2.1), when the resonant frequency of the sound standing wave mode crosses the driving frequency of the pendulum, we observe peaks in the measured dissipation and ripples in the measured period (hence superfluid fraction).

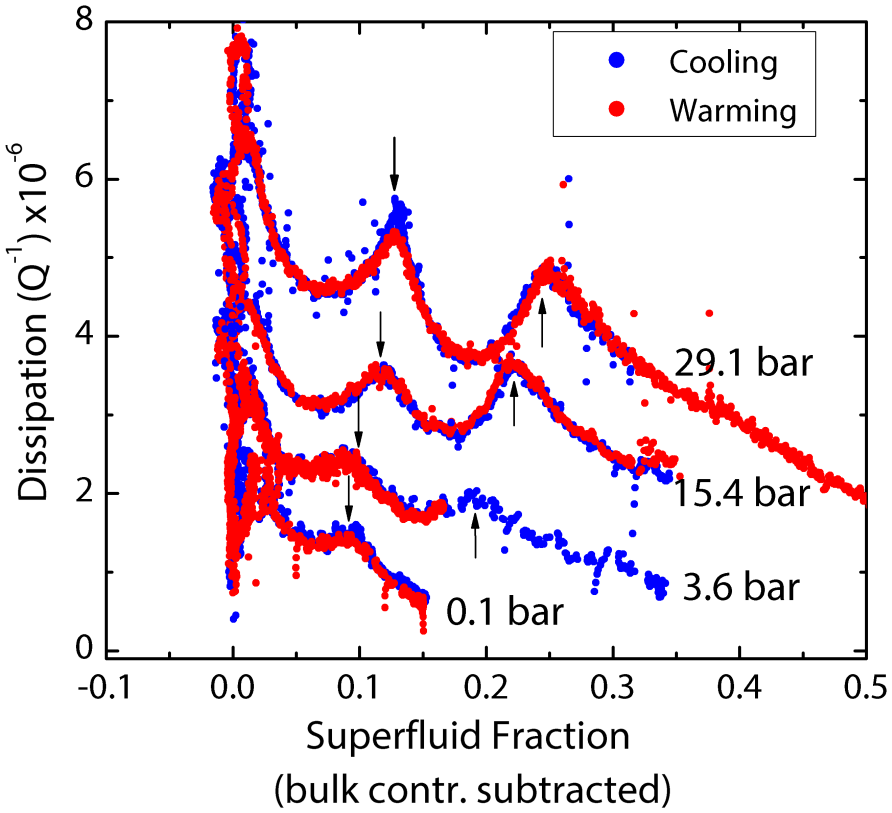

Figure 7.3: Dissipation versus superfluid fraction for the fluid embedded in the aerogel (bulk contribution is subtracted) at 0.1, 3.6, 15.4, and 29.1 bar. Visible are several sound resonance peaks. We highlight two sets of slow-mode sound resonances, at values of about 0.1-0.12 and 0.2-0.24 for the superfluid fraction. Arrows indicated the expected locations of the dissipation peaks based on the data for 29.1 bar and the ratios of the fluid densities at the other pressures.

We can use the slow-mode sound resonance to verify that the bulk contribution to the moment of inertia is indeed 3%. In particular, we track the slow-mode sound resonance dissipation peaks for each experimental pressure (fig. 7.3). Sound resonances occur at the same values for c_s for each pressure, and since ρ_a and c_a are fixed, then ρ_s/ρ at the dissipation peaks should scale as the density ρ for different pressures (eq. 7.3). Two sets of arrows in fig. 7.3 indicate the predicted ρ_s/ρ for two of the prominent dissipation peaks in our data. The

values ρ_s/ρ for 29.1 bar were set by the data, and the values for ρ_s/ρ at the lower pressures were determined by multiplying ρ_s/ρ (29.1 bar) by $(\rho_s/\rho\,(P))/(\rho_s/\rho$ (29.1 bar)). We observe good agreement between the observed and predicted location of the sound resonance dissipation peaks, which would not have been the case if we had incorrectly estimated the bulk contribution.

7.4 Experimental data in the superfluid state

Data for the superfluid fraction versus T/T_c^{bulk} for 6 different pressures ranging from 32 bar, down to 0.1 bar is shown in fig. 7.4. At high pressures (32, 29.1, 15.4 bar), a clear hysteresis loop is seen between warming and cooling, indicating a first order phase transition between and an A-like and a B-like phase. Guided by the results from NMR experiments done on a similar sample [73, 74, 75] and by the Ginzburg-Landau model predictions described in the following section, we identify these as polar distorted B, and polar distorted A. As pressure is lowered, the hysteresis loop gets less pronounced, indicating a larger degree of distortion of the phases. At 7.5 bar, the difference between the A and B phases is very small but hysteresis is still present (fig. 7.5), and at 3.6 and 0.1 bar no difference between cooling and warming is observed. At this lowest pressures we cannot tell if the low temperature superfluid state is A-like or B-like. Even if a hysteretic transition takes place, the signatures of the phases when the superfluid is probed in plane (perpendicular to the strands) could appear very similar in our measurements.

At temperatures slightly above the hysteresis loop, on both cooling and warming, we observe a sharp change in slope in the superfluid fraction versus

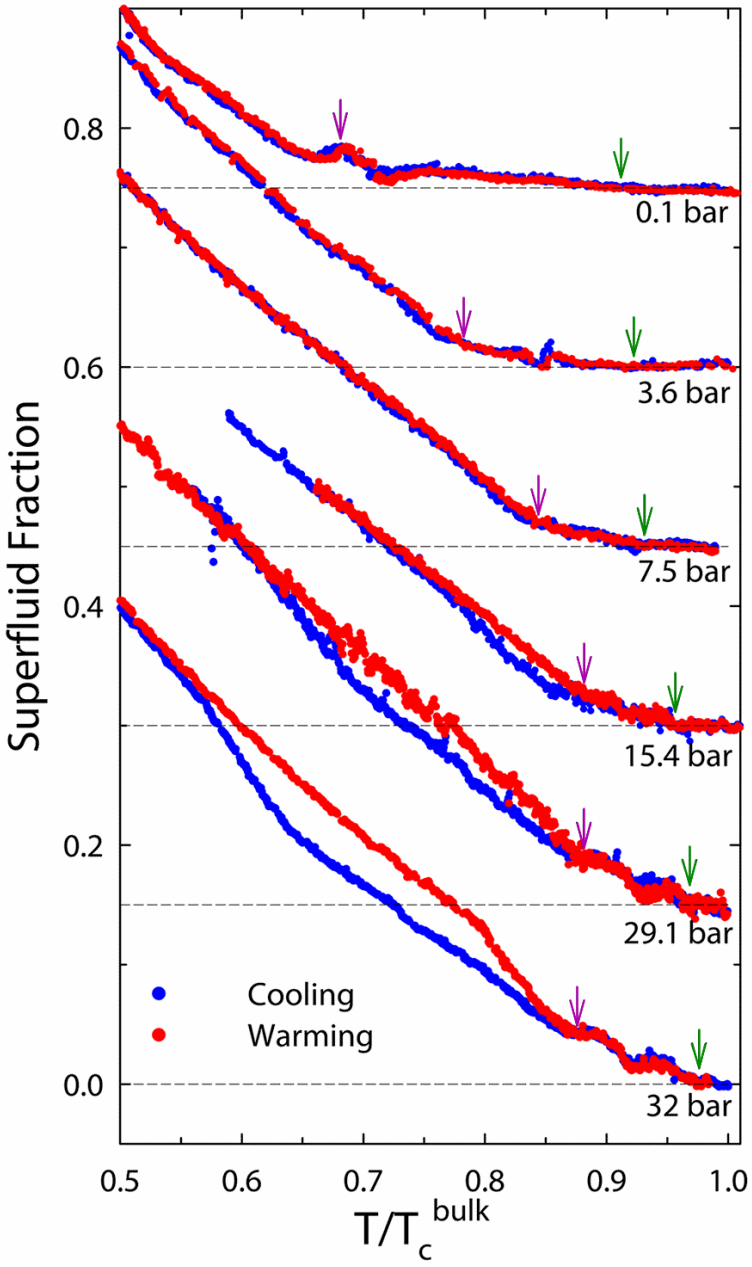

Figure 7.4: Experimental data for the measured superfluid fraction versus T/T_c^{bulk} for both cooling and warming at each of the experimental pressures. Data for each adjacent pressure is offset by 0.15 in the y-direction for clarity. Dashed lines indicate the zero superfluid fraction level for each pressure. Green arrows mark the superfluid transition temperature for the ^{3}He in the aerogel T_{ca}. Magenta arrows indicate the point at which change in the superfluid fraction data is observed T_{kink}.

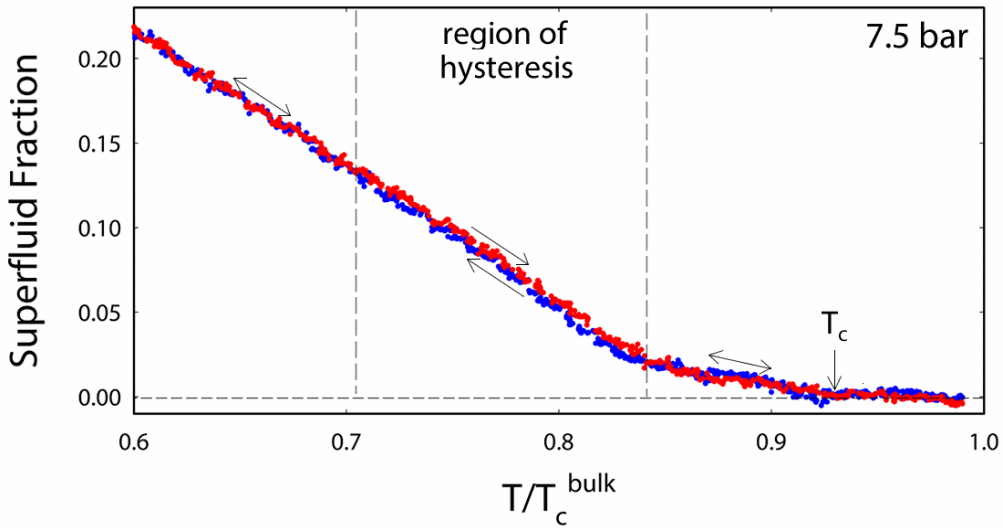

Figure 7.5: Data for 7.5 bar. A region of slight hysteresis between cooling and warming is bounded by two vertical dashed lines.

T (see fig. 7.4). The change in slope is especially pronounced at low pressures. We label the temperature of this feature as T_{kink}. At 7.5 bar (fig. 7.5), there is clear indications of both a region of hysteresis, associated with an A to B transition, and a very sharp and pronounced kink in the superfluid fraction data. It is evident that there are three superfluid phases present. Near T_{ca}, a high temperature phase is stable, which transitions on cooling to a distorted A phase. Cooling through the region of hysteresis, the distorted A phase transitions to a distorted B phase. On warming, the distorted B phase persists through the region of hysteresis until it transitions to the high temperature phase just below T_{ca}. We identify T_{kink} as the temperature of the phase transition between a high temperature superfluid phase and A or B phase. No hysteresis is associated with the transition at T_{kink}, therefore the transition is second order. The superfluid phase right below T_{ca} is identified by NMR as an equal spin pairing phase [73, 74, 75], but as discussed in section 2.4, both the A phase and the Polar phase are characterized by equal spin pairing.

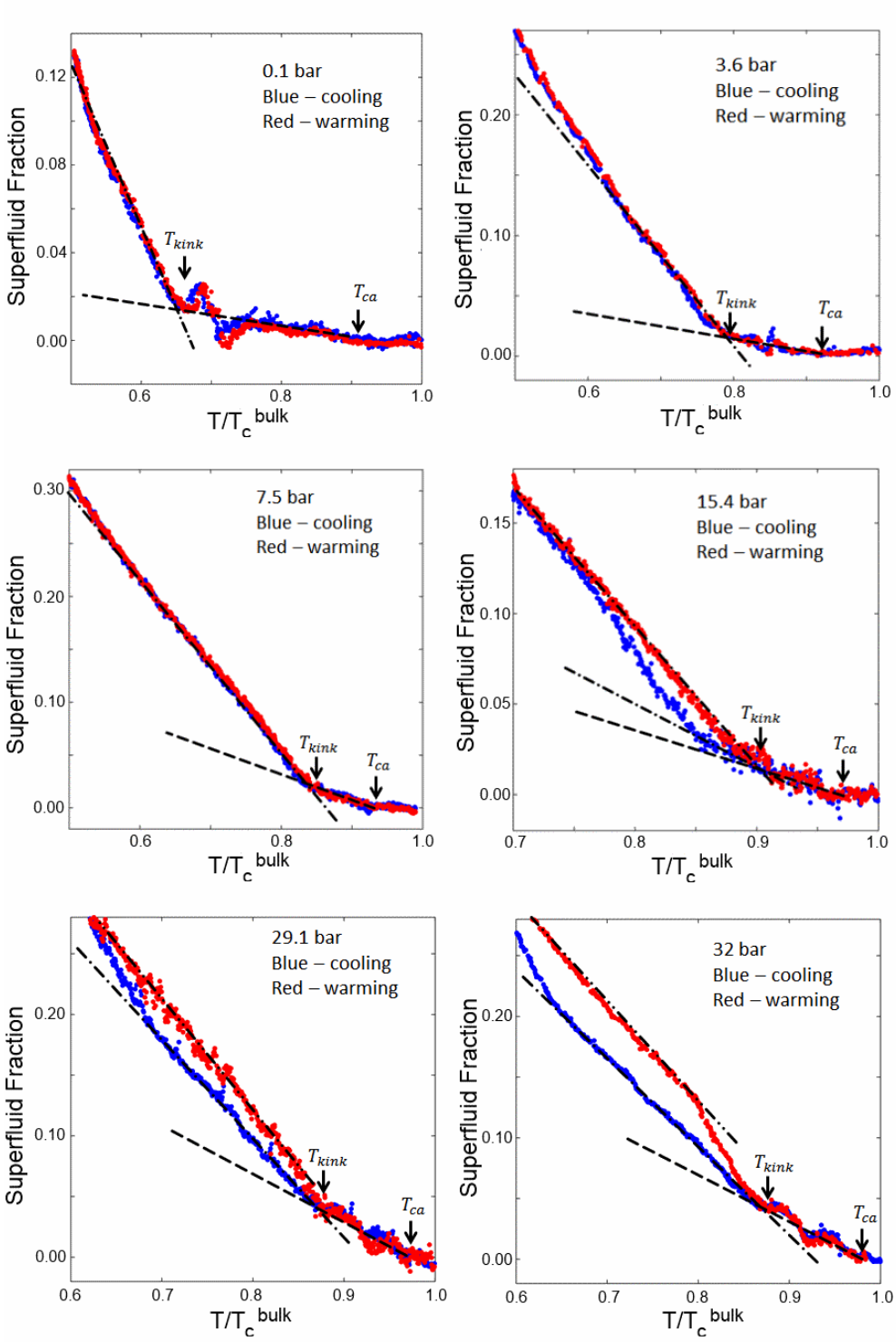

Figure 7.6: Plots of the superfluid fraction versus T/T_c^{bulk} for the six experimental pressures. Data for each experimental pressure is shown in a separate panel. Highlighted are T_{kink} and T_{ca}. Lines are drawn to be guides for the eye and illustrate the change in slope at T_{kink}.

7.5 Ginzburg-Landau model for the fluid in the nematically ordered aerogel

Due to the geometry of the highly oriented aerogel, we would expect the nodal direction in the A-phase to point perpendicular to the strands. This has been confirmed using NMR in Ref. [75]. The 3 by 3 order parameter matrix ansatz that describes the possible superfluid states for the fluid in the ordered aerogel has the following form:

$$\hat{A} = \begin{pmatrix} A_\perp & 0 & 0 \\ 0 & A_\perp & 0 \\ 0 & A_y & A_\parallel \end{pmatrix} \tag{7.4}$$

The conventional bulk A-phase corresponds to $A_y = A_\parallel$ and $A_\perp = 0$. Similarly, the isotropic B-phase has $A_\perp = A_\parallel$ and $A_y = 0$. If $A_\parallel \neq 0$ and $A_\perp = A_y = 0$, then this will represent the Polar phase. Starting from eq. 2.9 with a modification that accounts for the effects of the anisotropic disorder suggested by Ref. [44] and Ref. [76], the form of the Ginzburg-Landau (GL) free energy takes the following form:

$$\begin{aligned} F = &-\left(\frac{T_{ca}-T}{T_c^{bulk}}\right)\Delta^2\left|A_\parallel\right|^2 - \left(\frac{T_{ca}-T}{T_c^{bulk}}+\delta\right)\Delta^2\left(2|A_\perp|^2+\left|A_y\right|^2\right) + \beta_1\left|\mathrm{Tr}(\hat{A}\hat{A}^T)\right|^2 \\ &+\beta_2\left[\mathrm{Tr}(\hat{A}\hat{A}^\dagger)\right]^2 + \beta_3\mathrm{Tr}\left[\hat{A}\hat{A}^T(\hat{A}\hat{A}^T)^\dagger\right] + \beta_4\mathrm{Tr}\left[(\hat{A}\hat{A}^\dagger)^2\right] + \beta_5\mathrm{Tr}\left[\hat{A}\hat{A}^\dagger(\hat{A}\hat{A}^\dagger)^*\right] \end{aligned} \tag{7.5}$$

Here, Δ is the value of the condensation energy, T_{ca} and T_c^{bulk} the superfluid transition temperatures for the fluid within the aerogel and the bulk fluid respectively. The anisotropy in the system is parameterized by δ. The nonzero value of δ leads to two distinct transition temperatures, $T_{c\perp}$ and $T_{c\parallel} = T_{ca}$, below which the components of the order parameter perpendicular and parallel

to the aerogel anisotropy axis develop. More precisely δ can be defined as:

$$\delta = \frac{T_{c\parallel} - T_{c\perp}}{T_c^{bulk}} \left(1 + \frac{\beta_1 - \beta_2 + \beta_3 - \beta_4 - \beta_5}{\beta_1 + \beta_2 + \beta_3 + \beta_4 + \beta_5}\right) \tag{7.6}$$

In the linear pair-breaking regime, δ is given by:

$$\delta \cong -\frac{\pi^2}{4}\xi_0 \left(\frac{1}{\lambda_\perp} - \frac{1}{\lambda_\parallel}\right) \tag{7.7}$$

with ξ_0 being the zero-temperature coherence length, and $\lambda_{\perp,\parallel}$ being the quasi-particle mean-free-path perpendicular or parallel to the strands. This is where the extreme anisotropy of the aerogel comes into play. Spin diffusion measurements on a similarly grown "nematically" oriented aerogel reveal that the mean-free-path for a quasi-particle traveling along the strands is nearly twice that of one for a particle moving perpendicular to the strands [77].

Finding numerically the form of the order parameter $\hat{A}$ that minimizes the free energy for each pressure and temperature, we can make inferences for the equilibrium superfluid phases in different part of the phase diagram. For $T_{c\perp} < T < T_{c\parallel}$, this model predicts that the system will be in the polar phase ($A_{\perp,y} = 0$, $A_\parallel > 0$). For lower temperature, one finds either a distorted A phase, where $A_\perp = 0$ and $A_\parallel > A_y > 0$ or a distorted B phase, where $A_y = 0$ and $A_\parallel > A_\perp > 0$. The relative stability of these phases depends on the magnitude of the β terms in eq. 7.5. Quasi-particle mean-free paths in the nematic aerogel are expected to be relatively long (> 450 nm [77]), compared to the mean-free paths of ordinary silica aerogel ($\sim$ 100 nm). Thus, we believe that the β parameters are only weakly affected by the disorder, and in our analysis we use the bulk values given in Ref. [10].

The degree of polar distortion can be parameterized by $A_y/A_\parallel$ in the A-phase and $A_\perp/A_\parallel$in the B-phase. Both these ratios become smaller at lower pressures

(corresponding to more polar distortion), and all three phases become less distinct. The A to B transition is first order and is hysteretic, while A to Polar or B to Polar is second order and should be free of hysteresis.

7.6 Phase diagram. Correspondence between T_{kink} and $T_{c\perp}$

To test if T_{kink} is related to $T_{c\perp}$ we look for the value of the anisotropy parameter δ in eq. 7.5, such that we obtain the best match between the predicted values for $T_{c\perp}$ and the observed T_{kink} for a particular pressure. The resulting value for δ is of a similar magnitude compared to the one predicted in eq. 7.7, as we insert the values for $\lambda_{\perp,\parallel}$ measured by spin diffusion (450 nm and 850 nm [77]) insofar as the spin diffusion mean-free path is related to the mean-free path which enters eq. 7.7 (mass, thermal, and spin transport do not have the same mean-free path values, but are similar up to a numerical value of order 1). Using eq. 7.6 and the assumption that T_{ca} is $T_{c\parallel}$, we can find the locations of $T_{c\perp}$ at other pressures. T_{kink} conforms to our prediction for $T_{c\perp}$ reasonably well at low pressures (0.1, 3.6, 7.5, 15.4 bar). At high pressures (29.1 and 32 bar) the agreement is not as good and the kink is seen at lower temperatures than the predicted location of $T_{c\perp}$. Recent theoretical work argues that this Ginzburg-Landau theory may break down at high pressures [78], and this could be the reason why our predictions break down at the highest pressures.

Minimizing the Ginzburg-Landau free energy in eq. 7.5, we obtain the values for the equilibrium order parameter $\hat{A}$ and calculate the expected superfluid fraction using the recipe described in section 2.5. The only free parameter to adjust in this process is the value of Δ in eq. 7.5. As discussed in section 3.3, the

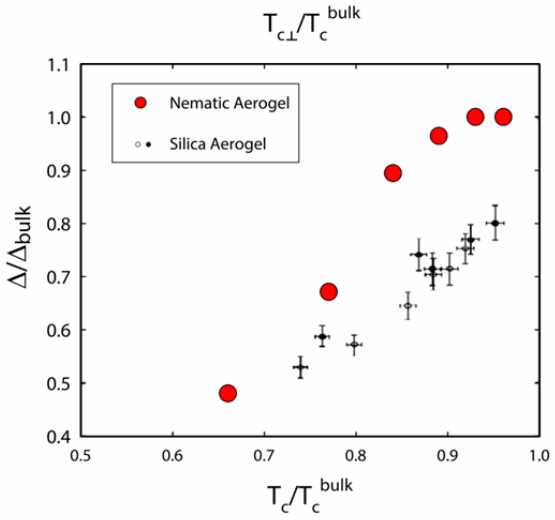

Figure 7.7: The ratio of the superfluid gap for the fluid in the aerogel over the superfluid gap of the bulk fluid is plotted versus the superfluid transition temperature suppression for different aerogel samples. Black filled and empty circles represent data from Ref. [79] plotted against T_c/T_c^{bulk} for two isotropic silica aerogel samples with different porosities (99.5% and 98%). Filled red dots indicate the factors by which we scaled the superfluid gap in our GL model calculated superfluid fractions for the present experiment plotted versus $T_{c\perp}/T_c^{bulk}$.

presence of disorder is expected to result in reduction of the superfluid gap. Figure 7.7 shows data compiled in Ref. [79] for the measured superfluid gap over the superfluid gap in the bulk fluid plotted versus the ratio of T_c in aerogel and in bulk for several isotropic (silica) aerogel samples. It is observed that a strong relationship between T_c suppression and gap suppression exists. In our aerogel sample (nematic aerogel), we take $T_{c\perp}/T_c^{bulk}$ to be the relevant parameter that should determine the ratio of the superfluid gap for ^{3}He in the aerogel compared to that in the bulk. Values for the ratio of the gap parameter Δ we used at each pressure and the bulk gap parameter Δ is shown in fig. 7.7 with filled red circles. This ratio was chosen to be temperature independent, but varied with pressure. As seen in the figure, the factors by which the gap is suppressed

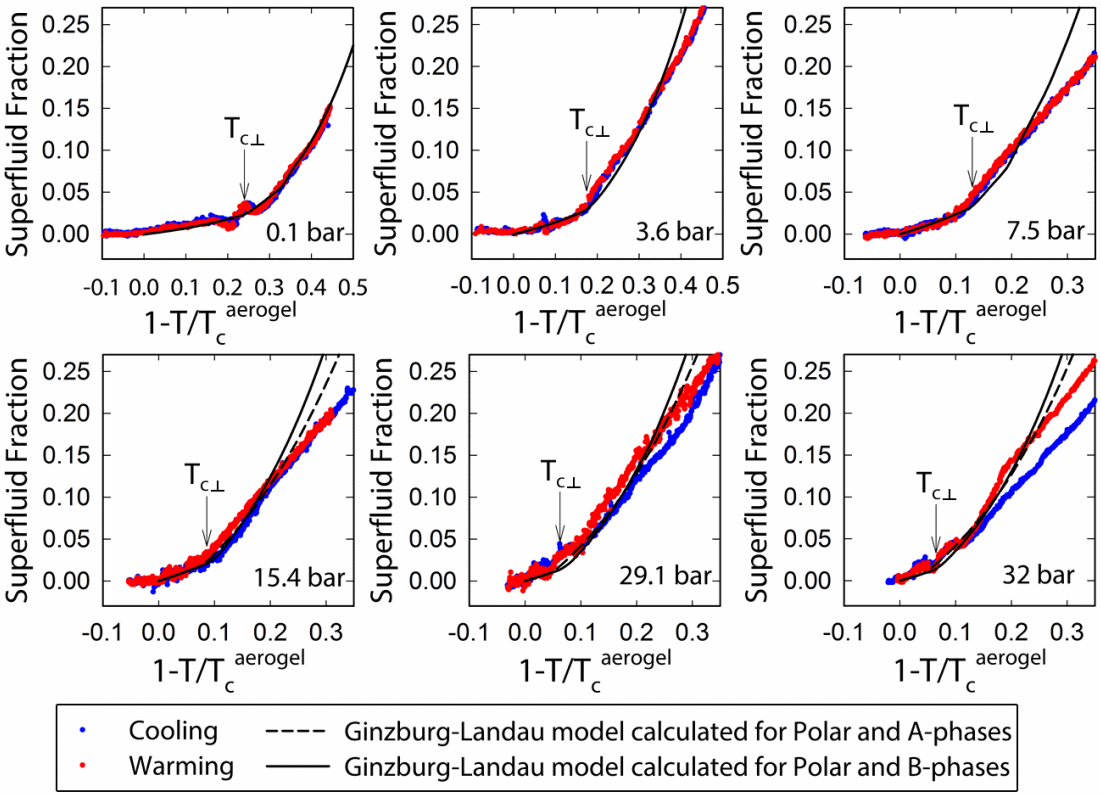

Figure 7.8: Superfluid fraction data (cooling and warming) plotted alongside the superfluid fraction calculated using a Ginzburg-Landau (GL) model for the ^{3}He in the nematically ordered aerogel.Data is plotted versus $1 - T/T_{ca}$, where T_{ca} is the temperature of the superfluid transition in aerogel. The temperature, $T_{c\perp}$,at which the components of the order parameter perpendicular to the strands become nonzero is indicated for each pressure with and arrow.

that best match the data vary roughly linearly with superfluid transition temperature suppression in a similar fashion as previously observed for the fluid in isotropic silica aerogels.

The calculated values for the superfluid fraction dependence on temperature, guided by our model, assume a transition from a Polar to an A or B phase. We see very good agreement, especially at low pressures, between the

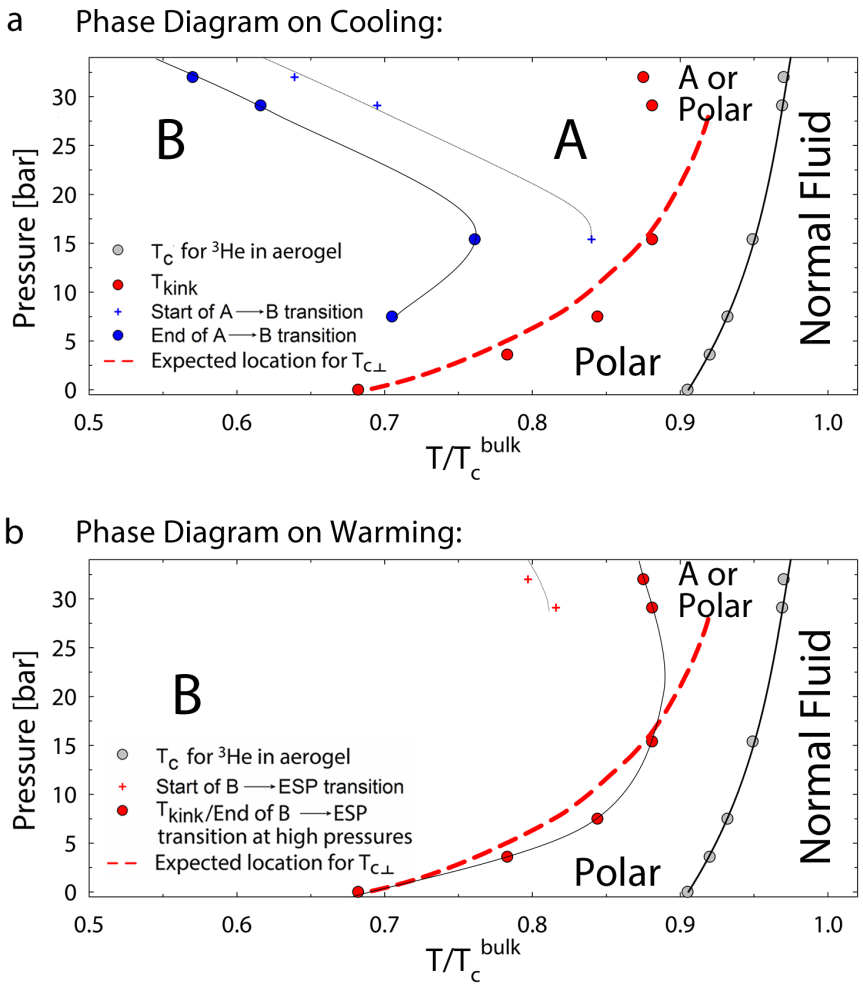

Figure 7.9: (a) Experimental phase diagram on cooling.
(b) Experimental phase diagram on warming

data and the calculated values (fig. 7.8). This leads us to conclude that at low pressures the high temperature phase has characteristics that correspond to the Polar phase, while at high pressures it has additional structure.

We summarize the locations of the observed phase transitions and we label the portions of the phase diagram according to the results of our analysis in fig. 7.9

7.7 Conclusion

This experiment revealed that embedding superfluid ^{3}He in a highly oriented aerogel produces striking new phenomena. The A and B superfluid phases are both distorted compared to their counterparts in the bulk, and their region of stability is markedly different compared to their stability in the bulk. We observe a phase which occurs just below the superfluid transition, which has no analog in the bulk. Our analysis points to the conclusion that at low pressures this superfluid state is closely related to the Polar phase.

Results presented in this chapter have been submitted for review to the journal Nature Physics. Portions of the text and some of the figures presented in this chapter have been included in the submitted manuscript.

CHAPTER 8

PHASE DIAGRAM OF A THIN FILM OF ^{3}HE CONFINED WITHIN A 1080 NM DEEP CAVITY

We present data in the superfluid state for five experimental pressures: 0.1, 1.4, 2.5, 3.6, and 5.6 bar. To enhance surface specularity, the surfaces of the experimental cell were pre-plated with roughly 50 μmol/cm^3 of ^{4}He, which amounted to ~ 3 monolayers of ^{4}He. This coverage was shown to be sufficient to make the surfaces nearly specular [52].

8.1 Determining the superfluid fraction from the torsion pendulum resonant frequency

Previous attempts of using a torsion pendulum to study confined films of ^{3}He encountered problems with the fluid decoupling from the pendulum walls at temperatures greater than the superfluid transition [80, 81], however, despite the extremely smooth surfaces of our cell, no sign of decoupling was observed in our experiment. In fig. 8.1a, we observe a constant shift of the torsion pendulum frequency data between the empty pendulum and the ^{3}He filled pendulum at a moderate pressure. In the experiment described in Ref. [80] the pendulum was filled at saturated vapor pressure. Due to the existence of liquid-vapor interface a vapor bubble could form within the cell. To avoid such possibility, the cell was filled above the critical pressure of ^{3}He.

Dissipation of empty and filled cell is plotted in Fig. 8.1b. The extra dissipation due to the fluid in the cell is very small compared to the empty cell dissipation. This is another indication that the fluid is well coupled to the cell

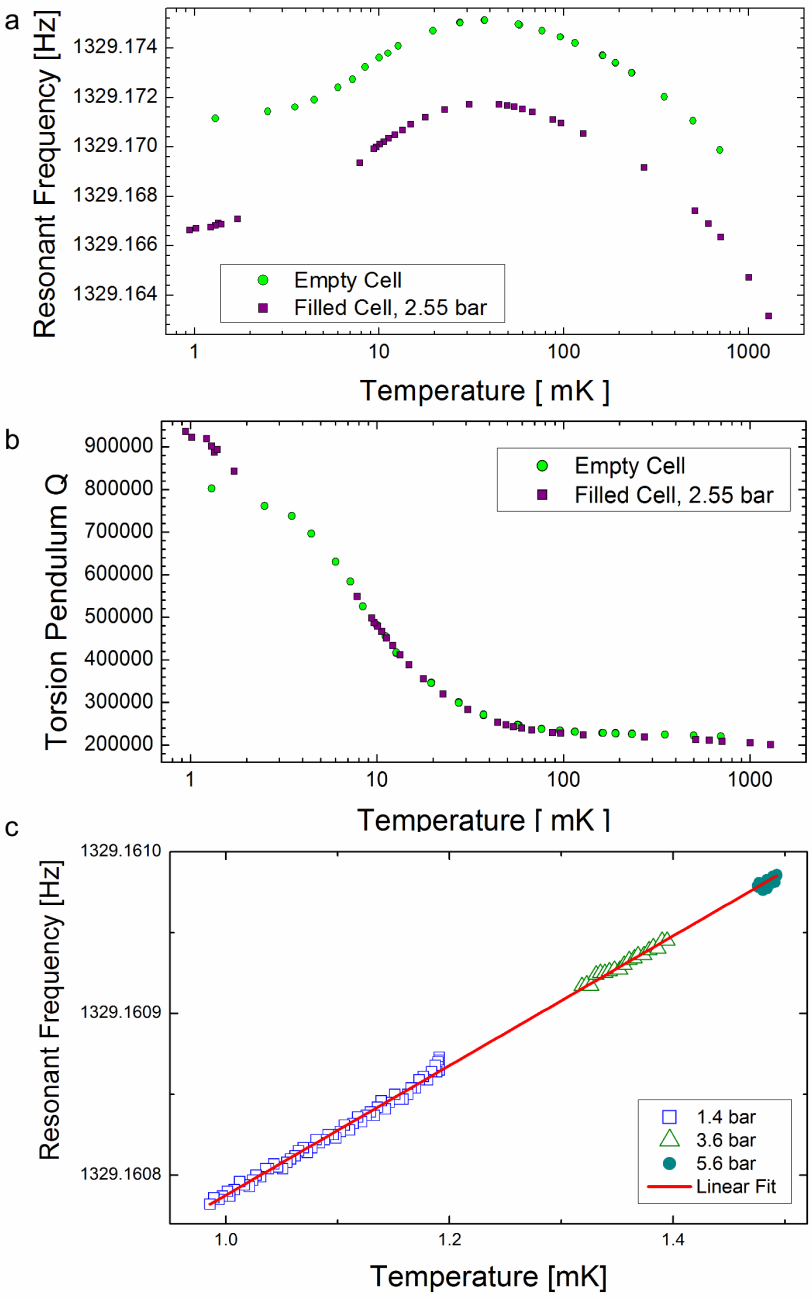

Figure 8.1: a. Data for the empty and ^{3}He filled (at 2.55 bar) torsion pendulum resonant frequency versus temperature.
b. Data for the empty and ^{3}He filled (at 2.55 bar) torsion pendulum quality factor versus temperature. Note that the empty cell seems to be unable to be cooled below $\sim$ 4 mK. This is probably due to a time-dependent heat leak from the cell head.
c. Data in the normal state torsion pendulum resonant frequency versus temperature for three experimental pressures adjusted by adding an appropriate constant so that all the data lies on the same line. The frequency shift versus temperature is indicative of the temperature dependence of the torsion constant.

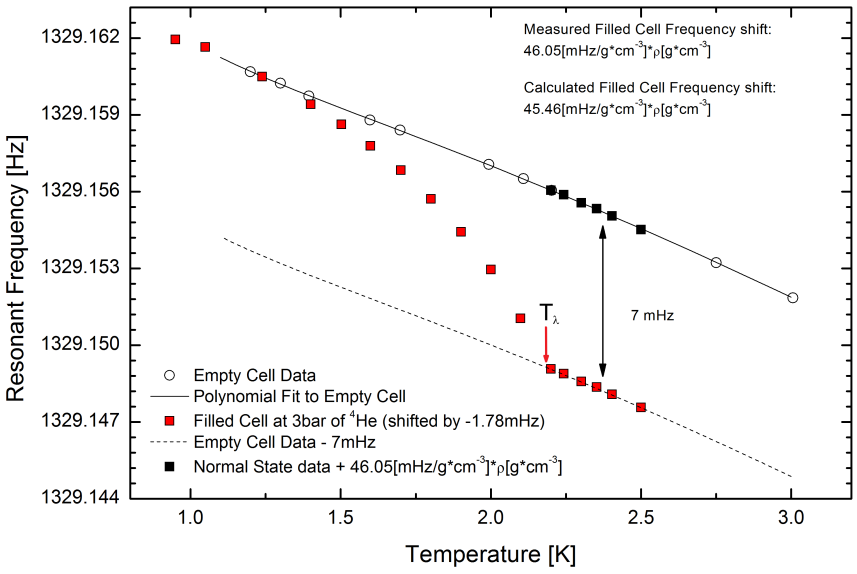

Figure 8.2: Data for empty cell and filled cell with ^{4}He (at 3 bar) torsion pendulum resonant frequency versus temperature. An arrow marks the position of T_λ.

walls, since the decoupling of the fluid is expected to be associated with a clear dissipation peak [81].

The resonant frequency shift at different pressures does not scale linearly with the fluid density. This phenomenon has been seen in the previous torsion pendulum experiments and is attributed to slight distortion of the torsion rod axis when the pressure is increased. Subtracting the period of the empty cell from the period of the filled cell is not sufficient to determine the frequency shift due to the coupled fluid. Instead, after we completed our experiments with ^{3}He, we filled the cell with ^{4}He and measured its frequency shift above and below T_λ. The results of these measurements are shown in fig. 8.2. Below 1 K, ^{4}He is nearly 100 % superfluid, so any difference between the filled cell and empty cell below 1 K will be only due to torsion rod distortion. It was determined

that this effect was responsible for a frequency shift of 1.78 mHz for 3 bar of pressure. After the effect of torsion rod distortion is accounted for, we observe that the difference for the torsion pendulum frequency between fully coupled fluid just above T_λ and the empty cell is 7 mHz. Using the appropriate values for the density of ^{4}He at these temperatures and pressure, we determine that the expression for the frequency shift due to the fully coupled normal fluid is:

$$\Delta f_{fully\ coupled} = 46.05[\mathrm{mHz}/(\mathrm{g}\cdot\mathrm{cm}^{-3})] \times \rho_{helium}[\mathrm{g}\cdot\mathrm{cm}^{-3}] \tag{8.1}$$

This expression is temperature independent for low temperatures (< 100 mK), since the density of the ^{3}He fluid does not change with temperature.

We expect that at temperatures of the order of a mK, the empty cell frequency to scale linearly with temperature. Direct measurements of the empty cell at these temperatures are not possible since we cannot cool the pendulum to temperatures lower than ~ 4 mK without employing the large thermal conductivity of the liquid ^{3}He. Instead, to determine the intrinsic temperature dependence of the pendulum frequency, we look at the normal state data for the various experimental pressures. Shifting the data for the different pressures accordingly, we see that the slope for the linear temperature dependence is 0.40056 mHz/mK (fig. 8.1c). We can now infer the superfluid fraction for the fluid within the torsion head from the experimental frequency $f(T)$ through the following expression:

$$\frac{\rho_s}{\rho} = \frac{f(T) - f_{normal}(T)}{\Delta f_{fully\ coupled}} \tag{8.2}$$

where $f_{normal}(T)$ is the linearly extrapolated normal state frequency to temperatures below T_c using the 0.40056 mHz/mK slope.

8.2 Temperature Calibration

During the course of this experiment, it was noted the unusually long time it took to achieve thermal equilibrium in the torsion pendulum after cooling or warming (ramping of the magnetic field) was stopped. Most likely, the silver sinter heat exchanger cooling liquid helium had deteriorated compared to the previous experiment. A larger thermal resistance between the fluid and the heat exchanger meant that small heat leaks into the helium will elevate its temperature in relation to the heat exchanger temperature. Fortunately, we could use the quartz tuning fork as a reliable thermometer measuring the actual temperature of the helium surrounding the fork, which is intimately connected to the ^{3}He within the torsion pendulum. For all pressures we measured, we observed that bulk superfluid transition measured by the quartz tuning fork occurred at a progressively lower temperature compared to the expected T_c (table 8.1). For each pressure, multiple cooling and warming ramps were performed. To account for thermal lag due to cooling and warming, the measured T_c was plotted versus the rate of change of temperature (warming rate was multiplied by a factor of 3, since heat capacity has a factor of ~ 3 jump just below T_c). The data for T_c versus rate of change of temperature falls on a straight line when plotted in this manner. The value for T_c measured in table 8.1 was determined from the y-intercept (T_c at zero rate of temperature change) of the linear fit to the data at each pressure. It is clear that there is some heat leak into the fluid, and since the heat exchanger thermal resistance gets higher with lower temperature, the thermal lag becomes more severe as temperature gets lowered.

Thermal resistance between the helium and the metal surface, known as the Kapitza resistance, is expected to scale as T^{-3}. Ref. [82] studied in detail the tem-

Table 8.1: Measured bulk T_c vs expected.

Pressure [bar]	T_c measured [mK]	T_c expected [mK]	$\Delta T(T_c)$ [mK]
5.6	1.460	1.506	0.046
3.6	1.286	1.331	0.045
2.5	1.137	1.219	0.082
1.4	1.009	1.094	0.085
0.1	0.798	0.927	0.129

perature dependence of the thermal resistance of silver sintered heat exchangers (the type we are using in our experiment), and found that while at higher temperatures the thermal resistance of the silver and the helium within the sinter pores affect the net heat exchanger resistance and lead to departure from the T^{-3} law, at low temperatures (below a few mK), all sintered heat exchangers exhibited the expected T^{-3} dependence. If the temperature lag is related to the heat exchanger thermal resistance as:

$$\Delta T = \frac{\dot{Q}}{R_{heat\ exchanger}} = \Delta T(T_c) \left(\frac{T_c}{T_{he}} \right)^3 \tag{8.3}$$

assuming that heat leak $\dot{Q}$ is constant throughout each data run, then for each pressure, we can turn the heat exchanger temperature (measured using the melting curve thermometer) into the temperature of the helium the following way:

$$T_{he} = T_{heat\ exchanger} + \Delta T(T_c) \left(\frac{T_c}{T_{he}} \right)^3 + \Delta T_{rate} \tag{8.4}$$

Here, ΔT_{rate} is the thermal lag due to nonzero cooling/warming rate. Assuming that ΔT_{rate} does not have a temperature dependence, ΔT_{rate} can be determined from the difference between the actual T_c measured for each particular data run and the y-intercept of the T_c versus rate of change of temperature plot (T_c

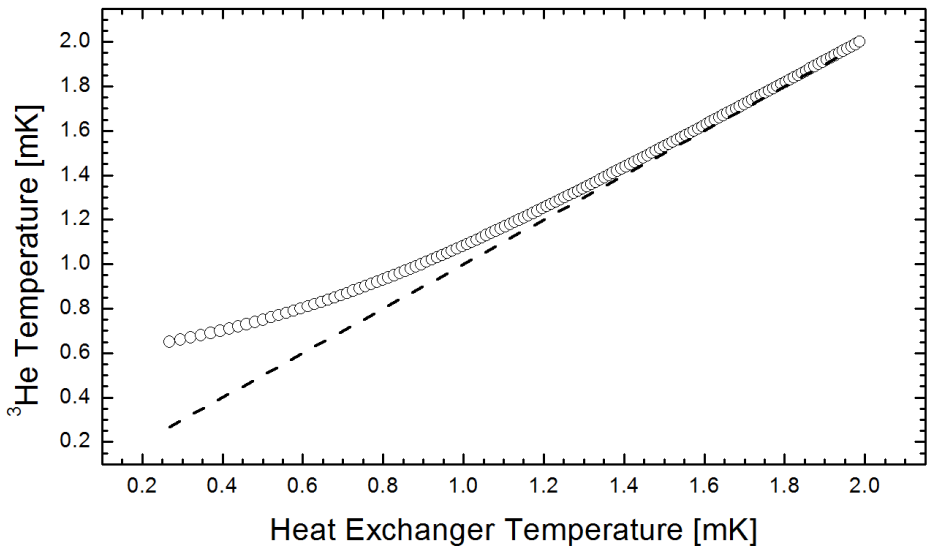

Figure 8.3: Data for the helium temperature (adjusted temperature) plotted versus the heat exchanger temperature (melting curve thermometer, unadjusted temperature) as determined for 5.6 bar, assuming T^{-3} dependence of the thermal resistance of the silver sinter heat exchanger

measured in table 8.1). The dependence of the temperature of the helium on the temperature of the heat exchanger for the pressure of 5.6 bar is shown in fig. 8.3. The lowest achievable temperature on our demagnetization stage is ~ 0.3 mK, so from fig. 8.3, we see that due to the less than optimal performance of our heat exchanger, the lowest achievable temperature for the helium in our experiment is ~ 0.6 mK.

After calibrating the quartz tuning fork for each pressure, we can use the fork as a very precise primary thermometer in our experiment which has virtually zero lag with the temperature of the fluid in the torsion head. Data from the nematically ordered aerogel experiment (chapter 7) for 0.1 and 3.6 bar is plotted in fig. 8.4a along the data for the fork in the current experiment at 0.1 bar. In the nematically ordered aerogel experiment, we did not encounter issues with high

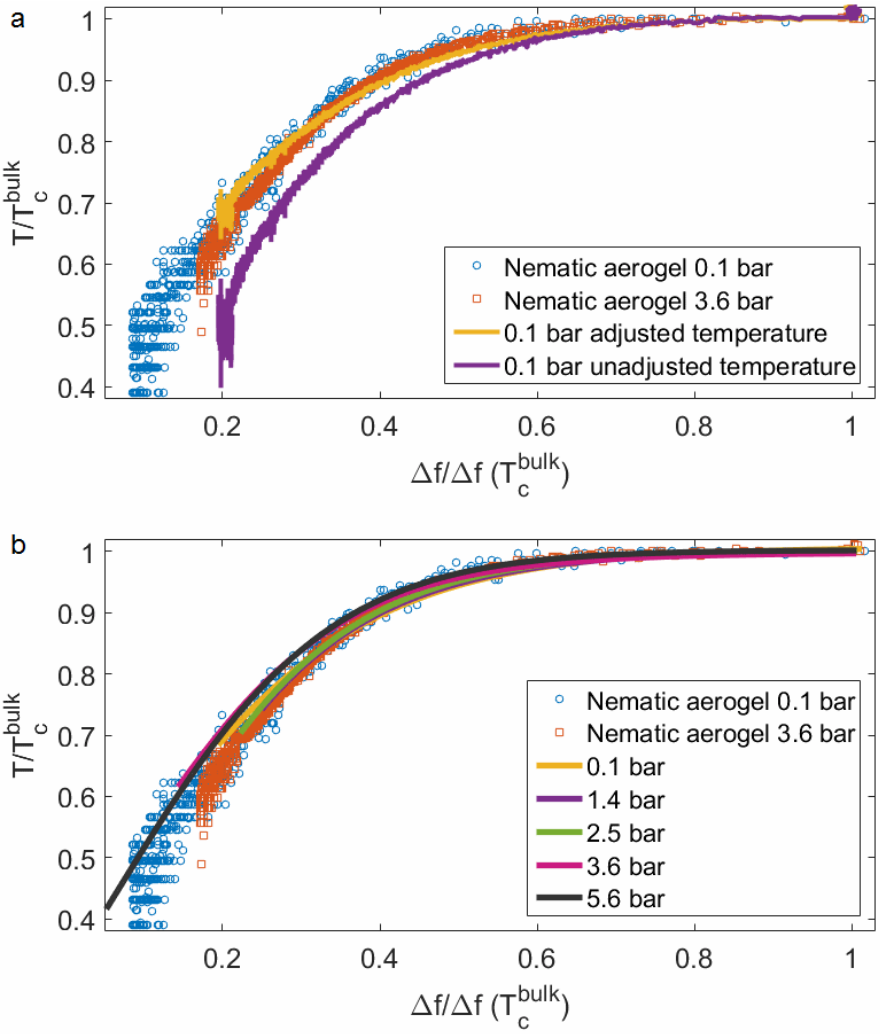

Figure 8.4: a. Data for the normalized temperature plotted versus the normalized full-width half maximum for the quartz tuning fork for the 0.1 and 3.6 bar fork data from the nematically ordered aerogel experiment. Data for 0.1 bar for the fork from the current experiment is shown using both unadjusted (melting curve thermometer) temperature and adjusted temperature (described in the text).
b. Data for the normalized temperature versus the normalized full-width half maximum for the quartz tuning fork for the 0.1 and 3.6 bar fork data from the nematically ordered aerogel experiment is plotted versus the adjusted temperature fork calibration in the current experiment..

thermal resistance of the heat exchanger.The purple trace uses the unadjusted melting curve temperature ($T_{heat\ exchanger}$) for the 1.1 μm cell data set, and clearly deviates significantly from the expected behavior. The orange trace uses the adjusted temperature T_{he} determined according to eq. 8.4, and we observe good agreement with previous experiments. Fig. 8.4b shows the calibration data for the fork at all pressures. Note that the pressure dependence is not large, and we have a good agreement with the previous experimental data, which leads credence to our calibration.

8.3 Superfluid Fraction and Dissipation Data

Figure 8.5 shows the superfluid fraction data for the five experimental pressures on cooling and warming, along with the bulk B phase superfluid fraction data at each pressure plotted versus the reduced temperature, as determined from the fork. We see that the measured superfluid fraction is very close to the bulk. This is not surprising, since Freeman showed that for ^{3}He confined within approximately 300 nm spaced Mylar sheets, the measured superfluid fraction is very close to the bulk when the surfaces were preplated with ^{4}He [83]. The fact that our experimental data shows a good agreement with the bulk is further evidence that the temperature of the helium has been estimated correctly by the method described in the previous section.

Close to Tc we observe a single, sharp resonance peak at all pressures (insets in fig. 8.5). We believe this due to a Helmholtz resonance mode crossing, most likely in the channel connecting the main cavity with the fill line. It is interesting to note that the resonance seems more pronounced on warming than on cooling.

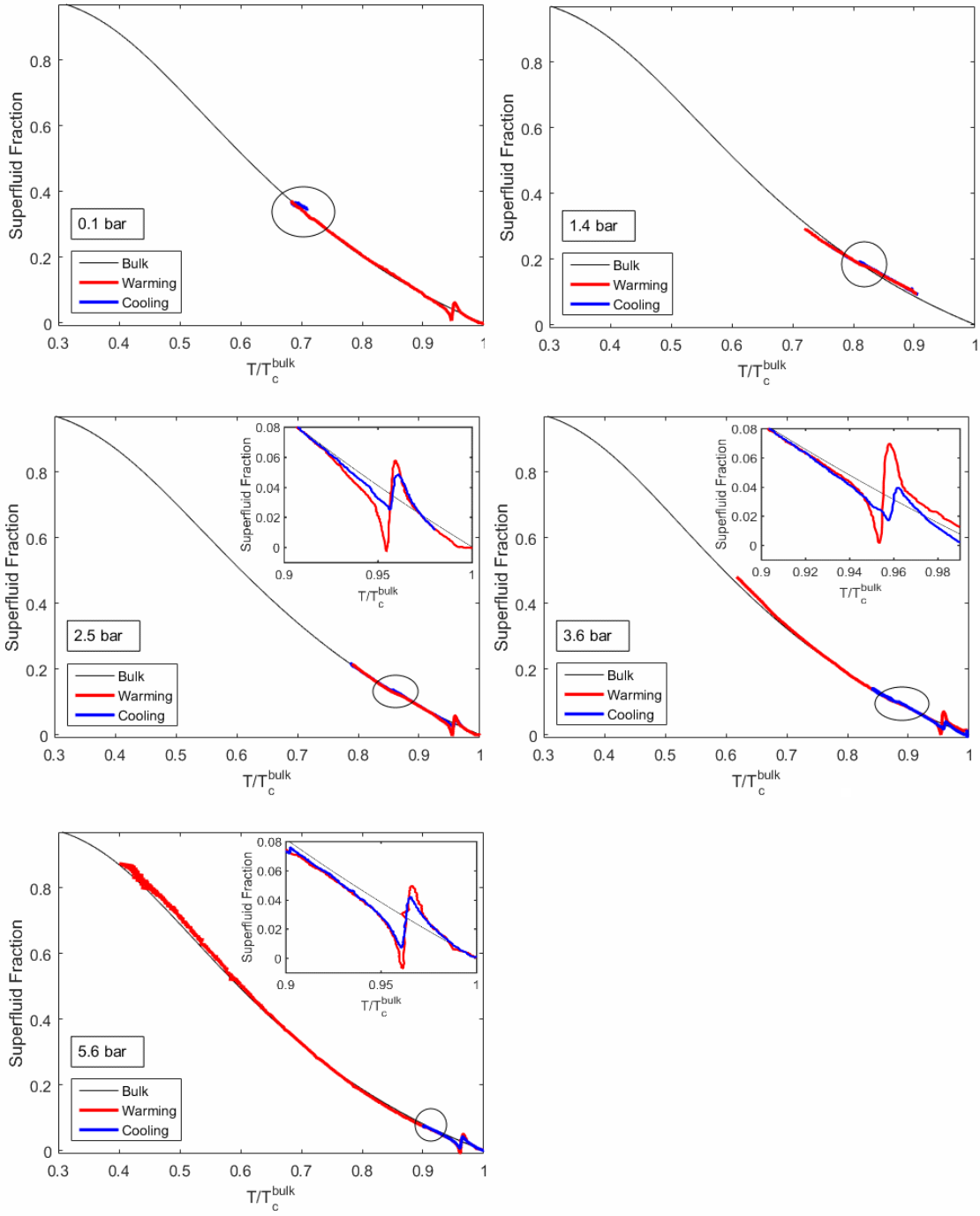

Figure 8.5: Superfluid fraction data for 0.1, 1.4, 2.5, 3.6, and 5.6 bar. Circles mark the location of the A to B and B to A transitions. See fig. 8.6

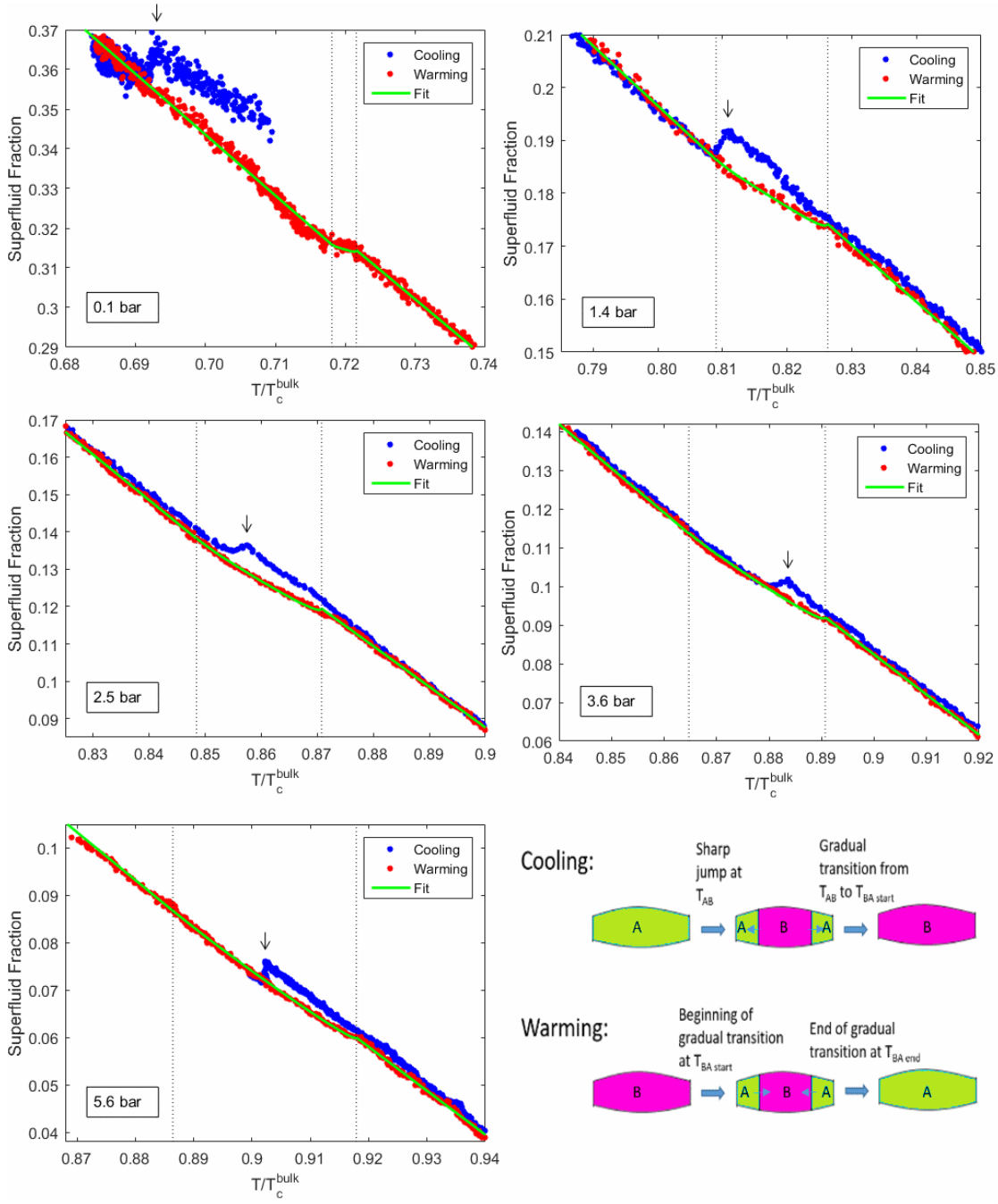

Figure 8.6: Regions of A to B transition on cooling and B to A transition on warming. Dotted lines indicate temperatures at which the B to A transition on warming starts and ends. Location of the A to B transition on cooling is indicated with an arrow at each pressure. Green line represents the B to A transition accounting for the bowing of the cell. Bottom right corner panel shows a cartoon describing the progression of the A to B transition on cooling and B to A transition on warming.

While the effect of confinement does not significantly alter the values of the superfluid fractions measured, confinement has a dramatic effect on the relative stability of the superfluid phases. We observe a high temperature superfluid phase, which we identify as the A phase at all pressures. At low temperatures, the A phase transitions to a low temperature superfluid phase, which we identify as the B phase. Unlike the NMR experiment at Royal Holloway, in which a cell with a cavity depth of 700 nm was studied, we observe an A - B transition at all pressures, down to zero bar. Figure 8.6 shows the superfluid fraction in the vicinity of A - B transition at each pressure. Figure 8.7 shows the measured torsion pendulum dissipation (Q^{-1}) over the same temperature range. A slight drift toward lower values with time for the torsion pendulum dissipation has been noted in our experiment. The drift is probably due to extremely long relaxation time of two level systems that determine the mechanical properties of the defects in the coin-silver torsion rod. For all pressures, except 5.6 bar, the cooling data was obtained first before the warming data. This is the reason why cooling data is observed to have higher overall dissipation compared to the warming data, except for 5.6 bar, at which the cooling data was obtained after the warming data, in which case it has a slightly lower dissipation.

We observe a sharp jump down in the superfluid fraction (fig. 8.6) and sharp jump up in the dissipation (fig. 8.7) as we transition from the A phase to the B phase on cooling at temperature T_{AB}. On warming, the B to A transition is seen to be gradual, starting at $T_{BA\ start}$ and ending at $T_{BA\ end}$. We can see that the A phase is associated with higher superfluid fraction and *lower* dissipation compared to the B phase. We expect that confinement orients the ℓ-vector of the A phase order parameter along the pendulum axis. Then, we would be probing along the direction of largest gap and hence expect a larger superfluid fraction

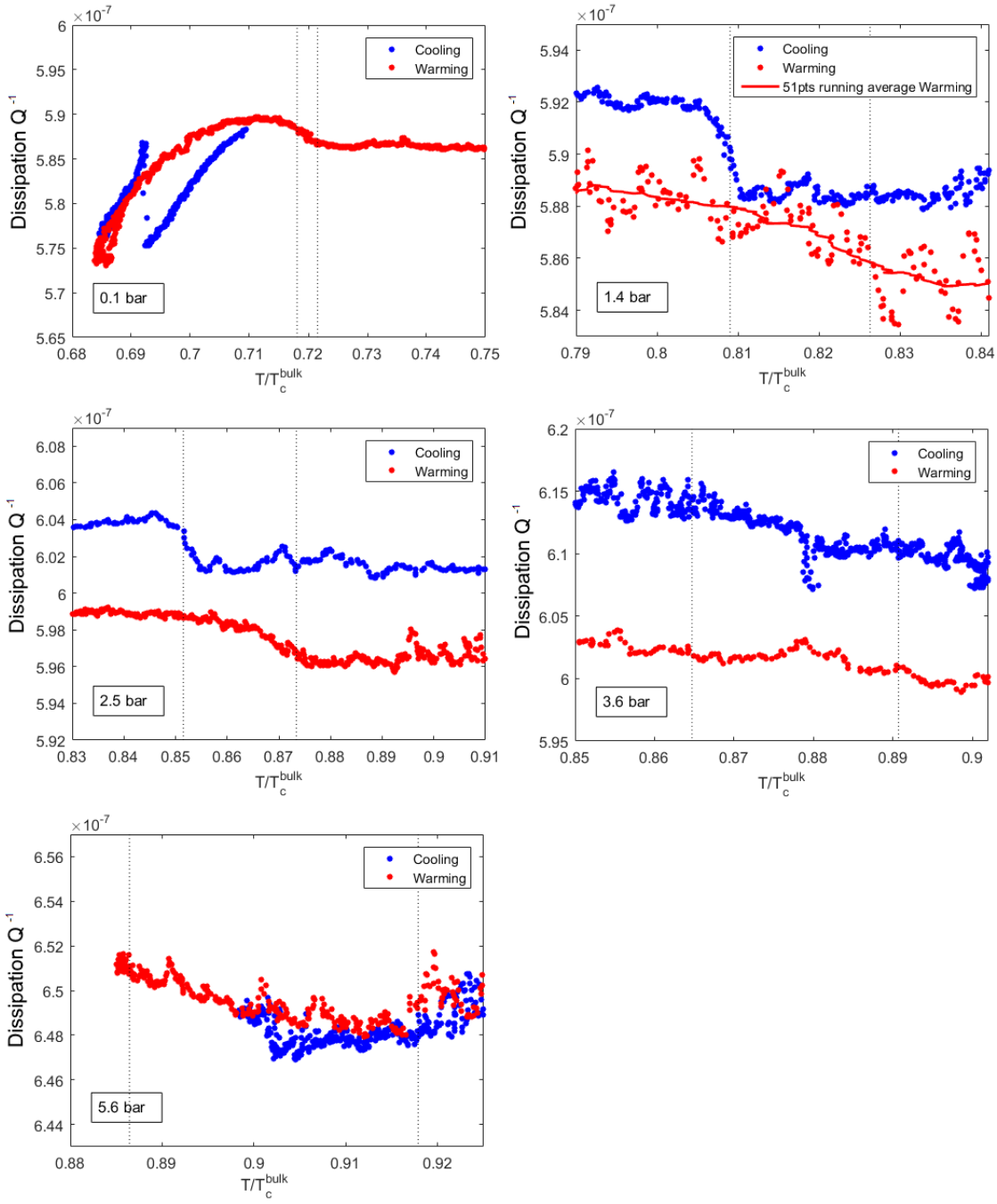

Figure 8.7: Measred dissipation $(1/Q)$ of the torsion pendulum in the region of the A-B phase boundary for the five experimental pressures. $T_{BA\ start}$ and $T_{BA\ end}$ are indicated with dotted lines.

in the A phase compared to the B phase. This is the situation we observe in our data. The ratio of the A phase superfluid fraction compared to the B phase superfluid fraction at T_{AB} is shown in table 8.2. The table also shows the values for T_{AB}, and $T_{BA\ start}$ and $T_{BA\ end}$ The A phase superfluid fraction enhancement is only slight, but agrees well with what is predicted for the bulk. Ref. [84] predicts $\rho_{sA\perp}/\rho_{sB}$ to be ~ 1.03 at 0 bar, ~ 1.09 at 10 bar, ~ 1.20 at 20 bar and ~ 1.275 at 34.36 bar.

Table 8.2: Measured ratios between superfluid fractions of A phase and B phase.

Pressure [bar]	ρ_{sA}/ρ_{sB}	T_{AB}/T_c	$T_{BA\ start}/T_c$	$T_{BA\ end}/T_c$
0.1	1.028	0.6930	0.7181	0.7216
1.4	1.037	0.8108	0.8090	0.8263
2.5	1.042	0.8574	0.8484	0.8708
3.6	1.051	0.8836	0.8647	0.8907
5.6	1.055	0.9023	0.8864	0.9179

One of the goals of this experiment was to test the prediction that the stripe phase will be formed at the onset of the A-B transition. Assuming that stripe domains are oriented perpendicular to the flow, we would expect that stripe phase will be revealed as a slight dip in the superfluid fraction measured and an increase in dissipation. We do not observe any of these tell tale signs in our data shown in fig. 8.6 and fig. 8.7.

Figure 8.8 shows the locations of T_c, T_{AB}, $T_{BA\ start}$, and $T_{BA\ end}$ on the pressure versus temperature phase diagram. Also with black solid lines are shown the predicted locations for the A to stripe, stripe to B and A to B transitions [51]. The stripe phase is predicted to be realized only at low pressures. The tempera-

ture width in T/T_c of the stripe phase region is expected to be roughly the same between 0 bar and 3 bar, and is expected to get smaller as pressure is increased further. Above a pressure of ~ 4.8 bar, no stripe phase is expected to be realized. In our experiment, we observe a larger temperature window between $T_{BA\ start}$ and $T_{BA\ end}$ as pressure is increased. If this were related to the realization of stripe phase interceding between the B to A transition, we would expect that temperature window to shrink at pressures above 5 bar. Instead, we observe that the difference between $T_{BA\ end}$ and $T_{BA\ start}$ is larger at 5.6 bar than at any of the lower pressures.

Plotting the locations of the observed phase transitions in terms of D/ξ_Δ versus pressure (fig. 8.9) can give us an insight to the source of the width observed in the B to A transition on warming (D is the depth of the cavity = 1080 nm, and ξ_Δ is the coherence length defined in eq. 2.35). If we assume that the A phase becomes the favored phase at values of D/ξ_Δ below a certain critical value, the existence of a finite width for T_{BA} can be explained through the existence of a distribution of slab thicknesses across the cell's channel. The beginning of the B to A transition is associated with transition at the part of the cell with smallest cavity depth, $D_{min} = 1080nm$ (e. g. the place where the silicon is bonded to the glass), whereas the end of the transition is associated with transition at the part of the cell with largest cavity depth D_{max} (e. g. the center of the annular cavity). Bowing of the cell due to the fluid pressure can explain the linearly increasing difference between D_{max} and D_{min} observed in fig. 8.9 as pressure is increased. At 1.4 bar and 3.6 bar, we have performed a series of measurements in which we started from the B phase and warmed partially through the B to A transition and subsequently cooled back down. For a series of turnaround points getting progressively closer to $T_{BA\ end}$, we observed a fully reversible transition. This

precludes the possibility that there is an additional first order transition (such as B to stripe or stripe to A) nested within the beginning and the end of the B to A transition. These measurements are consistent with coexistence of regions of A phase and B phase within the channel, with a phase boundary between them that is free from pinning. Once we have gone past $T_{BA\ end}$, subsequent cooling results in supercooling of T_{AB}. This is because once we have fully converted all B phase to A phase, no seeds for B phase exist, and hence A phase can get supercooled. We do not observe superheating of the B phase, because there is likely seeds of A phase present along the periphery of the cell (cell walls are not perfectly vertical).

Finite element analysis was done in COMSOL using for the cell geometry using the following values: Young's modulus for Si: 170 GPa with Poisson ratio of 0.28, and Young's modulus for glass: 73 GPa with Poisson ratio of 0.17. Note, using these parameters reproduced well the measured bowing by the Royal Holloway group on their 700 nm NMR Si-glass cell imaged at 4 K. Results for the bowing due to pressure are shown in figure 8.10. Knowing the exact profile for D across the cell, we can perform a numerical calculation for the distribution of the regions of A and B phase across the cell's channel as we go through the B to A transition. Results of this calculation as shown as solid green lines in fig. 8.6. We see very good agreement between the data and the calculation, which validates this model.

It is evident that points indicating the beginning of the B to A transition on warming (indicated in fig. 8.8 and 8.9 with orange inverted triangles) are the locations of the equilibrium transition between A phase and B phase. The A-B phase boundary is in the vicinity of the predicted A-stripe-B phase boundary by

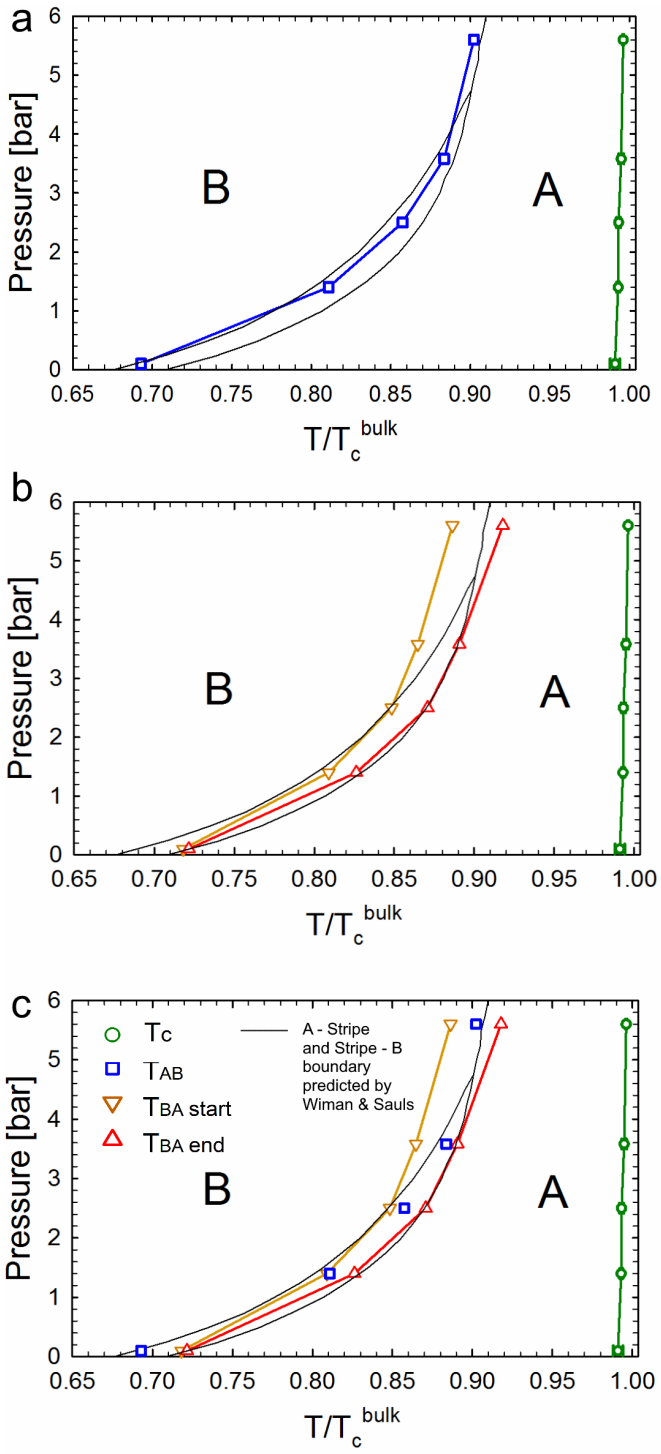

Figure 8.8: Phase diagram plotting pressure versus temperature for cooling (a), warming (b), and both cooling and warming (c).

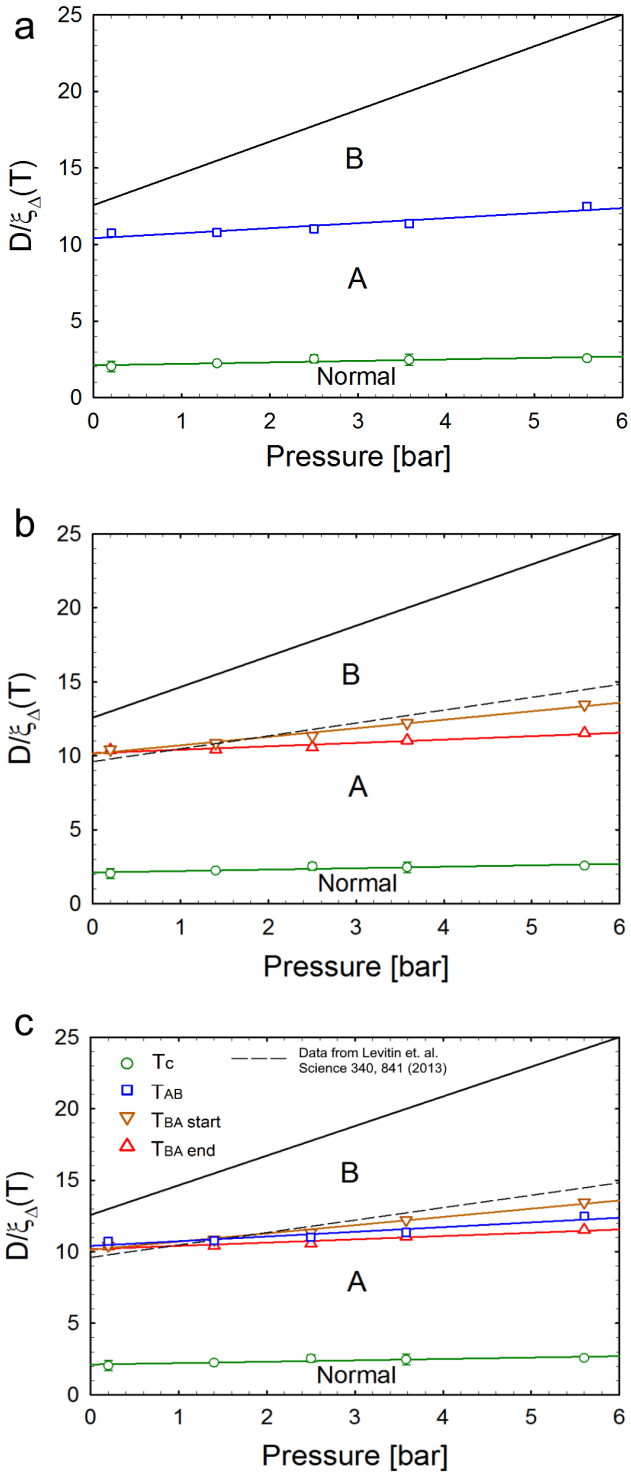

Figure 8.9: Phase diagram plotting confinement parameter $D/\xi_\Delta(T)$ versus pressure for cooling (a), warming (b), and both cooling and warming (c). Cavity depth D is not adjusted for bowing and is taken to be 1080 nm for all points.

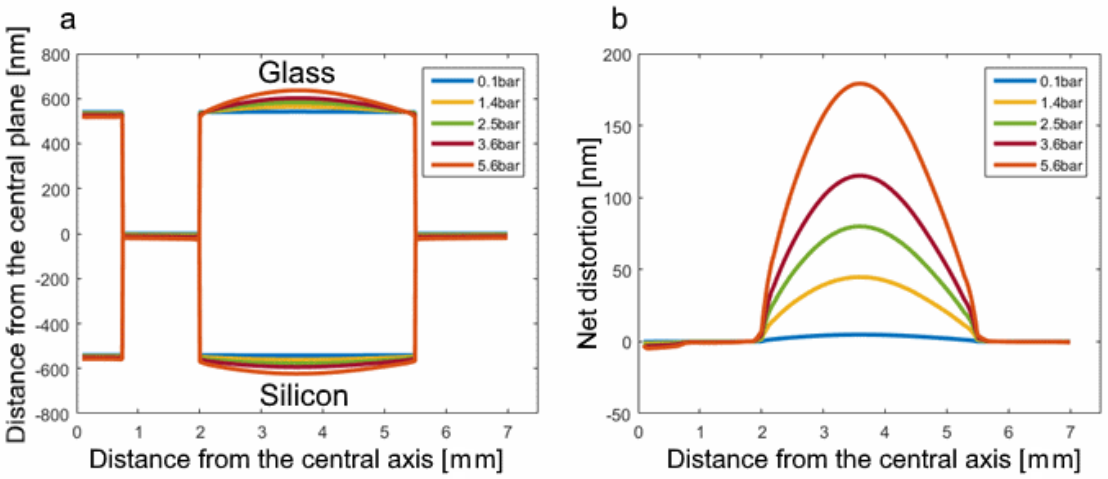

Figure 8.10: a. Cross sectional profile for the experimental cell, showing the amount of bowing for the silicon and the glass for each pressure.
b. Net distortion of the cavity.

Wiman and Sauls, but deviates from it at 3.6 and 5.6 bars. We note that there is some uncertainty in the strong coupling parameters that enter in the model of Wiman and Sauls. The experimental data for the A-B phase boundary should be able to resolve these uncertainties and help improve their model. We also compare the locations for $D/\xi_\Delta(T_{BA\ start})$ and the extrapolated values for $D/\xi_\Delta(T_{BA})$ determined by Lev Levitin's NMR measurements on a 700 nm deep cavity [18]. Our experimental data lies in the vicinity of Levitin's extrapolation, but deviates at high pressures. The data for $D/\xi_\Delta(T_{BA})$ has a linear dependence on pressure as expected, but has a somewhat smaller slope. This result indicates that there is not an universal model for the location of the A-B phase boundary in the D/ξ_Δ vs T space, but rather the location of the phase boundary also depends on the actual cavity depth D.

Finally, we want to point out that T_{AB} and T_{BA} fall exactly at the predicted locations for the A to stripe and stripe to B phase transition temperatures at

0.1 bar. This could be a coincidence or it could indicate that at 0.1 bar, unlike what we see at higher pressures, the stripe phase might be realized. Excessive bowing at higher pressures could be the reason why stripe phase is not realized at the other experimental pressures. It is worth noting that in fig. 8.6, for 0.1 bar we see a very small dip in the superfluid fraction right below the beginning of the B to A transition starting at $\sim 0.707T/T_c$ on warming. Unfortunately, we could get only to just below the A to B transition in our experiment, and we were unable to take multiple data sets at 0.1 bar to investigate further. We have made, however, an identically fabricated NMR cell with the same cavity depth. It would be worthwhile cooling that cell and investigating whether NMR can test the presence of stripe phase in that cell.

While we do not observe any "smoking gun" signs for the presence of stripes in our measurements, we cannot fully rule them out. It is possible that the pressure bowing of the cell orients the stripes into concentric circles with azimuthal symmetry. Since the flow in that case is along the stripe domain walls, their effect will be minimal in the torsion pendulum measurements. A NMR experiment done in parallel looking the same geometry is needed, as well as measurements in a cell with far less bowing need to be performed until we can rule out the presence of the stripe phase.

8.4 Conclusions

We have explored the phase diagram for superfluid ^{3}He confined within a 1080 nm deep cavity. No conclusive evidence pointing to the existence of the predicted stripe phase was observed.

8.5 Outlook and future experiments

This experiment was the first successful torsion pendulum experiment studying confined ^{3}He within a nanofabricated geometry. Building upon the success of this experiment, several more experiments are currently in preparation.

The first experiment will use the same geometry as the one described here, but will pattern the channel into a series of thin (< 10 μm) sectors etched by an additional 220 nm depth to the initial 1080 nm for a final depth of 1300 nm. The alternating sectors of 1080 nm and 1300 nm should lead to a temperature range in which A phase will be stable in the 1080 nm regions and B phase will be stable in 1300 nm regions. We would obtain either a stripe-like modulation of A-B phase regions will be stabilized or a non-equilibrium A or B phase will be realized.

In the second set of experiments, cells with cavity depths of 50, 100, 200, and 300 nm will be made. These cells will aim to revisit two old experiments [85, 86], in which a possible transition to a two-dimensional superfluid phase was thought to have been observed.

Finally, a high pressure capable cell of depth of ~ 600 nm will be made. In such a geometry, we expect to see A phase having a large region of stability at low and very high pressures. However, at intermediate pressures, the majority of the phase diagram will be occupied by the B phase with A phase confined only very near T_c.

BIBLIOGRAPHY

[1] D. D. Osheroff, R. C. Richardson, and D. M. Lee, Phys. Rev. Lett. **28**, 885 (1972).

[2] A. B. Vorontsov, and J. A. Sauls, Phys. Rev. B. **68**, 064508 (2003).

[3] A. A. Abrikosov, and I. M. Khalatnikov, Reports on Progress in Physics **22**, 329 (1959).

[4] J. Bardeen, L. N. Cooper, and J. R. Schrieffer, Phys. Rev. **108**, 1175 (1957).

[5] A. J. Leggett, Rev. Mod. Phys. **47** 331 (1975).

[6] L. D. Landau, and L. M. Lifshitz, Quantum Mechanics: Non-Relativistic Theory, Third Edition: Volume 3, Butterworth-Heinemann (1981).

[7] R. Balian, and N. R. Werthamer, Phys. Rev. **131**, 1553 (1963).

[8] D. Vollhardt, and P. Wölfle, The Superfluid Phases of Helium 3, Dover Publications Inc. (2013).

[9] J. A. Sauls, and J. W. Serene, Phys. Rev. B **24**, 183 (1981).

[10] H. Choi, J. P. Davis, J. Pollanen, T. M. Haard, W. P. Halperin, Phys. Rev. B. **75**, 174503 (2007).

[11] P. W. Anderson, and P. Morel, Phys. Rev. **123**, 1911 (1961).

[12] P. W. Anderson, and W. F. Brinkman, Phys. Rev. Lett. **30**, 1108 (1973).

[13] D. S. Greywall, Phys. Rev. B **33**, 7520 (1986).

[14] W. P. Halperin, R. A. Buhrman, D. M. Lee, and R. C. Richardson, Physics Letters A **45**, 233 (1973).

[15] D. N. Paulson, H. Kojima, and J. C. Wheatley, Phys. Rev. Lett. **32**, 1098 (1974).

[16] V. Ambegaokar, P. G. deGennes, and D. Rainer, Phys. Rev. A **9**, 2676 (1974).

[17] J. Hara, and K. Nagai, J. Low Temp. Phys. **72**, 407 (1988).

[18] L. V. Levitin, R. G. Bennett, A. Casey, B. Cowan, J. Saunders, D. Drung, Th. Schurig, and J. M. Parpia, Science **340**, 841 (2013).

[19] A. P. Mackenzie, Y. Maeno, Rev. Mod. Phys. **75**, 657 (2003).

[20] Y. Dalichaouch, M. C. de Andrade, D. A. Gajewski, R. Chau, P. Visani, and M. B. Maple, Phys. Rev. Lett. **75**, 3938 (1995).

[21] P. W. Anderson, Journal of Physics and Chemistry of Solids **11**, 26 (1959).

[22] J. V. Porto, J. M. Parpia, Phys. Rev. Lett. **74**, 4667 (1955).

[23] D. T. Sprague, et. al., Phys. Rev. Lett. **75**, 661 (1995).

[24] Y. Lee, and R. P. Haley, Novel Superfluids: Volume 1, chapter5: Superfluid helium three in aerogel: experiment, Oxford Science Publications (2013).

[25] J. Fricke, Scientific American **258**, 92 (1988).

[26] J. V. Porto, and J. M. Parpia, Phys. Rev. B **59**, 14583 (1999).

[27] J. Kim, et. al., Small **7**, 2542 (2011).

[28] J. A. Sauls, Yu. M. Bunkov, E. Collin, H. Godfrin, and P. Sharma, Phys. Rev. B **72**, 024507 (2005).

[29] H. Götz, and G. Eska, Physica B: Condensed Matter **329-333**, 307 (2003).

[30] P.A. Reeves, G. Tvalashvili, S.N. Fisher, A.M. Guénault and G.R. Pickett, J. Low Temp. Phys., **129** 185 (2002).

[31] P. Venkataramani and J.A. Sauls, Physica B **284**, 297 (2000).

[32] H. Takeuchi, et. al., Phys. Rev. Lett., **108**, 225307 (2012).

[33] P. Sharma and J.A. Sauls Physica B **329** 313 (2003).

[34] S.N. Fisher, A.M. Guénault, A.J. Hale, and G.R. Pickett, Phys. Rev. Lett. **91** 105303 (2003).

[35] H. Choi, K. Yawata, T.M. Haard, J.P. Davis, G. Gervais, N. Mulders, P. Sharma, J.A. Sauls, and W.P. Halperin, Phys. Rev. Lett. **93** 145302 (2004).

[36] E.V. Thuneberg, S.K. Yip, M. Fogelström, and J.A. Sauls, Phys. Rev. Lett. **80** 2861 (1998).

[37] K. Matsumoto, J. V. Porto, L. Pollack, E. N. Smith, T. L. Ho, and J.M. Parpia, Phys. Rev. Lett. **79** 253 (1997).

[38] J. Pollanen, J. I. A. Li, C. A. Collett, W. J. Gannon, W. P. Halperin, Phys. Rev. Lett. **107**, 195301 (2011).

[39] E. Nazaretski, N. Mulders, and J.M. Parpia, JETP Lett. **79** 383 (2004).

[40] K. Aoyama and R. Ikeda, Phys. Rev. B **73** 060504(R) (2006).

[41] J. Pollanen, et. al., Journal of Non-Crystalline Solids **354**, 4668 (2008).

[42] G. E. Volovik, Journal of Low Temperature Physics **150**, 453 (2008).

[43] J. Pollanen, J. I. A. Li, C. A. Collett, W. J. Gannon, W. P. Halperin, and J. A. Sauls, Nature Physics **9**, 775 (2013).

[44] J. A. Sauls, Phys. Rev. B **88**, 214503 (2013).

[45] V. E. Asadchikov, et. al., JETP Lett. **101**, 556 (2015).

[46] Y. Nagato, M. Yamamoto, and K. Nagai, Journal of Low Temperature Physics **110**, 1135 (1998).

[47] L.H. Kjäldman, J. Kurkijärvi, and D. Rainer, Journal of Low Temperature Physics **33**, 577 (1978).

[48] A. B. Vorontsov and J. A. Sauls, Phys. Rev. Lett. **98**, 045301 (2007).

[49] H. Mayaffre, S. Krämer, M. Horvatić, C. Berthier, K. Miyagawa, K. Kanoda, and V. F. Mitrović, Nature Physics **10**, 928 (2014).

[50] J. Wiman, and J. A. Sauls, Poster presentation at he international symposium on quantum fluids and solids QFS2015, Niagara Falls, NY. (2015).

[51] J. Wiman, and J. A. Sauls, private communication.

[52] S. M. Tholen, and J. M. Parpia, Phys. Rev. B **47**, 319 (1993).

[53] Suk Bum Chung, and Shou-Cheng Zhang, Phys. Rev. Lett. **103**, 235301 (2009).

[54] G. E. Volovik, JETP Letters **90**, 398 (2009).

[55] M. M. Salomaa, and G. E. Volovik, Phys. Rev. B **37**, 9298 (1988).

[56] X.-L. Qi, S.-C. Zhang, Rev. Mod. Phys. **83**, 1057 (2011).

[57] H. Wu, and J. A. Sauls, Phys. Rev. B **88**, 184506 (2013).

[58] B. E. Deal, and A. S. Grove, J. Appl. Phys. **36**, 3770 (1965).

[59] S. G. Dimov, PhD thesis, Cornell University (2009).

[60] C. N, Archie, T. A. Alvesalo, J. D. Reppy, and R. C. Richardson, Journal of Low Temperature Physics, **42**, 295 (1981).

[61] J. M. Parpia, D. J. Sandiford, J. E. Berthold, and J. D. Reppy, Phys. Rev. Lett. **40**, 565 (1978).

[62] D. S. Greywall, Phys. Rev. B **29**, 4933 (1984).

[63] J. M. Parpia, D. G. Wildes, J. Saunders, E. K. Zeise, J. D. Reppy and R. C. Richardson, J. Low Temp. Phys. **61** 337, (1985).

[64] D. Einzel, and J. M. Parpia, Phys. Rev. Lett. **58**, 1937 (1987).

[65] A. Golov, D.A. Geller, N. Mulders, and J.M. Parpia, Phys. Rev. Lett. **82**, 3492 (1999).

[66] W. P Halperin, H. Choi, J. P. Davis, and J. Pollanen, J. Phys. Soc. Jap. **77** 111002 (2008).

[67] N. Zhelev, R. G. Bennett, E. N. Smith, J. Pollanen, W. P. Halperin, and J. M. Parpia, Phys. Rev. B **89**, 094513 (2014).

[68] M. C. Cross and P.W. Anderson, in Proceedings of the 14th International Conference on Low Temperature Physics, Ontaniemi, Finland, North-Holland, Amsterdam, Oxford, Vol. 1, p. 29. (1975).

[69] M. C. Cross, AIP Conf. Proc. **103**, 325 (1983).

[70] D. I. Bradley, S. N. Fisher, A. M. Guénault, R. P. Haley, N. Mulders, S. O'Sullivan, G. R. Pickett, J. Roberts, and V. Tsepelin, Phys. Rev. Lett. **98** 075302 (2007).

[71] D. I. Bradley, S. N. Fisher, A. M. Guénault, R. P. Haley, G. R. Pickett, J. E. Roberts, S. O'Sullivan, and V. Tsepelin, Journal of Low Temperature Physics **150**, 445 (2008).

[72] R. G. Bennett, N. Zhelev, E. N. Smith, J. Pollanen, W. P. Halperin, J. M. Parpia, Phys. Rev. Lett. **107**, 235504 (2011).

[73] R. Sh. Askhadullin, et. al., JETP Letters **95**, 326 (2012).

[74] V. V. Dimitriev, et. al., JETP **119**, 1088 (2014).

[75] R. Sh. Askhadullin, et. al., JETP Letters **100**, 662 (2015).

[76] I. A. Fomin, JETP **118**, 765 (2014).

[77] R. Sh. Askhadullin, et. al., Journal of Physics: Conf. Series **400**, 012002 (2012).

[78] R. Ikeda, Phys. Rev. B **91**, 174515 (2015).

[79] G. Lawes, and J. M. Parpia, Phys. Rev. B **65**, 092511 (2002).

[80] S. G. Dimov, R. G. Bennett, B. Ilic, S. S. Verbridge, L. V. Levitin, A. D. Fefferman, A. Casey, J. Saunders, and J. M. Parpia, Journal of Low Temperaure Physics **158** 155 (2010).

[81] P. Sharma, A. Crcoles, R. G. Bennett, J. M. Parpia, B. Cowan, A. Casey, and J. Saunders, Phys. Rev. Lett. **107**, 196805 (2011).

[82] D. J. Cousins, S. N. Fisher, A. M. Gunault, G. R. Pickett, E. N. Smith, and R. P. Turner, Phys. Rev. Lett. **73**, 2583 (1994).

[83] M. R. Freeman, PhD thesis, Cornell University (1988).

[84] Y. Kuroda, and A. D. S. Nagi, J. of Low Temp. Phys. **25**, 569 (1976).

[85] J. Xu and B. C. Crooker, Phys. Rev. Lett. **65**, 3005 (1990).

[86] A. M. R. Schechter, R. W. Simmonds, R. E. Packard, and J. C. Davis, Nature **396**, 554 (1998).